THE UNIVERSITY OF READING

Department of Meteorology

The energy balance of urban areas

Ian Nicholas Harman

A thesis submitted for the degree of Doctor of Philosophy

October 2003

Declaration

I confirm that this is my own work and the use of all material from other sources has been properly and fully acknowledged.

Ian Nicholas Harman

ABSTRACT

Urban areas have different climatologies to their rural surroundings. The physical mechanisms responsible for these differences are not accurately known. This work contributes to the better understanding of the physical processes acting in urban areas.

The role of surface morphology in determining the surface energy balance of an urban area and the subsequent impacts on the planetary boundary layer are investigated. The urban street canyon is used as the generic unit of the urban surface in a range of analytic, experimental and numerical investigations.

The first part of this work considers the role of surface morphology on the individual terms of the surface energy balance. An analytical approach was used to investigate the exchange of diffuse radiation in a street canyon. Multiple reflections of radiation were found to play an important role. An experimental approach and process based modelling were used to analyse the turbulent flux of a scalar from a street canyon. The variation of the flow and turbulence with surface morphology both above and within the street canyon was found to determine the surface flux densities. The competing effects of surface geometry, which decreases the flux densities, and the increased surface area, which increases the total fluxes, determines the net effect of surface morphology on the energy balance.

The second part of the work considers the interaction between the surface energy balance and the boundary layer. A coupled model of the surface energy balance and boundary layer was used to investigate the impact of surface morphology on the boundary layer. The impacts of surface morphology, on their own, result in realistic surface, canopy and boundary layer urban heat islands. An investigation into simplifying the urban street canyon energy balance shows that two surfaces, a roof surface and a canyon surface, are needed to represent the surface energy balance of urban areas. The adjustment of the boundary layer under advection from a rural to an urban area is suggested to be a key process even at low wind speeds.

Acknowledgements

I express my thanks to my supervisors, Dr. S. E. Belcher and M. J. Best, for their invaluable support, assistance and guidance throughout this project. I am grateful for the support and guidance given by Prof. K. Browning and Prof. P. Valdes in their direction of this work.

Thanks also go to Dr. J. F. Barlow in formulating and building the experiments and for valuable discussions in interpreting the results. I acknowledge the technical support of the experiments by S. Gill and A. Lomas. I thank P. Clark for graciously stepping in to support the project when unforeseen circumstances occured in the later stages. Thanks must also go the Boundary-Layer group and my fellow PhD students for the support and guidance in the presentation of this work and the wider support given. Thanks go to J. Finnigan and to Prof. K. Shine for their input concerning the work in Chapter 2.

I am immensely grateful to my family for their unwaivering support and encouragement over the years. I am also grateful to all my friends, especially Chloe, James and Sheula, Baz, Litka and Ulash, within and outside the department for being there and helping me to keep perspective. Many thanks to all at the Department of Meteorology for making the department such a friendly place where it is a pleasure to work. Finally, thanks to the members of the University of Reading Mixed Hockey Club and my fellow squash players in helping me forget things when I needed to.

This research was funded by the Natural Environment Research Council and the Met Office through a CASE award.

Contents

Glossary of terms

The individual terms are introduced in detail within the main text.

Standard terms

t	time (s)
(x, y, z)	standard orthogonal co-ordinate system either aligned east-west, north-south or x aligned with the mean wind.
ρ	density of air (1.2 kg m^{-3})
g	acceleration due to gravity (9.8 m s^{-2})
c_p	specific heat capacity of air at constant pressure (1004 J kg^{-1}K^{-1})
$\theta_s(T_i)$	surface temperature (of surface i) (K)
δ_{ij}	Kronecker-delta operator.

Averaging operators

$\bar{x}$	time-average of property x
$\langle x \rangle$	spatial-average of property x
x'	instantaneous deviation of x from its time- and spatial- average
x_*	scaling value for x'

Surface dimensions

h_e	height of the buildings (m)
w_e	width of the street (m)
r_e	width of the generic surface unit (m)
λ_p	planar area index
λ_f	frontal area index
z_2	reference height in the inertial sub-layer (m)
z_i	height of the boundary layer (m)

Subscripts

i, j, k	general subscripts
rf	roof
s	surface
st	street
us (ds)	upstream (downstream) section of the street (Chapter 3)
wl $(w1, w2)$	wall
uw (dw)	upstream (downstream) wall (Chapter 3)
c	canyon
sk	sky

Boundary layer variables

$\overline{\mathbf{v}}(z)$	vertical profile of the horizontal wind vector aligned in the $x-y$ directions (m s^{-1}) $\big(= (\overline{u}(z), \overline{v}(z))\big)$
$U(z)$	vertical profile of the wind speed (m s^{-1})
U_δ	wind speed at the top of the inertial sub-layer (m s^{-1})
(u_g, v_g)	geostrophic wind vector (m s^{-1})
(u_F, v_F)	mean wind for the upstream profile (Chapter 6) (m s^{-1})
τ	turbulent stress (kg m^{-1}s^{-2})
u_*	surface friction velocity (m s^{-1})
λ (λ_e)	(equilibrium) mixing length (m)
$\theta(z)$	vertical profile of potential temperature (K)
L	Monin-Obukhov length (m)
R_i	Richardson number
Ψ_m, Ψ_h	integrated stability functions for momentum and heat respectively
$\overline{\theta}_F$	mean potential temperature for the upstream profile (K)
L_F	distance from the change in surface type (fetch) (Chapter 6) (m)
K_m, K_h	turbulent diffusivities for momentum and heat respectively (m^{2}s^{-1})
H	surface sensible heat flux (W m^{-2})
w_*	scaling for the vertical velocity (m s^{-1})

Energy balance variables

$K^{\downarrow}$	total downwelling wavelength-integrated solar radiative flux density (W m^{-2})
$K^{\uparrow}$	total upwelling wavelength-integrated solar radiative flux density (W m^{-2})
$L^{\downarrow}$	downwelling wavelength-integrated longwave radiative flux density (W m^{-2})
$L^{\uparrow}$	upwelling wavelength-integrated longwave radiative flux density (W m^{-2})
Q^{*}	net radiative flux density (W m^{-2})
K_{sf} (K_{df})	direct (diffuse) component of the solar radiative flux density (W m^{-2})
H	sensible heat flux density (W m^{-2})
LE	latent heat flux density (W m^{-2})
G	ground heat flux density (W m^{-2})
k	thermal conductivity of the substrate (W k^{-1}m^{-1})
c_s	volumetric heat capacity of the substrate (J K^{-1}m^{-3})
α_i	wavelength-integrated albedo for the material of surface i
ε_i	wavelength-integrated emissivity for the material of surface i
T_L	linearising temperature (273 K)
T_{in}	substrate interior temperature (K)
G_{in}	interior ground heat flux (W m^{-2})
w_T	transport velocity for the turbulent fluxes (m s^{-1})
$\mathcal{F}_1, \mathcal{F}_2, \mathcal{F}_4$	approximations to the full canyon energy balance (Chapter 5)

Radiation variables (Chapter 2)

$\Lambda_{i(j)}$	flux density of incoming diffuse radiation onto surface i which has originated directly from surface j (W m^{-2})
Λ_i	total flux density of incoming diffuse radiation onto surface i (W m^{-2})
Ω_i	flux density of emitted diffuse radiation from surface i (W m^{-2})
B_i	total flux density of diffuse radiation away from surface i (W m^{-2})
Q_i	net radiative flux density for surface i (W m^{-2})
F_{ij}	matrix of shape factors
Γ_{ij}	matrix for radiative interaction
ψ_{ij}	inverse of Γ_{ij}
$\mathcal{R}_0, \mathcal{R}_1$	approximation methods to full solution for radiative exchange

Turbulent transport variables (Chapter 3)

X	generic scalar
z_{0m}, z_{0X}	roughness lengths for momentum and X, respectively, pertaining to the surface material (m)
z_{0T}, z_{XT}	roughness lengths for momentum and X, respectively, pertaining to the entire canyon unit (m)
d_T	displacement height pertaining to the entire canyon unit (m)
r_X	resistance to the turbulent transport of scalar X (s m^{-1}) - often relates to the transport across an internal boundary layer
$r_{\Delta X}$	resistance to the turbulent transport of scalar X across a free shear layer (s m^{-1})
w_X	turbulent transport velocity for the flux density of scalar X (m s^{-1})
w_i	turbulent transport velocity for the flux density from surface i (m s^{-1})
w_c	turbulent transport velocity for the flux density out of the canyon cavity (m s^{-1})
w_t	turbulent transport velocity for the total flux density from the (canyon) surface into the boundary layer (m s^{-1})
w_{0t}	turbulent transport velocity for the flux density from a flat surface of equivalent surface material (m s^{-1})
L_r	maximum length of the recirculation zone (m)
L_{se}	length of the sloping edge of the recirculation zone (m)
u_i	wind speed representative of the turbulent transport from surface i (m s^{-1})
u_{ct}	wind speed representative of turbulent transport at canyon top (m s^{-1})
δ_i	depth of the internal boundary layer formed along surface i (m)
α_1, α_2	coefficients for the deceleration of the flow in the canyon cavity.
c_D	turbulent drag coefficient (kg m^{-3})
C_D	turbulent drag coefficient based on the wind speed at building height (kg m^{-3})

CHAPTER ONE

Introduction

The lowest layers of the atmosphere are known as the *planetary boundary layer* or simply the *boundary layer*. Stull (1988) defines the boundary layer as "that part of the atmosphere that is directly influenced by the presence of the Earth's surface, and responds to surface forcings with a time scale of about an hour or less." Boundary layer meteorology, the study of this layer of the atmosphere, is characterised by the study of the turbulent nature of the boundary layer.

The airflow and thermal structure of the boundary layer is determined by the Earth's surface. In particular, the *surface energy balance*, the partitioning of energy at the surface into different forms, and the drag exerted by the surface determine the surface temperature and the vertical profiles of wind and temperature in the boundary layer. Urban areas alter the material and aerodynamic character of the surface, greatly affecting the surface energy balance as well as the dynamic and thermodynamic nature of the boundary layer. These modifications to the local climate are the core topics of *urban meteorology* and *urban climatology*.

Urban modifications to the local climate are manifested in a variety of forms. Urban areas are generally warmer, less windy and drier in a relative sense than their rural surroundings (e.g. Oke, 1987). However, the role of the rural surroundings in determining these modifications cannot be understated (Arnfield, 2003). The most prominent feature of the local climate of urban areas is the well known *urban heat island*. This is a transient feature of urban areas, usually nocturnal, where the urban surface and near-surface air temperatures are warmer than their rural surroundings. Oke (1982) presents a number of physically based explanations for the urban heat island. The precise causality is different for each urban area with the reduction in moisture availability, changes in the surface material properties and reduced longwave radiative cooling through radiative trapping considered to be the dominant processes (Oke, 1987; Oke *et al.*, 1991; Arnfield, 2003).

Investigation of the thermal and dynamic properties of urban areas is important in a range of applications. Heat stress resulting from the urban heat island can be a major concern for public health (e.g. Dabbert *et al.*, 2000). Similarly the dispersion characteristics of pollutants, known to depend on the location of the source (Oke, 1987) and synoptic conditions (Ketzel *et al.*, 2002), have important impacts on public health. More recently attention has focussed on the dispersal of hazardous chemical or biological releases within urban areas. Architects and building engineers require detailed knowledge of the airflow in urban areas to determine the structural strength and energy requirements of new buildings. Finally, the increasing resolution of numerical weather prediction models makes the practical forecasting of the weather within urban areas a real possibility. Such work will also allow the assessment of whether urban areas impact significantly upon mesoscale weather systems as has been speculated (e.g. Bornstein and Thompson, 1981; Bornstein and Lin, 2000; Rozoff and Adegoke, 2003). Accurate, but simple, methods to incorporate the range of dynamic and thermodynamic influences on the boundary layer across the full range of urban types and synoptic conditions are therefore required.

A range of methods have been used to investigate the urban boundary layer and urban energy balance. These include wind and water tunnel simulations (e.g. Barlow and Belcher, 2002; Lu *et al.*, 1997a,b), numerical simulations (e.g. Hunter *et al.*, 1992; Johnson and Hunter, 1995; Baik and Kim, 1999; Liu and Barth, 2002), field experiments (e.g. Cleugh and Oke, 1986; Grimmond, 1992) and high resolution remote sensing (e.g. Lee, 1993).

This study focusses on one aspect of urban areas, namely the surface morphology, and how it controls urban meteorology. Changes in the surface morphology are possibly the one property common to all urban areas. It is therefore important to consider fully the impact of surface morphology on all parts of the surface energy balance and boundary layer. The remainder of this introductory chapter presents a brief overview of the energy balance and boundary layer of urban areas concentrating on the current understanding, the fundamental paradigms, concepts and assumptions used throughout the thesis, as well as perceived gaps in knowledge. The specific aims of this work are then introduced together with a more detailed outline of the thesis. Detailed motivation for each of the sections of work are included at the beginning of those sections.

1.1 Scale and the urban surface

The complex morphology of an urban area results in a range of effects in the boundary layer and energy balance. The urban surface is notably highly non-homogeneous varying on a range of spatial scales. Fundamental to understanding the physical mechanisms responsible for the urban modifications to the local climate is the spatial scale upon which the physical processes act. Figure 1.1 relates several topics within urban climatology to the typical spatial scales on which they are considered (e.g. Britter and Hanna, 2003). Of course, physical processes acting on one spatial scale can be influenced by others acting on a different spatial scale. For example the detailed transport processes at the street scale determine the boundary conditions for the boundary layer which in turn impacts larger scale processes. Similarly, the synoptic and regional scale forcing can influence all of the smaller scales. A key aspect of urban meteorology concerns the description and classification of the surface on the relevant spatial scale.

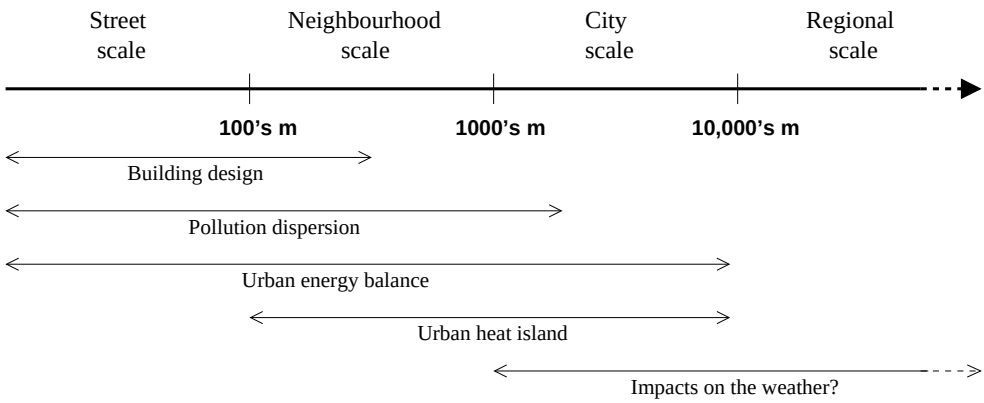

Figure 1.1: Schematic relating topics within urban climatology and their spatial scales.

Buildings impose two properties of the urban surface. Firstly, the total surface area is increased from that of a planar surface. Secondly, the surface is deformed to accommodate the increase in surface area. The term *surface geometry* is used in this thesis specifically to denote the deformation of the surface, i.e. the dimensions and separation of the buildings. The term *surface morphology* is used to denote the combined effects of increasing the surface area and the deformation of the surface.

The full detail of the urban surface is only needed, and indeed only practical, for highly specific studies, for instance into the dispersion of pollutants from a specific source within a building array. More common is a requirement to classify the average effects of the urban surface on the appropriate spatial scale. The simplest general method to classify the surface morphological

characteristics requires three parameters, namely the building height h_e, the planar area index λ_p and the frontal area index λ_f (e.g. Grimmond and Oke, 1999a) averaged over the scale of interest. The planar area index is the ratio of the land surface occupied by the footprints of the buildings to the total land surface area. The frontal surface area index is the ratio of the surface area exposed to the mean wind to the total land surface area. Thus λ_f depends on the direction of the mean wind. These three morphological parameters are illustrated in Figure 1.2 for an array of uniform buildings. Depending on the case considered, additional information may be required such as the asymmetry in building size (Bottema, 1996) or the vegetated fraction of the land surface (O'Rourke and Terjung, 1981).

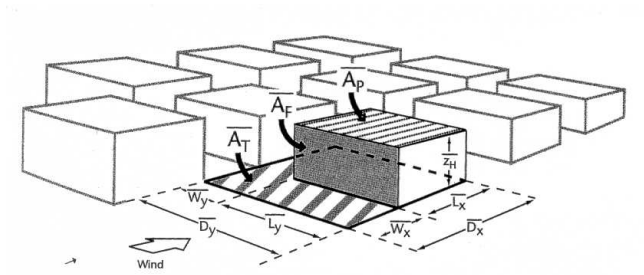

Figure 1.2: Schematic of the morphometric ratios for an array of three dimensional uniform buildings. The non-dimensional ratios are defined as: $\overline{\lambda_p} = \overline{A_P}/\overline{A_T} = \overline{L_x L_y}/\overline{D_x D_y}$, $\overline{\lambda_f} = \overline{A_F}/\overline{A_T} = \overline{z_H L_y}/\overline{D_x D_y}$ (after Grimmond and Oke, 1999a).

Even within this framework the range of surface morphologies possible is too large to investigate realistically. Both observational and modelling studies have therefore attempted to base their studies on generic units of the urban surface. There is then an implicit assumption that the behaviour of the atmosphere over, and energy balance of, these generic units mimics those of real-life urban areas of a similar morphological nature. Such generic units include the urban street canyon (e.g. Nunez and Oke, 1977) and arrays of cubes (e.g. Aida, 1982). The difference between the real urban areas and these generic units should always be remembered when comparing observations and model results or infering results from modelling studies.

This work considers the *urban street canyon* to be the generic unit of the urban surface. This is the simplest unit of an urban area which allows the surface morphology to be varied. The urban street canyon consists of two parallel, uniform in height, uniform in size buildings with flat roofs. This generic unit of an urban area and the nomenclature used is shown in Figure 1.3*. For this generic unit (under flow normal to the canyon axis) $\lambda_f = h_e/r_e$ and $\lambda_p = 1 - w_e/r_e$.

*An unfortunate clash of notation exists between the urban climatology community and the wider surface exchange/boundary layer communities. This thesis uses the boundary layer community notation where possible.

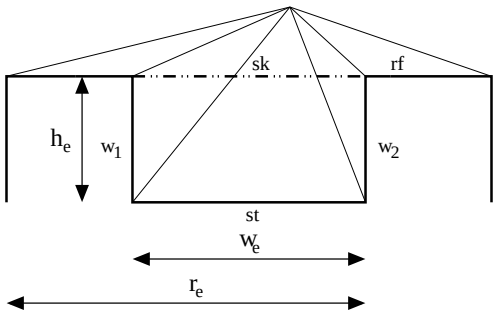

Figure 1.3: Perspective schematic of an urban street canyon together with the characteristic dimensions and nomenclature used. Note the four facets of the urban street canyon, the street (st), the two walls (w1 and w2), and the roof (rf), together with a transparent surface at canyon top (sk) (see Chapter 4).

1.2 The urban boundary layer

The boundary layer over an urban area is of particular interest as it is in this layer of the atmosphere that the majority of routine observations in urban areas are taken. It is therefore important to know what these observations represent. As air flows from one surface to another an *internal boundary layer* forms. The internal boundary layer is influenced by, but not fully adjusted to, the new surface and deepens with fetch. The internal boundary layer formed over urban areas is the *urban boundary layer*. The urban boundary layer is however a collection of successive internal boundary layers rather than one internal boundary layer due to the continual changing of building formations and densities across the urban area.

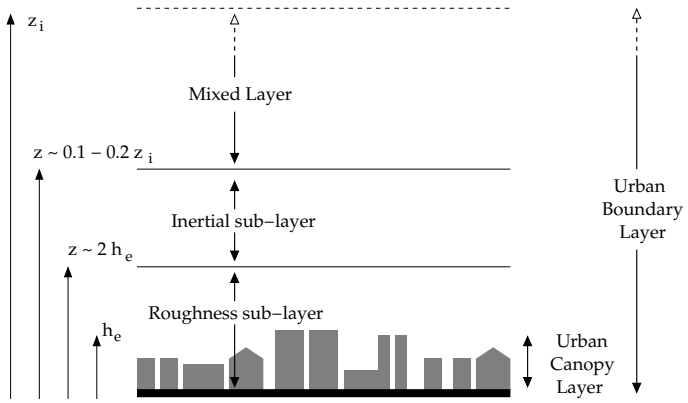

Figure 1.4: Schematic of the boundary layer over an urban surface with typical depths for the sub-layers (e.g. Roth, 2000). z_i is the depth of the planetary boundary layer over an urban area.

The boundary layer is traditionally partitioned into a number of sub-layers dependent on the characteristics of the mean and turbulent parts of the flow (e.g. Garratt, 1992). Over an urban

area this traditional partitioning is modified to account for the large impacts of urban areas on the boundary layer (Oke, 1987). This partitioning into four sub-layers is shown in Figure 1.4. The four layers (from the top down) are:

- The *mixed layer*: The flow and potential temperature are rapidly mixed resulting in horizontally homogeneous, vertically uniform profiles. By night this sub-layer may be further partitioned into a residual of the previous day's mixed layer overlying a surface inversion layer which has been cooled from below. The mixed layer may also be capped by an inversion layer at the top of the boundary layer. Little is known about any differences between urban and rural mixed layers (Roth, 2000).

- The *inertial sub-layer*: The flow and potential temperature are horizontally homogeneous but can vary in the vertical. The vertical fluxes of momentum, heat and moisture are horizontally homogeneous and uniform in the vertical and are taken to be equal to the spatially averaged surface value. Monin-Obukhov Similarity Theory may be applicable in this sub-layer (Rotach, 1993a). The lowest atmospheric level of numerical weather prediction models is usually assumed to lie within this layer.

- The *roughness sub-layer*: Adjacent to the rough surface the airflow is influenced by the individual roughness elements. The flow is horizontally heterogeneous, determined by local length scales such as the height of the roughness elements (buildings), their breadth or separation (e.g. Oke, 1988; Roth, 2000) and building shape (Rafailidis, 1997).

- The *canopy layer*: Either a separate sub-layer (Oke, 1987) or the lowest part of the roughness sub-layer below the height of the buildings. The flow is highly heterogeneous spatially and subjected to form drag (Belcher *et al.*, 2003). Most routine observations in urban areas are taken within this layer.

The vertical extent of each of these layers is the subject of several studies. A range of wind tunnel studies (Raupach *et al.*, 1980; Oke, 1987; Rafailidis, 1997; Cheng and Castro, 2002) show horizontal heterogeneity of the flow below 1.8–5 building heights. This estimate for the depth of the roughness sub-layer was seen to depend on the separation of the buildings (Raupach *et al.*, 1980) and building shape (Rafailidis, 1997). This implies that most of the observations taken in urban areas remain in the roughness sub-layer as supposed to the ideal location in the inertial sub-layer. The inertial sub-layer over urban areas is often thin (0.1 z_i, Roth (2000)). It is possible

that it may not exist in unstable conditions when the effects of surface heterogeneity are mixed further in the vertical (Roth, 2000) or when the building height varies and the roughness sub-layer is deepened (Cheng and Castro, 2002). The depth of the urban canopy layer is considered later.

1.2.1 The inertial sub-layer

The mean wind speed, U, and the turbulent nature of the flow in the inertial sub-layer over uniform terrain can be expressed in terms of Monin-Obukhov Similarity Theory. The assumptions of this theory are that a) the turbulent fluxes are constant with height, b) the mean flow is horizontally homogeneous and c) radiative transfer is negligible. The first two of these assumptions are not valid near to buildings and the continual variation of the urban surface implies that assumption b) will rarely be met even well above the surface. However in the absence of other theory, Monin-Obukhov Similarity Theory is commonly used as the basis for the analysis of the flow and turbulence in the urban inertial sub-layer (e.g. Roth, 2000). Correcting for the displacement of the mean flow, the vertical profile of the wind in the inertial sub-layer then takes the following form (e.g. Garratt, 1992)

$$U(z) = \frac{u_*}{\kappa}\left[\ln\left(\frac{z-d_T}{z_{0T}}\right) - \Psi_m\left(\frac{z-d_T}{L}\right)\right], \tag{1.1}$$

where z is the height above the ground, d_T is the zero-plane displacement of the mean flow, $u_* = (\tau/\rho)^{1/2}$ is the friction velocity measured in the inertial sub-layer, $\kappa(= 0.4)$ is von Kármán's constant, L is the Monin-Obukhov length and Ψ_m is the integrated stability function for momentum. z_{0T} is a constant of integration called the *bulk* or *effective roughness length*. The subscript $_T$ denotes that these values are representative of the total effects of the building array and not of the surface material. Physically d_T represents the mean height of momentum absorption by the surface and is often taken to be the depth of the canopy layer (Jackson, 1981).

The stability function Ψ_m and its counterparts for heat and moisture, Ψ_h and Ψ_q respectively, are empirical functions traditionally fitted to data (e.g. Dyer, 1967; Beljaars and Holtslag, 1991). These functions represent the effects of stability on the turbulent mixing and therefore on the vertical profiles of the mean flow, temperature and humidity in the inertial sub-layer. Ψ_m takes the value 0 in neutral conditions, is greater than 0 in unstable conditions and less than 0 in unstable conditions (e.g. Beljaars and Holtslag, 1991). Kanda *et al.* (2002) suggest that the form of the stability functions over an urban area is different to that over other surfaces.

The Monin-Obukhov length takes the form

$$L = -\frac{u_*^3}{\kappa \left(g/\theta_s\right) \left(H/\rho c_p\right)}, \tag{1.2}$$

where θ_s is the surface temperature, g is the acceleration due to gravity, ρ the density of air, c_p the specific heat capacity of air and H is the area-averaged sensible heat flux.

There are an increasing number of studies relating the roughness length and displacement height of an urban surface to the surface morphology (e.g. Raupach *et al.*, 1980; Bottema, 1996; Macdonald *et al.*, 1998) - see Raupach (1994) and Grimmond and Oke (1999a) for a review. The log-law (Equation (1.1)) has been observed over an urban area (Rotach, 1993a) and in wind tunnels over a variety of surface morphologies (Raupach *et al.*, 1980; Macdonald *et al.*, 1998; Barlow and Belcher, 2002; Cheng and Castro, 2002). Interestingly, Cheng and Castro note that the *spatially averaged* wind profile obeys the log-law down to building height.

The turbulence of the flow in the inertial sub-layer over an urban area remains poorly understood although a number of observational studies have been completed (e.g. Xu *et al.*, 1997). This is partly due to difficulty in observing at such a height above the ground, differences between observation techniques and a lack of a common framework to analyse these observations (Roth, 2000). Such work is needed to establish whether firstly, the inertial sub-layer exists from a turbulence view point (constant fluxes with height), and secondly to determine which if any of the current paradigms for the roughness and displacement of a real urban surface is applicable across the full range of urban morphologies.

1.2.2 The roughness sub-layer and canopy layer

Details of the flow and turbulence within the roughness sub-layer are needed for a variety of applications, notably pollution dispersion, building engineering and the urban energy balance. A focussed effort has been undertaken to observe and to understand the nature of the mean flow and turbulence within the urban roughness sub-layer. Quantitative understanding of the spatially averaged mean flow has advanced through the application of a modified Monin-Obukhov Similarity Theory (Rotach, 1993a,b) or applying a spatially-averaged dynamical approach (Macdonald, 2000; Coceal and Belcher, 2004). There are several key differences in the nature of the turbulence over ‘rural’ and urban sites. Firstly, there are significant dispersive stresses within the urban

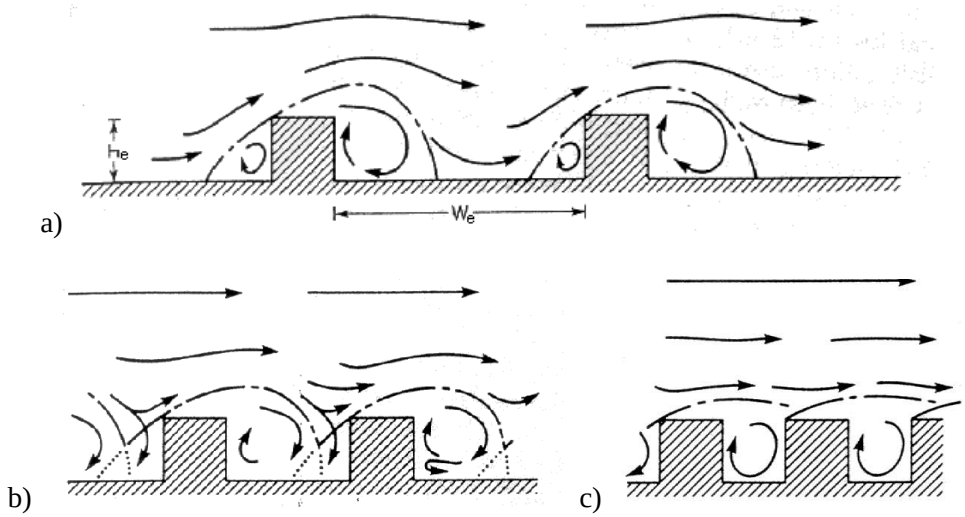

Figure 1.5: The flow regimes associated with air flow over building arrays with increasing canyon aspect ratio (h_e/w_e). (a) Isolated roughness flow; (b) Wake interference flow; (c) Skimming flow (adapted from Oke, 1987,1988).

canopy (Cheng and Castro, 2002). Secondly, the Reynolds stresses peak at or just above roof level indicating that this is a region of intense turbulence production (e.g. Rotach, 1993a). Finally, the turbulent spectrum over an urban area is altered. The peak in the energy spectrum is flattened with no single frequency dominating the power spectrum (Louka, 1998; Roth, 2000).

A range of qualitative pictures of the flow within the roughness sub-layer and around individual building configurations exist (e.g. Oke, 1987; Hunter *et al.*, 1992). Quantitative interpretation of these paradigms and the relation to observations is on going. Of particular concern is the weakness in the quantitative understanding of the physical processes governing the turbulent exchange at the top of canopy layer (e.g. Bentham and Britter, 2003), the coupling of the air above and within the building array (e.g. Louka *et al.*, 1998), the spatial variability of the turbulent intensity within the building array (e.g. Cheng and Castro, 2002) and the dependence of these features on the surface morphology.

A particularly useful paradigm in this work is the flow regimes of Oke (1987,1988), as shown in Figure 1.5. Restricting our consideration to the case of perpendicular flow incident on a series of urban street canyons; in the lee of each building a recirculating wake forms. An upstream bolster eddy can also form if the buildings are widely enough spaced. The *canyon aspect ratio*, the ratio of the buildings' height to their separation h_e/w_e, then determines whether the recirculating wake occupies all or part of the canyon cavity.

Three flow regimes then exist depending on the canyon aspect ratio, these are:

- The *isolated flow regime* occurs when the spacing of the buildings is wide. Oke (1987) suggests that for this regime the canyon aspect ratio, $h_e/w_e \lesssim 0.3$.
- The *wake interference regime* occurs at intermediate canyon aspect ratios. The recirculating wake interacts with the upstream displacement of the flow resulting from the downstream building.
- The *skimming flow regime* occurs at high canyon aspect ratios, $h_e/w_e \gtrsim 0.7$ (Oke, 1987). The main flow is displaced; turbulent exchange at the canyon top drives a recirculating flow within the canyon.

Few observational studies have considered the isolated flow regime. A small but increasing number of wind tunnel (e.g. Brown *et al.*, 2000) and numerical studies (e.g. Sini *et al.*, 1996) have considered the wake interference regime. In most studies the flow is seen to be highly intermittent making generalisation difficult. However as the morphology of many sub-urban areas falls into this flow regime further development both qualitative and quantitative is important.

Most studies consider the skimming flow regime, common in the city centres. A large number of wind tunnel (e.g. Raupach *et al.*, 1980), field experiment (e.g. Nakamura and Oke, 1988) and numerical studies (e.g. Mills, 1993) have concentrated on this flow regime with a range of motivating topics including the urban energy balance (e.g. Nunez and Oke, 1977) and pollution dispersion (e.g. Yamartino and Wiegand, 1986). Almost all studies indicate that the flow within the street canyon consists of an intermittent vortex and a shear layer at canyon top (e.g. Louka *et al.*, 2000). However this picture is for the mean sense only and can be disrupted by stability effects (e.g. Kim and Baik, 1999). An interesting feature of most numerical studies (e.g. Sini *et al.*, 1996) and some water tunnel studies (Baik *et al.*, 2000) is the formation of two or more counter rotating vortices as the canyon aspect ratio is increased beyond $h_e/w_e \sim 1.5$. Counter rotating vortices must occur when considering Stokes' flow dynamics in top lid driven cavity flows (Shankar and Deshpande, 2000). However, the presence of counter rotating vortices in a full scale urban street canyon has, to our present knowledge, not been observed. Deepening the canyon does however decrease the mean wind speed and turbulent intensity at street level.

The different physical processes occuring in these three flow regimes affect the turbulent transport of momentum and scalars. Very few studies have considered the turbulent characteristics of

the flow as the surface morphology is changed in a consistent manner (see Okamoto *et al.* (1993) and Brown *et al.* (2000) for exceptions). In particular, the consequent effects on the turbulent transport of scalars, important in determining the sensible and latent heat flux component of the energy balance has had little quantitative attention (see Barlow and Belcher (2002) and Narita (2003) for exceptions) and is the subject of Chapter 3.

Despite the obvious limitations of considering perpendicular flow to two dimensional geometry, limited understanding exists concerning the quantitative effects of alternative wind directions or building layouts on the mean flow and turbulent transport. An open question remains as to whether the results of these street canyon studies can be applied to cases where significant channelling of the flow (e.g. Nakamura and Oke, 1988) or canyon asymmetry (e.g. Nunez and Oke, 1977) occurs.

1.3 The urban energy balance

The energy balance of the surface is the physical process which couples the surface and the boundary layer. In a similar way that the surface roughness determines the Reynolds stresses, the drag on the flow and therefore the mean wind profile, the energy balance determines the surface fluxes of temperature and moisture and therefore the mean profile of potential temperature in the boundary layer and the surface temperature. Additionally, these two processes are linked. The Reynolds stresses are influenced by the stability of the atmosphere (Dyer, 1967). Conversely, the surface fluxes of heat and moisture depend on the turbulent nature of the boundary layer. The status of the boundary layer and energy balance of any surface are therefore intimately linked (Raupach, 2001). Over urban areas, where the turbulent intensities are higher than rural areas (Roth, 2000), this coupling is likely to be more important.

The energy balance of any point on a surface can be expressed as,

$$K_{\downarrow} - K_{\uparrow} + L_{\downarrow} - L_{\uparrow} - H - LE - G = 0. \tag{1.3}$$

This is an expression of the First Law of Thermodynamics (conservation of energy). $K_{\downarrow}$ and $K_{\uparrow}$ are the downward and upward, respectively, flux densities of the wavelength integrated shortwave radiation. $L_{\downarrow}$ and $L_{\uparrow}$ are the downward and upward, respectively, flux densities of the wavelength integrated longwave radiation incorporating emitted, transmitted and reflected radiation. H is the

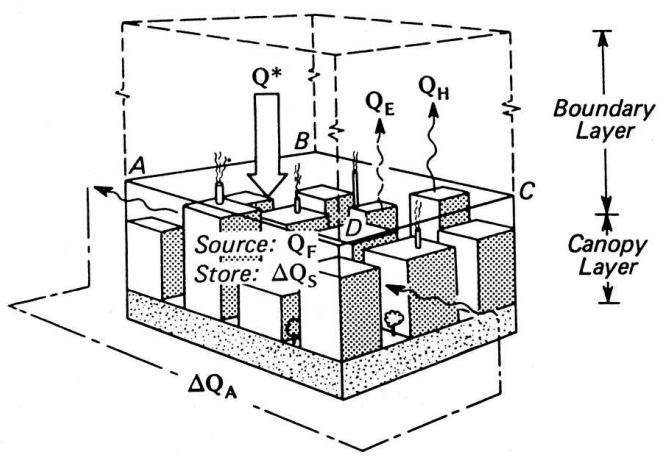

Figure 1.6: Schematic of the volumetric averaging approach to urban energy balance (after Oke, 1987). The base of the averaging volume is determined as the level across which there is negligible energy transfer on time scales of less than a day. Note the different notation: Q^* is the net radiation; Q_H the sensible heat flux; Q_E the latent heat flux; ΔQ_S storage; ΔQ_A the advective flux; and Q_F the anthropogenic heat flux.

turbulent flux density of sensible heat into the boundary layer, LE the turbulent flux density of energy associated with the evaporation of water (latent heat) into the boundary layer and G the flux density of energy into the substrate.

The complexity of the urban surface means that this equation cannot realistically be solved for every point on the urban surface and therefore requires approximation. Common approaches include considering the energy balance of the different building facets (e.g. Masson, 2000) or considering the energy balance of a volume incorporating buildings, intervening air and the underlying substrate (e.g. Oke, 1987; Grimmond *et al.*, 1991). In order to compare these approximations it is useful to to consider the balance of energy through a horizontal plane just above roof level (plane ABCD in Figure 1.6). This is denoted the *urban energy balance* or *bulk energy balance* and fluxes per unit planar area across this plane are denoted *bulk fluxes*. This is the balance of energy required in numerical weather prediction models. Relating the energy balance of the individual facets to the bulk energy balance requires additional assumptions, most commonly that the intervening air does not absorb or release energy. The urban energy balance is then the sum of the energy balances of the individual urban surfaces suitably weighted by surface area.

Applying the volumetric averaging approach (e.g. Oke, 1987) (see Figure 1.6) alters the form of the energy balance in three ways. Firstly, the absorption and release of energy by intervening air is incorporated with the integrated ground heat flux into a term known as *storage*. Secondly, advection through the volume can result in a non-zero flux of energy through the vertical edges of

the volume - this is the *advective* flux. Finally, the emission of anthropogenic energy in various forms can be explicitly incorporated into the energy balance. The anthropogenic heat flux can be locally instantaneously large (e.g. 400 W m^{-2} (Ichinose *et al.*, 1999)) but more commonly takes a modest value of the order of 10 W m^{-2} (Grimmond and Oke, 1995). The approach of volumetric averaging, however, due to its simple nature may prevent the physical processes governing the energy balance from being assessed. In particular, the different nature of the energy balance (e.g. Nunez and Oke, 1977) and surface temperatures (e.g. Voogt and Oke, 1998) of different surfaces is lost and the precise dependence on surface morphology cannot be examined.

Despite the practical difficulties in observing and interpreting the energy balance of an urban area a large number of observational campaigns have occurred. Most have studied the energy balance of temperate "western" style cities (e.g. Nunez and Oke, 1977; Cleugh and Oke, 1986; Grimmond, 1992; Grimmond and Oke, 1995, 1999b) including a number of long term studies, comparison studies between urban, sub-urban and rural sites and in a range of synoptic conditions. Fewer observations have been taken in tropical (wet or dry) regions, but observations have been taken in Mexico (Oke *et al.*, 1999; Garcia-Cueto *et al.*, 2003), a number of locations in Asia (e.g. Yoshida *et al.*, 1991) and recently in Africa (Offerle *et al.*, 2003). The comparisons between urban and rural energy balances are particularly useful as they highlight the principal effects of urbanisation on the energy balance. These are

- A greatly reduced latent heat flux - although immediately after rain events this can be the dominant term (Atkinson, 1985).
- An increased flux into the substrate during the day - this energy can then be released during the night maintaining surface warmth.
- The sensible heat flux may be slightly increased during the day but notably tends to peak later ($\sim$ 1 hour) and remains positive for several hours after sunset.
- Positive sensible heat fluxes can be maintained throughout the night (e.g. Oke *et al.*, 1999).
- The ground heat flux (storage) may peak slightly earlier ($\sim$ 1 hour).

The underlying physical processes responsible for these differences are as for the urban heat island, which is of course an observed symptom of these changes to the energy balance. The interpretation of the radiation terms of the energy balance of urban areas is well advanced (e.g.

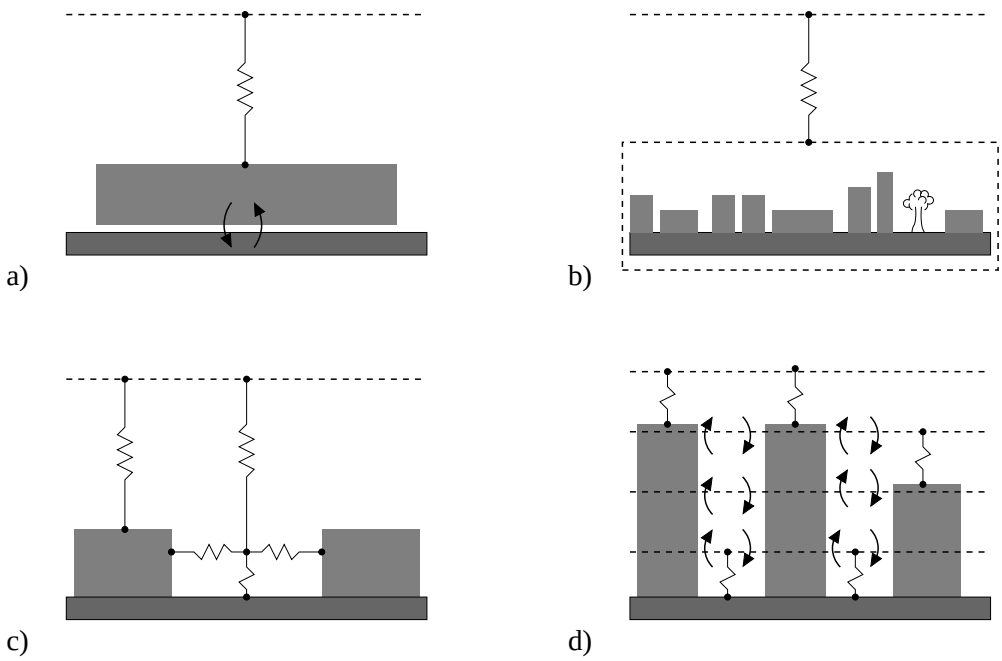

Figure 1.7: Schematic of the four basic approaches in modelling the urban energy balance. (a) Slab and 'concrete' canopy models (e.g. Best, 1998a); (b) volumetric averaging models (e.g. Grimmond *et al.*, 1991); (c) urban street canyon - single layer models (e.g. Masson, 2000); (d) urban street canyon - multi-layer models (e.g. Martilli *et al.*, 2002).

Johnson *et al.*, 1991). The degree of complexity used to calculate the radiation terms, however, varies between authors. The interaction between surface geometry and the radiation/storage balance at night under clear sky, light wind conditions has been fundamental in understanding the cause of urban surface heat islands (Oke *et al.*, 1991). The role of the turbulent fluxes and boundary layer state is not as well understood, despite the advance of tools such as source area modelling (Schmid, 1994). The role of surface morphology in determining the energy balance and its role in determining urban modifications to the urban climate therefore remains to be resolved.

A range of methods to model the energy balance of urban areas exist, depending on their intended usage and the complexity required. Figure 1.7 shows a schematic of the four principal types used across a range of applications. The simplest models are slab models (Figure 1.7(a)). The urban surface is approximated as one surface but with surface characteristics appropriate for urban areas (e.g. Myrup, 1969; Carlson and Boland, 1978). More complex versions of this model type approximate the urban surface as a canopy (e.g. Best, 1998a; Vu *et al.*, 2002). The differences between these two cases lie in the methods used to couple the slab to the underlying surface. These models commonly do not explicitly incorporate surface morphology.

A range of statistical models exist for the volume-averaged energy balance of urban areas (Fig-

ure 1.7(b)). Most notable of these is the Objective Hysteresis Model and its successors (Grimmond *et al.*, 1991; Grimmond and Oke, 1999b, 2002). These models statistically parameterise the relation between the evolution of the net radiative flux and the storage terms and then subsequently partition the residual into the turbulent fluxes. The effects of surface morphology are incorporated into the statistically determined coefficients. The statistical determination of the model coefficients implies that these models cannot be ported between different cities without reassessing these coefficients.

A number of physically based models have been developed with the aim of incorporation into mesoscale numerical weather prediction models. The first class of these are single layer models. These use a generic unit of the urban surface placed entirely below the level of the lowest atmospheric model level (Figure 1.7(c)). The majority of these models use the urban street canyon as the generic unit of the urban surface (e.g. Masson, 2000) though arrays of cubes have been used (e.g. Kawai and Kanda, 2003). The urban energy balance is comprised of the averaged energy balance of (the parts of) the individual building facets. The effects of surface morphology on the energy balance of the individual building facets and the entire urban energy balance is explicitly incorporated in the formulation of the terms of the energy balance. This is the approach taken in this thesis.

The final type of model (Figure 1.7(d)) also uses a generic unit of the urban surface but allows the unit to intersect several atmospheric model levels (e.g. Martilli *et al.*, 2002; Martilli, 2002). The influence of the urban surface is then spread in the vertical in a more realistic way. Again the influence of surface morphology is incorporated explicitly. In both of the final cases the morphological properties of the surface used represent the average of these properties on a spatial scale appropriate to the resolution of the mesoscale model, i.e. the neighbourhood or city scales, so these models cannot in practice capture the fine detail of the surface.

Three issues apply to all of these models. Firstly, the turbulent fluxes determine the coupling of the surface and the boundary layer but their dependence on surface morphology and boundary layer stability is not well known or understood. Given that most observations are taken in the atmosphere this is serious obstacle to the realistic validation of models of the urban energy balance. Secondly, these models require a number of input parameters (e.g. surface heat capacities). It is not known how many of these parameters relate to the observable quantities on the ground. This is especially important given the different scales on which the surface properties vary and on which these models are likely to be employed. Finally, few of these models have been run, and

subsequently validated, in conjunction with boundary layer models. Given the coupled nature of the boundary layer and energy balance the sensitivity of these models, to surface morphology for instance, may differ when run in the coupled and surface only senses. This work addresses some of these issues.

Thesis structure

This present study focusses on the influence of surface morphology on the energy balance and boundary layer of urban areas. The aims of this work are three-fold:

- To investigate the impacts of surface morphology on all parts of the surface energy balance and boundary layer.
- To determine which of the urban modifications to the local climate can be attributed to the combined effects of surface morphology and to suggest physical explanations for those that cannot, and finally
- to determine methods to incorporate surface morphology into operational numerical weather prediction models.

Two approaches are used to investigate these aims. Firstly, analytic, experimental and process based modelling is used to investigate the morphological dependence of the individual terms of the urban energy balance. Secondly, numerical studies are used to assess the impact of the effects of surface morphology on the boundary layer.

In more detail:

- Chapter 2 considers the impact of surface geometry on the exchange of diffuse radiation in the canopy layer. A simple model to calculate net radiative flux densities is presented and compared to commonly used alternatives.
- Chapter 3 considers the impact of surface morphology on the turbulent fluxes of scalars from an urban surface. Wind tunnel experiments and modelling are used to highlight the important physical processes governing the turbulent transport.
- Results from the previous chapters are used to formulate an urban energy balance model in Chapter 4. The urban energy balance is comprised of the facet-averaged energy balances

for the four facets of an urban street canyon. This energy balance model is then coupled to a one dimensional boundary layer model, and numerical studies are used to investigate the full impacts of surface morphology on the urban energy balance and boundary layer.

- Chapter 5 considers the degree of complexity needed within the urban energy balance model. The urban energy balance model developed in Chapter 4 is compared to two approximate models which could be implemented into operational weather prediction models.

- Chapter 6 considers the importance of advection in determining the urban modifications to the local climate. Numerical simulations incorporating the advection of a boundary layer from a rural site to an urban site are compared to previous results with a particular emphasis on the maintenance of positive nocturnal sensible heat fluxes.

- Chapter 7 summarises and discusses the results of the work and gives suggestions for future work, noting areas of uncertainties.

- The two appendices give details of the methods used to calculate the solar radiative forcing in the thesis (Appendix A) and the turbulence closure method used in the boundary layer model in Chapters 4, 5 and 6 (Appendix B).

At all points the results of the work are related to observations within urban areas and the implications for operational numerical weather prediction models are highlighted.

CHAPTER TWO

Radiative exchange in an urban street canyon

2.1 Introduction

The effect of surface morphology on the radiation balance is a key to understanding the energy balance of an urban area. The associated reduction in nocturnal radiative cooling is a principal reason for urban-rural night time surface temperature differences (Oke, 1987; Oke *et al.*, 1991). However, quantitative evaluation of the radiation balance in an urban area is complicated in three main ways. Firstly, the heterogeneity of building size, orientation and surface material properties makes the establishment of bulk properties such as the emissivity of the urban area difficult. Secondly, geometry alters the magnitude of the incoming fluxes through a variety of processes. Thirdly, (multiple) reflections of radiation may be an important part of the radiation balance of an urban area unlike that of a horizontal surface.

The urban street canyon (Nunez and Oke, 1977) is often used as the generic unit of the urban surface within many surface energy balance models for urban areas (Arnfield, 1982; Johnson *et al.*, 1991; Mills, 1993; Sakakibara, 1996; Arnfield and Grimmond, 1998; Arnfield, 2000; Masson, 2000; Kusaka *et al.*, 2001). Even for a simple morphological construct such as the urban street canyon there are differences in how the radiation balance has been calculated. The radiation balance for the mid-points on each building facet can be formulated and used as representative of the building facets (Johnson *et al.*, 1991). This method has the advantage of ease of validation. The average radiation balance for (parts of) the building facets (area averages) can be formulated (Verseghy and Munro, 1989 a,b; Kobayashi and Takamura, 1994; Masson, 2000; Kusaka *et al.* 2001) and used as representative of the total effect of the building facets. This method better conserves total energy. In both cases, a range of methods are used to calculate the radiative transfer.

Reflected radiation has been observed to lead to secondary peaks in the net radiation received

at the two walls of an urban canyon (Nunez and Oke, 1977). There are a variety of methods used to calculate these reflections, and in the number of reflections considered, for both shortwave and longwave radiation. Common methods include ignoring all reflections (Noilhan, 1981; Sakakibara, 1996) or considering only one reflection (Johnson *et al.*, 1991; Kobayashi and Takamura, 1994; Masson, 2000 - longwave part; Kusaka *et al.*, 2001). More complex methods include increasing the number of reflections considered until convergence of the net radiation (Arnfield, 1982), solving the full geometric series (Verseghy and Munro, 1989 a,b; Masson, 2000 - shortwave radiation) or performing Monte Carlo simulations of the path of photons in the canyon (Aida and Gotoh, 1982; Kobayashi and Takamura, 1994; Pawlak and Fortuniak, 2002).

Verseghy and Munro (1989 a,b) showed, for two cases, that neglecting canyon geometry, multiple reflections, and additional physics such as the absorption, emission and scattering of radiation within the canyon and the non-isotropy of diffuse solar radiation could lead to appreciable errors in the radiation terms for an urban street canyon. By comparing Monte Carlo simulations and a one reflection model, Kobayashi and Takamura (1994) showed that the effects of reflections were more important at higher aspect ratios and lower emissivities. Pawlak and Fortuniak (2002) show that Monte Carlo simulations and solving the full geometric series give similar results for a specific case. Johnson *et al.* (1991) show that the error associated with ignoring two or more reflections in a closed system of isothermal surfaces with identical emissivities is 0.3% at an emissivity of 0.95. However, a careful consideration of the errors resulting from neglecting reflections of radiation for a full range of cases is needed.

In summary, there exists a range of methods to calculate the net radiation of an urban area, particularly those based on the urban street canyon, but there is little knowledge of which approximations are required across the wide range of surface parameters encountered in an urban area. In particular, how do these methods compare across a range of urban geometries and material properties? This knowledge is needed to determine when each of these methods is valid and what complexity of solution is needed especially given the need to keep the numerical complexity of surface energy balance models as low as possible.

Hence this chapter focusses on the exchange of diffuse radiation within an urban canyon to establish when commonly used methods are valid. A generic method is introduced for the full solution of the exchange of diffuse radiation in a closed system of surfaces, developed originally by Sparrow and Cess (1970) and applied to an urban street canyon by Verseghy and Munro (1989 a,b) and Pawlak and Fortuniak (2003). To isolate the effects of reflections, the effects of absorption,

emission and scattering of radiation by the canyon volume air, and hence the dependence of the radiation balance on the full surface energy balance, are not considered. For the purposes of this chapter the solution calculated with the Sparrow and Cess (1970) method is taken to be the 'exact' solution. Two commonly used approximations, no reflections and one only reflection of radiation, are compared to this exact solution over a range of canyon aspect ratios and surface material properties. Comparison of results obtained with the three methods allows an assessment of the applicability of the approximations.

2.2 Methodology

Sparrow and Cess (1970) have developed a method to find the solution to the diffuse radiative exchange between the facets of closed system of surfaces surrounding a non-absorbing medium. This method is applied here to an urban street canyon which is taken as the generic unit of the urban surface. The radiative flux densities are assumed to be uniform across each of the surfaces. The emission and reflection of radiation is assumed to be diffuse and according to the surface material emissivity and albedo. The medium between the surfaces is assumed to be radiatively non-absorbing. The exchange of longwave radiation and the diffuse component of the shortwave radiation within an urban street canyon can be calculated using this method provided the facet-averaged fluxes are considered. The direct component of the solar radiation cannot be calculated using this method, but reflections of the direct component of solar radiation can.

The absorption, emission and scattering of radiation by the air can be significant even over the moderately short distances within an urban canyon (Verseghy and Munro, 1989 a,b). A full radiation model may be needed to account for these processes. This chapter, however, concentrates on the impact of reflections on the radiation balance so these processes are neglected here. Nakamura and Oke (1988) and Voogt and Oke (1998) show that the surface temperature may not be uniform across the individual facets of an urban street canyon. However, the relative change in surface temperature across a facet is small so that the facet averaging and radiation balance calculations can be interchanged without imposing a large error ($\approx 0.3\%$ for a ± 5K variation across each facet).

2.3 Exchange of diffuse radiation

2.3.1 Fundamentals of radiative exchange

Surface morphology affects the radiation balance by altering the magnitude and source of the radiative flux densities incident on each surface. The effects of surface morphology on the radiative exchange between a closed system of surfaces surrounding a non-absorbing medium are expressed in terms of the *shape factors* for the system of surfaces.

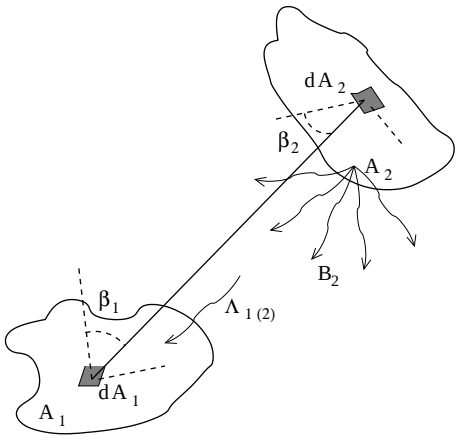

Figure 2.1: Schematic of the shape factor for an arbitrary pair of surfaces.

Let B_j be the total facet-averaged diffuse radiative flux density away from a surface j. Let $\Lambda_{i(j)}$ denote the flux density of diffuse radiation onto surface i originating directly from surface j. These two flux densities are related by the shape factor, $F_{i\,j}$, of the two surfaces, namely

$$\Lambda_{i(j)} = F_{i\,j} B_j. \tag{2.1}$$

Figure 2.1 shows a schematic for the configuration used to derive the shape factor between two surfaces. The shape factor for an arbitrary pair of surfaces can be derived (Sparrow and Cess, 1970) as

$$F_{i\,j} \;=\; \frac{1}{A_i} \int\limits_i \int\limits_j \frac{\cos\beta_i \,\cos\beta_j}{\pi r^2}\; \mathrm{d}A_j \;\mathrm{d}A_i, \tag{2.2}$$

where $\mathrm{d}A_i$ and $\mathrm{d}A_j$ are elemental parts of the (larger) surface i and j respectively and A_i is the area of surface i. The line connecting the two elemental areas is of length r, with β_i and β_j being

the angles between this line and the normals to the surfaces dA_i and dA_j respectively. $F_{i\,j}$ is a function of the separation and relative orientation of the two surfaces i and j only.

2.3.2 Shape factors for an urban canyon

The shape factors required when applying the Sparrow and Cess (1970) method to an urban street canyon are those between two equally sized, in-line, parallel planes and between two perpendicular planes sharing a common edge, as shown in Figure 2.2. Shape factors for the radiative exchange between any two of the canyon surfaces can be derived from one of these two generic types.

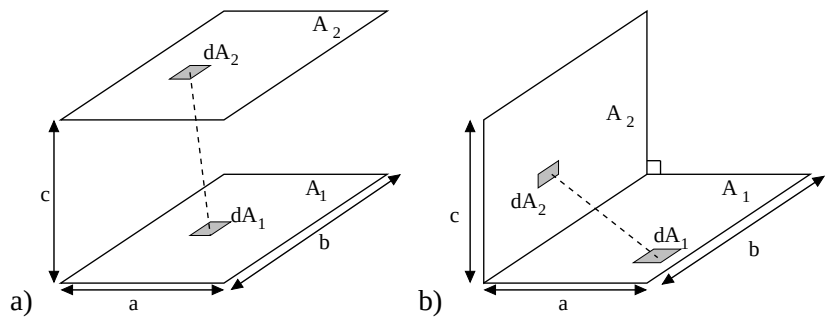

Figure 2.2: Schematic of the shape factors for the urban street canyon. (a) two parallel in-line planes; (b) two perpendicular planes.

For the case of parallel planes (Figure 2.2(a)) and allowing $b \rightarrow \infty$ (the two dimensional canyon case), Equation (2.2) yields (Sparrow and Cess, 1970)

$$\begin{aligned} F_{A_1\,A_2} &= \frac{1}{X}\left[\left(1+X^2\right)^{1/2}-1\right], \\ \text{where } X &= a/c. \end{aligned} \tag{2.3}$$

For the case of two perpendicular planes (Figure 2.2(b)) and allowing $b \rightarrow \infty$, Equation (2.2) yields

$$\begin{aligned} F_{A_1\,A_2} &= \frac{1}{2}+\frac{1}{2X}-\frac{1}{2X}\left[1+X^2\right]^{1/2}, \\ \text{where } X &= a/c. \end{aligned} \tag{2.4}$$

Denoting the street, wall and ‘sky’ facets by st, wl and sk respectively, the shape factors for the

urban street canyon system are then determined from Equations (2.3) and (2.4) as

$$F_{sk\,st} = F_{st\,sk} = \left(1 + \left(\frac{h_e}{w_e}\right)^2\right)^{\frac{1}{2}} - \frac{h_e}{w_e}, \tag{2.5}$$

$$F_{w1\,w2} = \left(1 + \left(\frac{w_e}{h_e}\right)^2\right)^{\frac{1}{2}} - \frac{w_e}{h_e}, \tag{2.6}$$

$$F_{st\,w1} = \frac{1}{2}(1 - F_{st\,sk}), \tag{2.7}$$

$$F_{w1\,st} = F_{w1\,sk} = \frac{1}{2}(1 - F_{w1\,w2}). \tag{2.8}$$

The shape factors for an urban street canyon vary widely for the parameters encountered in real cities as shown in Figure 2.3. The radiative exchange in a 'suburban canyon' ($h_e/w_e \approx 0.2$)

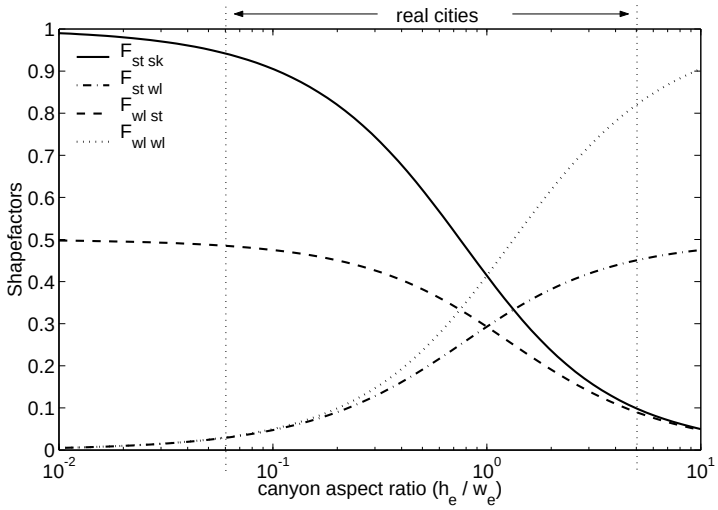

Figure 2.3: Shape factors for the urban street canyon.

is similar to that of a flat surface ($F_{sk\,st}$ is near one and $F_{w1\,w2}$ and $F_{st\,wl}$ are near zero) with most of the exchange of diffuse radiation occuring between the sky and street facets. The radiative exchange of city-centre canyons ($h_e/w_e > 1$) occurs mostly between the two wall facets and between the walls and street. This change in the radiative exchange is a main cause of the urban modification of the radiation balance.

Shape factors can also be formulated for infinitesimal parts of each facet (Johnson and Watson, 1984; Steyn and Lyons, 1985). These are also known as *viewfactors* (e.g Oke, 1987). There can be a large variation of viewfactor with position on each facet (Steyn and Lyons, 1985). This

highlights the need to use the facet averaged shape factors and not representative points within energy balance calculations. The small relative variation in surface temperature across each facet implies that the combination of varying shape factor and surface temperature does not produce large errors when the facet averaging and radiation balance calculations are interchanged ($\approx 1\%$).

2.3.3 Exact solution

The exact solution to the exchange of diffuse radiation within a closed system of surfaces is calculated by developing a system of equations for the total radiative flux density away from each of the surfaces (Sparrow and Cess, 1970). The exact method is illustrated here in the context of the longwave radiation; the shortwave radiation is analogous with $(1 - \alpha_i)$ replacing ε_i throughout; here ε_i is the surface emissivity, α_i the surface albedo (full details in Sparrow and Cess (1970)). There are a range of radiative flux densities on the ith facet; the emitted, Ω_i, total incoming, Λ_i, total outgoing, B_i. and net, Q_i. These flux densities are related by

$$\Lambda_i = \sum_j F_{i\,j} B_j, \tag{2.9}$$

$$B_i = \Omega_i + (1 - \varepsilon_i)\Lambda_i, \tag{2.10}$$

$$Q_i = \Lambda_i - B_i. \tag{2.11}$$

The quantity of interest, namely the net component of the radiation for the ith facet, Q_i, involves the total outgoing radiation from the other facets, i.e. all of the B_j's.

Here the Equations (2.9)-(2.11) are solved by expressing them in matrix form, namely

$$B_i = \Omega_i + (1 - \varepsilon_i) \sum_j F_{i\,j} B_j, \tag{2.12}$$

$$\Omega_i = \sum_j \Gamma_{ij} B_j, \tag{2.13}$$

$$\text{where } \Gamma_{ij} = \delta_{ij} - (1 - \varepsilon_i) F_{i\,j}.$$

Since the matrix Γ_{ij} always has an inverse, ψ_{ij}, Equation (2.13) can be inverted to give the

total outgoing radiative flux density, and hence the net radiative flux density, for each facet,

$$B_i = \sum_j \psi_{ij}\Omega_j, \tag{2.14}$$

$$Q_i = \begin{cases} \sum_j F_{i\,j}B_j - \Omega_i, & \text{if } \varepsilon_i = 1, \\ (\varepsilon_i B_i - \Omega_i)/(1-\varepsilon_i), & \text{otherwise.} \end{cases} \tag{2.15}$$

The matrix Γ is inverted numerically for each value of h_e/w_e and ε_i. Equation (2.15) can be expressed in matrix form for ease of use as part of a surface energy balance model.

2.3.4 Approximate solutions

Most previous studies have developed approximate solutions to Equations (2.9)-(2.11). Equations (2.9) and (2.10) show that the net radiative flux density for a particular facet is an infinite geometric series in $(1-\varepsilon)$. Previous studies approximate this infinite series by truncating after a finite number of terms. Noilhan (1981) neglects all reflections; whereas Kusaka *et al.* (2001) retains only one reflection. Ignoring all reflections (denoted $\mathcal{R}^0$) is formally the approximation resulting from ignoring all terms of order $(1-\varepsilon)$ and higher. Retaining only one reflection (denoted $\mathcal{R}^1$) is formally the approximation resulting from ignoring all terms of order $(1-\varepsilon)^2$ and higher. The corresponding forms of Equation (2.15) after these approximations have been made are

$$\mathcal{R}^0: \quad Q_i^0 = \varepsilon_i \sum_j F_{i\,j}\Omega_j - \Omega_i, \tag{2.16}$$

$$\mathcal{R}^1: \quad Q_i^1 = \varepsilon_i \sum_j F_{i\,j}\left(\Omega_j + (1-\varepsilon_i)\sum_k F_{j\,k}\Omega_k\right) - \Omega_i. \tag{2.17}$$

2.3.5 Application to the urban street canyon

The application of the three methods to an urban street canyon requires the specification of the emitted flux densities and emissivities for each of the facets of the canyon system. The emitted flux density from each of the canyon facets is calculated using Stefan's law (top line Equation (2.18) below). The emissivity of the sky facet is one and the emitted flux density for the sky

facet is the downwelling longwave radiation $L_{\downarrow}$. With these specifications, consider again the approximate solutions given in Section 2.3.4. The emitted flux densities from the canyon facets are of order ε and the downwelling longwave radiation is of order one. Equations (2.16) and (2.17) must then be adapted to keep the approximations consistent in powers of ε. To do this an extra reflection of the downwelling radiation must be retained compared to the number of reflections of the radiation emitted from the canyon facets. The consistent approximate solutions for the net radiation are then

$$\Omega_i = \begin{cases} \varepsilon_i \sigma T^4 & \text{for } i = st, wl \\ L_{\downarrow} & \text{for } i = sk \end{cases}, \tag{2.18}$$

$$Q_i^0 = \varepsilon_i \sum_j F_{i\,j} \left(\Omega_j + (1-\varepsilon_j) F_{j\,sk} L_{\downarrow}\right) - \Omega_i, \tag{2.19}$$

$$Q_i^1 = \begin{array}{l} \varepsilon_i \sum\limits_j F_{i\,j} \;\; \Omega_j \; - \; \Omega_i + \\ \qquad \varepsilon_i \sum\limits_j \;\; F_{i\,j}(1-\varepsilon_j) \left(\sum\limits_k F_{j\,k} \left(\Omega_k + (1-\varepsilon_k) F_{k\,sk} L_{\downarrow}\right) \right) \end{array}. \tag{2.20}$$

Note, obviously, all solutions agree when $\varepsilon_i = 1$ for all surfaces. Comparison of the three solutions, namely Equations (2.15), (2.19) and (2.20), are shown next.

2.4 Comparison of the exact solution with the approximations

A comparison of results for the net longwave radiation, Q_i, for each facet from an individual case is now considered. The absolute values and differences between the three methods depend on the case considered but the features highlighted are robust. Consider the particular case when the emitted flux densities are prescribed by setting the facet surface temperatures at 295 K and the downwelling longwave radiation is 275 W m^{-2}. These values are chosen to be realistic for mid-latitude regions. Each of the canyon facets has the same emissivity. Results are described for a range of canyon aspect ratios, h_e/w_e, and emissivities, ε.

2.4.1 Exact solution - longwave radiation

The net radiative flux density from the canyon facets gives a measure of how the surface temperatures of the canyon facets would change for the case considered. Figure 2.4 shows the weighted

(by surface area) average of the net radiative flux density for the three canyon facets calculated using the exact solution. Note the tendency towards the flat case as the canyon aspect ratio decreases, the tendency to zero net radiation when $\varepsilon \rightarrow 0$ and the decrease in the magnitude of the net radiative flux density as the aspect ratio increases. The transition between a net radiative flux density which is close to that of a flat surface to that of a highly convoluted surface is rapid around $h_e/w_e = 0.5$. This illustrates the large impact that surface geometry has on the net radiative flux density and thus the sensitivity to geometry of the radiation balance of the urban street canyon. The range of emissivities for natural materials is $\varepsilon > 0.5$.

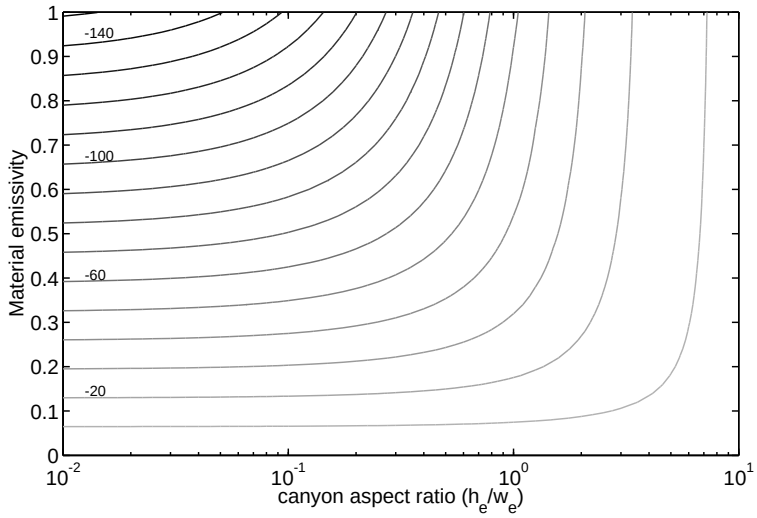

Figure 2.4: Weighted by surface area average of the net longwave radiative flux density from the three canyon facets using the exact solution - contours every 10 W m^{-2} from -150 to -10 W m^{-2} (light).

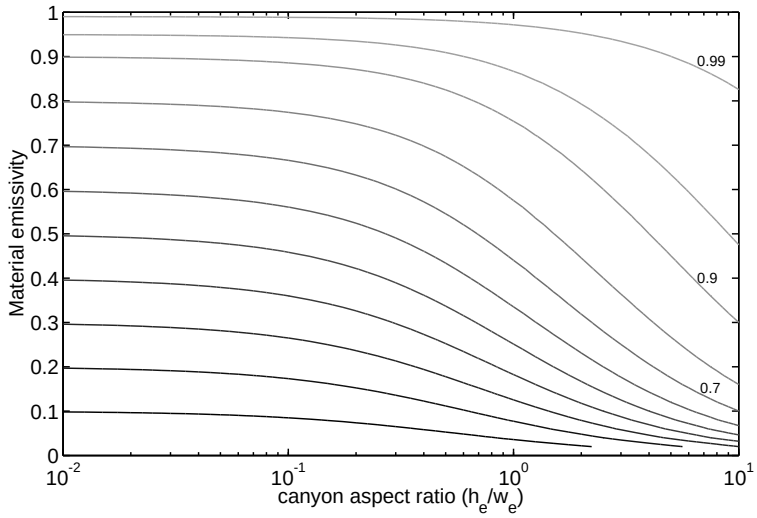

Figure 2.5: Canyon top net radiative flux density normalised by the net radiative flux density of a horizontal blackbody surface - contours every 0.1 from 0.1 (dark) to 0.9 then 0.95 and 0.99 (light).

The net radiative flux density across the top of the canyon gives a measure of the *effective* emissivity of the canyon system. *Effective* in this sense means the value the parameter would have to take to give the same canyon top net radiative flux density if the underlying surface were horizontal. Figure 2.5 shows the net radiative flux density at canyon top normalised by the net radiative flux density of a horizontal blackbody surface at 295 K. An increase in canyon aspect ratio increases the magnitude of the net radiative flux density across the top of the canyon thus increasing the radiation emitted to space. This increase in net radiative flux density is due to the larger surface area of the canyon; the net radiative flux density of individual canyon facets is reduced in magnitude compared to the flat case because the incoming radiation is now partly from the other canyon facets instead of the sky. These effects of canyon geometry on the exchange of diffuse radiation between the facets on an urban street canyon will be referred to as the *shape factor effect* throughout this work.

2.4.2 Approximate methods - longwave radiation

Figures 2.6 and 2.7 show the weighted average of the net radiative flux density for the three canyon facets for the same case but calculated using the $\mathcal{R}^0$ and $\mathcal{R}^1$ methods respectively. When $h_e/w_e = 0$ there is no radiative exchange between the surfaces; when $\varepsilon = 0$ there is no radiation emitted or absorbed and when $\varepsilon = 1$ there is no radiation reflected. In these three cases all three methods must be equivalent as seen in Figures 2.4, 2.6 and 2.7. Differences between the methods occur as the canyon aspect ratio increases and when the emissivity of the canyon facets takes intermediate values.

Figures 2.6 and 2.7 show that the two approximations possess an unphysical feature as the canyon aspect ratio increases. The exact solution shows that the magnitude of the weighted average net radiative flux density decreases monotonically as the canyon aspect ratio increases or ε decreases. In contrast the approximations show minima as ε varies and do not tend to zero for all ε as the canyon aspect ratio increases. This shows that reflections play an important role in the exchange of diffuse radiation when the aspect ratio increases or the surface material becomes grey-body.

The minima always occur in these approximations. For instance, the $\mathcal{R}^0$ approximation has the

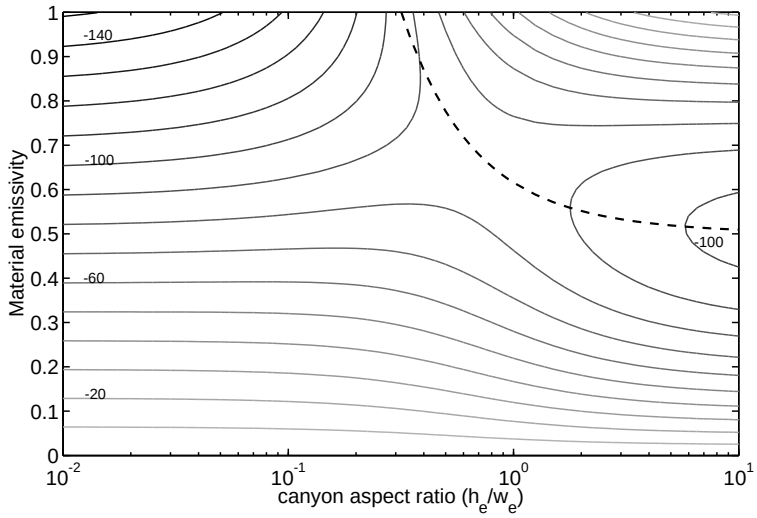

Figure 2.6: Weighted by surface area average of the net longwave radiative flux density for the three canyon facets using the $\mathcal{R}^0$ approximation - contours every 10 W m^{-2} from -150 – -10 W m^{-2} (light). Locus of minima marked by dashed line.

following form for the net radiative flux density of the street facet, Q^0_{st},

$$Q^0_{st} = \varepsilon F_{st\,sk} L_\downarrow + \varepsilon(1 - F_{st\,sk})\varepsilon\sigma T^4 + 2\varepsilon F_{st\,wl} F_{wl\,sk}(1-\varepsilon)L_\downarrow - \varepsilon\sigma T^4. \tag{2.21}$$

The four terms represent the directly absorbed downwelling radiation, the directly absorbed radiation which was emitted by the walls, the absorbed downwelling radiation that has undergone one reflection (off either wall) and the emitted longwave radiation. The third term is the term included for a consistent approximation in ε.

Differentiation of Equation (2.21) shows that there is a minimum in the net radiative flux density for the street when $\varepsilon = \varepsilon^0_{stm}$. The value of the net radiative flux density for the street along this locus is given by Q^0_{stm} where,

$$\varepsilon^0_{stm} = \frac{\left[F_{st\,sk} + 2F_{st\,wl}F_{wl\,sk}\right] L_\downarrow - \sigma T^4}{2\left[2F_{st\,wl}F_{wl\,sk}L_\downarrow - (1 - F_{st\,sk})\sigma T^4\right]}, \tag{2.22}$$

$$Q^0_{stm} = \frac{\left(\left[F_{st\,sk} + 2F_{st\,wl}F_{wl\,sk}\right] L_\downarrow - \sigma T^4\right)^2}{4\left[2F_{st\,wl}F_{wl\,sk}L_\downarrow - (1 - F_{st\,sk})\sigma T^4\right]}. \tag{2.23}$$

The locus has limits of $\varepsilon^0_{stm} \to \infty$ as $h_e/w_e \to 0$ and $\varepsilon^0_{stm} \to \frac{1}{2}$ as $h_e/w_e \to \infty$ with a corresponding limit of $Q^0_{stm} \to -\frac{1}{4}\sigma T^4$ as $h_e/w_e \to \infty$. The net radiative flux density on this

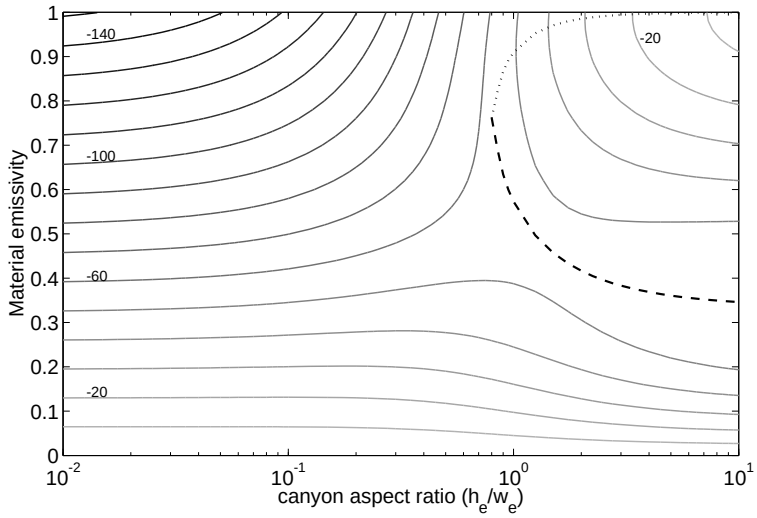

Figure 2.7: Weighted by surface area average of the net longwave radiative flux density for the three canyon facets using the $\mathcal{R}^1$ approximation - contours every 10 W m^{-2} from -150 to -10 W m^{-2} (light). Locus of minima marked by dashed line; locus of maxima marked by dotted line (real-only parts shown).

locus is incorrect as the canyon aspect ratio increases. The inclusion of the additional term to keep a consistent cutoff in ε does not affect this result qualitatively.

Similar analysis of the net radiative flux density for the walls, Q^0_{wl}, shows a similar locus of minima. The net radiative flux density for the wall facets on this locus is the same as that of the street facet on the locus ε^0_{stm} when $h_e/w_e \to \infty$. As the canyon aspect ratio becomes small the limits on the locus are $\varepsilon^0_{wlm} \to 1$ and $Q^0_{wlm} \to \frac{1}{2}(L_\downarrow - \sigma T^4)$ which is correct. The weighted average net radiative flux density for the three canyon facets will therefore also always have a locus of minima, as is shown in Figure 2.6. The locus marks the minima when varying ε, i.e. it will cross contours of the net radiative longwave flux density when these contours are parallel to the ε axis.

The minimum for the $\mathcal{R}^1$ method affects a smaller range of canyon aspect ratios than that of the $\mathcal{R}^0$ method. The cubic nature of the expressions for Q^1_{st} and Q^1_{wl} resists similar simple analysis (Abaramowitz and Stegun, 1973) but gives loci of minima and maxima as shown in Figure 2.7.

2.4.3 Errors of the approximate solutions

Figures 2.8 and 2.9 show the relative error of the $\mathcal{R}^0$ and $\mathcal{R}^1$ methods, respectively, compared to the exact solution. The relative error is chosen as this measure of the error is not particular to the case considered here. The approximate methods always overestimate the magnitude of the net

radiative flux and can be an order of magnitude incorrect. For typical emissivities, e.g. $\varepsilon = 0.9$, the $\mathcal{R}^0$ method can be 10% or more incorrect, the $\mathcal{R}^1$ method 5% or more incorrect. As expected the $\mathcal{R}^1$ method is the better approximation for all canyon aspect ratios and emissivities.

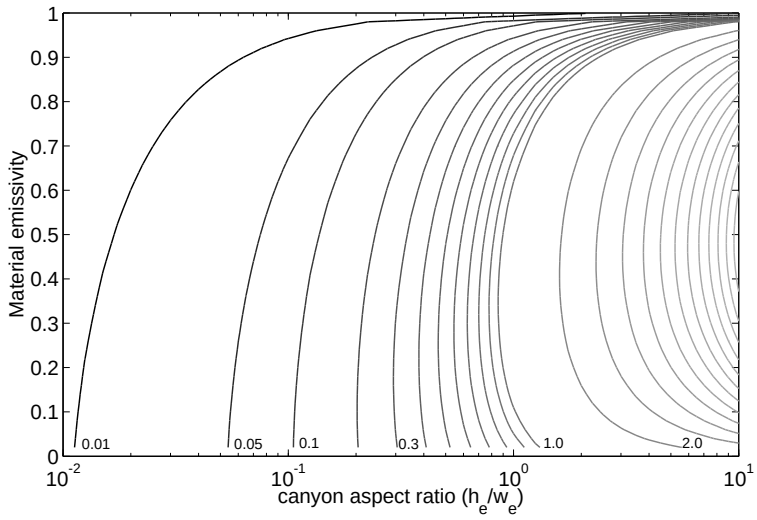

Figure 2.8: Relative error of the weighted average of net radiative flux density using the $\mathcal{R}^0$ approximation - contours at 0.01 (dark), 0.05, every 0.1 from 0.1–1.0 then every 1.0.

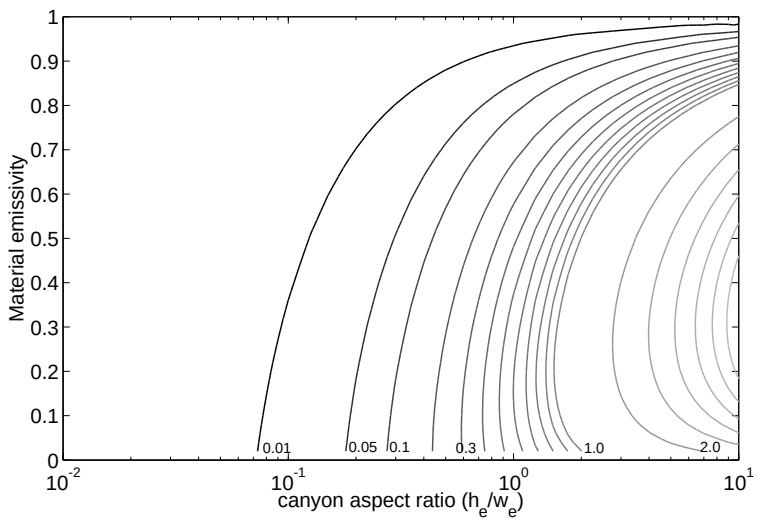

Figure 2.9: Relative error of the weighted average of net radiative flux density using the $\mathcal{R}^1$ approximation - contours at 0.01 (dark), 0.05, every 0.1 from 0.1–1.0 then every 1.0.

The errors of the approximations are very sensitive to the material emissivity in the range of realistic emissivities (e.g. 0.7 – 0.9 for concrete, ≈ 0.95 for asphalt, Oke (1987)). For instance, the relative error of the $\mathcal{R}^0$ method at a canyon aspect ratio of $h_e/w_e = 1$ and $\varepsilon = 0.95$ is 20%. A small uncertainty in the emissivity of the material property, $\varepsilon = 0.95 \pm 0.02$, leads to

a range of relative errors of 10–30%. A small uncertainty in the surface material emissivity can therefore have an unphysically large impact on the accuracy of the net radiation calculations if these approximations are used.

The loci of minima from the two methods give natural conditions for when the approximations can be considered to be valid. Regions of $h_e/w_e - \varepsilon$ space which show these unphysical features are where the approximate methods deviate significantly from the exact solution. Although these are case dependent, broad conclusions are that the $\mathcal{R}^0$ method should not be used for canyon aspect ratios greater than 0.3, the $\mathcal{R}^1$ method should not be used for canyon aspect ratios greater than 0.8. Additionally the dependence of the relative error of the two methods on the material emissivity suggests that these thresholds should be lowered when considering materials with a low emissivity. For full applicability only the exact solution is valid.

Allowing the emissivity of the different facets to vary from each other does not qualitatively change these relative error patterns. The approximations continue to perform well for high emissivities and low canyon aspect ratios. For lower emissivities and higher aspect ratios the relative error of each approximation is close to but greater than the relative error of the approximation when applied to the same street canyon but with all the facets having the emissivity of the surface with the highest emissivity.

2.4.4 Shortwave radiation

The method of Sparrow and Cess (1970) assumes the flux densities on each surface are uniform. Hence this method is not applicable to the direct component of the solar radiation because the direct component experiences shadowing and therefore the flux densities on each facet are not uniform. Instead, standard solar geometry schemes (e.g. Owczarek, 1997) and a shadowing scheme (e.g. Swaid, 1993; Sakakibara, 1996) can be used to calculate the facet-averaged direct solar radiative flux densities as described in Appendix A. When such geometric effects are considered, the flux densities depend on time, location and canyon orientation, and so do the relative errors in neglecting reflections (Verseghy and Munro, 1989a). The Sparrow and Cess method can be applied however to the diffuse component of the incoming shortwave radiation and to any diffusely reflected solar radiation. A similar method to that illustrated here has been used successfully to predict the time variation of the effective albedo of an urban street canyon (Pawlak and Fortuniak, 2003).

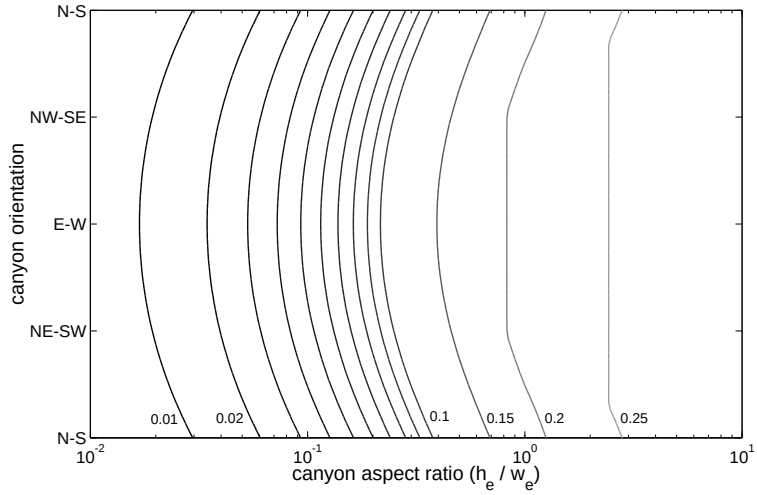

Figure 2.10: Relative error of the weighted average of solar radiative flux density using the $\mathcal{R}^0$ approximation - contours at every 0.01 (dark) until 0.1 then every 0.05.

As an example of the effects of neglecting multiple reflections of solar radiation consider the relative errors of the $\mathcal{R}_0$ and $\mathcal{R}_1$ approximations as the canyon orientation is varied for a specific case, as shown in Figures 2.10 and 2.11. The direct component of the solar radiative flux density is calculated as in Appendix A. The Sparrow and Cess method is applied to calculate the effects of multiple reflections of solar radiation. In this case the 'emitted' flux densities from the canyon facets are the reflected portion of the facet-averaged direct radiative flux density, the emitted flux from the 'sky' facet is the usual diffuse solar radiation. The case considered is midday on the spring equinox at 60°N for a canyon of aspect ratio $h_e/w_e = 1.0$ with a surface material albedo of $\alpha = 0.3$.

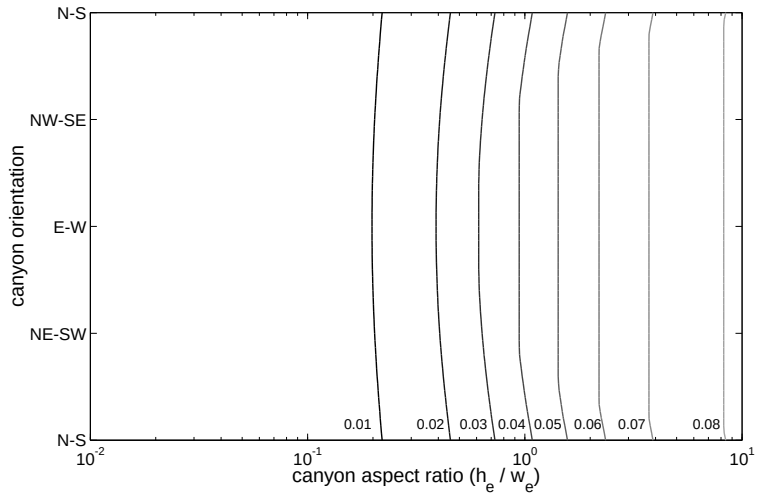

Figure 2.11: Relative error of the weighted average of solar radiative flux density using the $\mathcal{R}^1$ approximation - contours at every 0.01 (dark) until 0.08.

With both methods the relative error is dependent on the orientation of the canyon. Both approximate methods perform worse for east-west orientated canyons than for north-south orientated canyons. This is due to the asymmetry of the direct forcing on the two walls present at this time. Comparing the two figures shows that most of the inaccuracy is due to the first reflection of radiation. The error due to variation of the canyon orientation remains a second order effect with the canyon aspect ratio and surface material albedo being the dominant parameters controlling the accuracy of the two approximate methods.

The same conclusions on the validity of the different approximations remains, with the conditions on the material emissivity, ε being replaced by equivalent conditions on the material albedo, α. The increased magnitude of the solar radiation (of typical magnitude 0 to 1000 W m^{-2}), compared to the net longwave radiation (of typical magnitude -200 to -50 W m^{-2}), would suggest that a more accurate solution is required for the solar radiation and therefore the exact solution is needed. Most natural materials have emissivities that are close to one but albedos have a much greater natural range, for instance 0.2–0.4 for brick or 0.05–0.5 for glass (Oke, 1987). Reflections are therefore more likely to be important for the solar component of the radiation balance particularly as the canyon aspect ratio increases.

For example, consider a north-south orientated brick canyon ($\varepsilon = 0.9$, $\alpha = 0.3$) of aspect ratio 1.0 at 50°N on the spring equinox. The relative error in the total solar component of the zero reflections approximation is found to be 18%, that of the one reflection approximation 2.5%. This compares with the relative errors of the longwave radiation component, namely 30% for the zero reflections approximation and 3% for the one reflection approximation. However, the absolute errors for the solar component can be larger than those of the longwave component given a reasonable solar forcing. Reflections are therefore more likely to become important for the solar component of the radiation balance in an absolute sense even though the relative error may be smaller due to the direct component of the solar radiation.

The urban street canyon absorbs more solar radiation, lowering the effective albedo of the system as a whole, but the increase in surface area means that the average flux density onto the three canyon facets is smaller than that of a horizontal surface of the same material.

2.5 Summary and conclusions

The radiative exchange in an urban canyon has been investigated assuming that the radiative flux densities are uniform along each of the facets and that radiation is emitted and reflected diffusely. A method of calculating the exact solution to the net balance for the different facets of the urban canyon has been implemented and compared to two commonly used approximations. In practice this method requires the calculation and inversion of the matrix Γ for each canyon aspect ratio and material property considered. The coefficients in this matrix are then fixed; hence this method is simple to execute numerically. The exact solution varies significantly from the two approximations considered, and is therefore needed for accuracy, if the albedo of the surface material is greater than 0.2 or the emissivity is less than 0.8. Some building materials have emissivities or albedos which would imply the need to use the exact solution, e.g. concrete $\varepsilon \approx 0.7$–0.9 and brick $\alpha \approx 0.2$–0.4. The need for the more complicated approach becomes more critical as the canyon aspect ratio increases. Errors from the approximate methods can be large (an order of magnitude) and vary rapidly across the range of emissivities and albedos commonly encountered from building materials. Uncertainty in the material properties can then have an unphysically large impact on the accuracy of the net radiative flux density calculated when these approximations are used. This method has been validated against field measurements of the solar radiation over a scaled model of an urban street canyon (Pawlak and Fortuniak, 2003).

The exact solution is taken from a generic method and so can be generalised to alternative building configurations. For different geometries the shape factors between each pair of surfaces need to be calculated. The effect of multiple reflections is then achieved by inverting matrix equations analogous to Equations (2.12) and (2.13). Similar adaptation of the other two methods to other building configurations would make them comparable in complexity and hence the increased accuracy gained would favour using the exact solution.

The radiation balance in an urban setting is highly complex. Multiple reflections are shown here to play an important role; Verseghy and Munro (1989 a,b,) show, for a particular case, that the errors associated with the neglect of absorption, emission and scattering of radiation by the air in the canyon volume can be of a similar magnitude to that of neglecting multiple reflections. Given the large errors identified here when neglecting multiple reflections, it seems likely that both effects need to be incorporated into the radiation component of any surface energy balance model of an urban area. Urban energy balance models based on the urban street canyon need to consider

at least one reflection of radiation and multiple reflections are desirable for full applicability.

The surface morphology has two principal effects on the radiation balance of an urban area. Firstly, the increase in surface area acts to decrease the average radiative flux densities which would reduce the temperature variation at the surface. The reduction in temperature variation observed may not be as large as expected given the change in the average flux densities due to the asymmetry of the solar forcing resulting from shadowing. Secondly, surface geometry allows the radiation balances of different surfaces to interact. For instance, reflected radiation can form a large part of the incoming radiative flux density of a surface. This effect means that the urban surface as a whole absorbs from and emits more radiation to the overlying atmosphere than a flat surface of equivalent material properties. This is despite the reduction in the flux densities at the surface. It is this balance between the increase in surface area and effects of surface geometry which must be preserved when incorporating urban areas into numerical weather prediction models.

CHAPTER THREE

Turbulent exchange in an urban street canyon

3.1 Introduction

The turbulent fluxes of heat, moisture and momentum play a key role in determining the energy balance of any surface, and therefore in determining the surface temperature and the vertical profiles of the wind and temperature in the boundary layer. The building configuration of urban areas is known to affect the radiative component of the energy balance (Arnfield, 2003) and the turbulent flux of momentum (Raupach *et al.*, 1980; Grimmond and Oke, 1999b). The sensible heat flux from an urban area varies more spatially than the net radiative flux does over an urban area (Schmid *et al.*, 1991) and depends on the surface type and usage (Grimmond and Oke, 2002; Christen *et al.*, 2003). How this variation relates to differences in the building configuration remains unknown. This knowledge is needed for studies of the near-surface urban air quality and the formulation of the sensible and latent heat fluxes in surface energy balance models of urban areas.

The sensible heat flux is a key term in the surface energy balance. Both the surface and boundary layer temperature is determined, in part, by the sensible heat flux. In particular, the evolution and depth of the boundary layer is intimately linked to the sensible heat flux and its relation to the latent heat flux (Raupach, 2001). The potential for feedback between the surface energy balance and the boundary layer (e.g. Brubaker and Entekhabi, 1995, 1996) implies that accuracy is needed when calculating this term of the urban energy balance within numerical weather prediction models.

There are a range of existing models for the turbulent fluxes from urban areas, primarily as part of models of the surface energy balance. Grimmond *et al.* (1991) and Grimmond and Oke (1999a) present an urban surface energy balance model in which the flux of energy into the building fabric and then the turbulent fluxes are related to the evolution of the net radiation. Any influence of

the surface morphology on the turbulent fluxes is dealt with empirically by training the model with observations to each location. Best (1998b, 1999) takes a similar approach by modifying the ground heat flux and allowing the turbulent fluxes to adjust accordingly. What these approaches lack is treatment of how urban morphology affects the physical processes governing the turbulent fluxes.

Many models of the atmospheric processes in an urban area are based on a generic unit of an urban area. One such generic unit is the urban street canyon (Nunez and Oke, 1977). This generic unit is used as the basis of many energy balance models for urban areas (Johnson *et al.*, 1991; Mills, 1993; Sakakibara, 1996; Arnfield and Grimmond, 1998; Masson, 2000; Kusaka *et al.*, 2001; Martilli *et al.*, 2002). Urban street canyon models parameterise the turbulent exchange of heat from the canyon facets to the air above the canyon. The parameterisation is commonly empirical (Kusaka *et al.*, 2001) or based on the turbulent transfer from a horizontal but rough surface (Masson *et al.*, 2002). Most models formulate the fluxes in terms of the wind speed within the street canyon. A range of methods are employed to parameterise this wind speed. These include invoking results from the studies of the flow through vegetation canopies (Masson, 2000), invoking continuity (Mills, 1993) and determining the vertical profile of the wind through the accumulated effects of drag from a series of street canyons (Martilli *et al.*, 2002). In all cases, the parameterisation of the turbulent flux from the individual facets and the flux from the entire canyon unit need to be validated.

The flow (Oke, 1988; Baik *et al.*, 2000) and turbulence (Johnson and Hunter, 1995) within an urban street canyon varies with canyon geometry. The turbulent flux of a scalar from the facets of an urban street canyon is therefore expected to be influenced by canyon geometry. Barlow and Belcher (2002) develop a wind tunnel method for measuring the facet-averaged flux of a passive scalar in a neutral atmosphere from the street facet of a single urban street canyon. Barlow *et al.* (2004) used this method to measure the facet-averaged flux from each of the facets of a series of urban street canyons. Narita (2003) measured the flux of a scalar from the facets of a range of urban canonical geometries using a similar method to Barlow and Belcher (2002). All of these measurements showed a dependence of the fluxes on canyon geometry including a non-monotonic variation of the flux from the street facet as the canyon aspect ratio is increased. The purpose of this chapter is to develop a quantitative model for the turbulent flux of a scalar from an urban street canyon that explains the dependence of the fluxes on the geometry of the street canyon that was observed by Barlow *et al.* (2004).

This chapter therefore focusses on the geometric dependence of turbulent exchange from an urban street canyon and the physical processes responsible for this dependence. The urban area is represented by a series of urban street canyons oriented normally to the wind. Consideration is focussed on the case of forced convection. A model for the facet-averaged fluxes from each facet of an urban street canyon in neutral conditions is presented for a range of canyon geometries. The model is developed from ideas on the turbulent transfer across developing boundary layers (Section 3.2) and ideas on the geometric dependence of the flow within and above the street canyon (Sections 3.4 and 3.5). A comparison between the model predictions and wind tunnel measurements of Barlow *et al.* (2004) then allows an assessment of which physical processes determine the geometric dependence of the turbulent flux of a scalar from an urban surface.

3.2 The bulk aerodynamic formulation for surface fluxes

The time- and spatially- averaged flux density of a scalar property X in the inertial sub-layer, F_X, is given by

$$F_X = \langle \overline{w'X'} \rangle, \tag{3.1}$$

where the primes indicate the instantaneous departure from the mean value of X, the over-bar denotes a time average and the angle brackets a spatial average. If the flux of X is mediated entirely by turbulence, dimensional analysis shows that the flux is proportional to the difference of the mean values X takes at the surface and at some height above that surface multiplied by a transport velocity. This approach of relating the flux of X to the mean values of X is the bulk aerodynamic formulation (Garratt, 1992). Denoting the area-averaged value of X at the surface by $\langle \bar{X}_s \rangle$ and at any height, z, in the inertial sub-layer, $\langle \bar{X} \rangle$, the flux density of X at the surface, F_X, is then given by

$$F_X = w_X \left(\langle \bar{X}_s \rangle - \langle \bar{X} \rangle \right) = \frac{\langle \bar{X}_s \rangle - \langle \bar{X} \rangle}{r_X}, \tag{3.2}$$

where w_X is the transfer velocity for property X and its reciprocal, r_X, is the resistance to transport.

For a neutrally stratified rough-wall boundary layer with zero displacement height that is in equilibrium with the underlying surface, the mean vertical wind profile, $\langle \bar{u}(z) \rangle$, and mean vertical

profile of X, $\langle \bar{X}(z) \rangle$, vary as

$$\langle \bar{u}(z) \rangle = \frac{u_*}{\kappa} \ln\left(\frac{z}{z_{0m}}\right), \tag{3.3}$$

$$\langle \bar{X}(z) \rangle - \langle \bar{X}_s \rangle = \frac{X_*}{\kappa} \ln\left(\frac{z}{z_{0X}}\right), \tag{3.4}$$

where $u_* = (\tau/\rho)^{1/2}$ is the friction velocity, $X_* = -F_X/u_*$ is a scaling for X', κ is the von Kármán constant and z_{0m} and z_{0X} are the roughness lengths for momentum and property X respectively. The resistance to the transport of X therefore takes the form

$$r_X(z) = \ln\left(\frac{z}{z_{0m}}\right) \ln\left(\frac{z}{z_{0X}}\right) \Big/ \kappa^2 \langle \bar{u}(z) \rangle. \tag{3.5}$$

Within the inertial sub-layer of the atmospheric boundary layer the area-averaged flux density is uniform with height and therefore takes the same value as at the surface. Using Equation (3.5) at two heights, $z_1 < z_2$, within the inertial sub-layer, the flux density of X at the surface can be related to the mean vertical profile of X by

$$F_X = w_{X\Delta} \left(\langle \bar{X}(z_1) \rangle - \langle \bar{X}(z_2) \rangle \right) = \frac{\langle \bar{X}(z_1) \rangle - \langle \bar{X}(z_2) \rangle}{r_X(z_2) - r_X(z_1)}. \tag{3.6}$$

Using Equations (3.3), (3.4) and (3.6) the resistance to transport between the two atmospheric levels, $r_{X\Delta} = r_X(z_2) - r_X(z_1)$, can be expressed as

$$r_{X\Delta} = \frac{\Delta \langle \bar{X} \rangle}{u_* X_*}. \tag{3.7}$$

In a boundary layer where the mean vertical profiles of all properties can be described by Equation (3.4), as determined by the relevant roughness lengths, $r_{X\Delta}$ takes the same value regardless of the property considered.

A boundary layer undergoing an adjustment to new surface properties forms an internal boundary layer. The profile of X in such a region can be considered to form three sub-layers. The

inner-most layer is in full equilibrium with the underlying surface, the outer-most layer remains unaffected by the change in surface properties with the middle layer blending the two profiles together. The depth of the internal boundary and inner layers relate to the distance downstream from the change in surface properties; the inner layer is taken to grow linearly with distance from the surface change. The turbulent transport from the surface to a height in the outer layer depends on both the resistance to transport off the surface, r_1, and the resistance to transport across the internal boundary layer, r_{12}, as shown schematically in Figure 3.1. If the wind speed at height z_1 in the inner layer is known, r_1 is given by Equation (3.5). The resistance to transport r_{12} is given by Equation (3.7) where now u_* and X_* are the local scaling terms. These local scaling terms are approximated by those of the outer layer as transport is dominated by the larger eddies which will have this characteristic scaling.

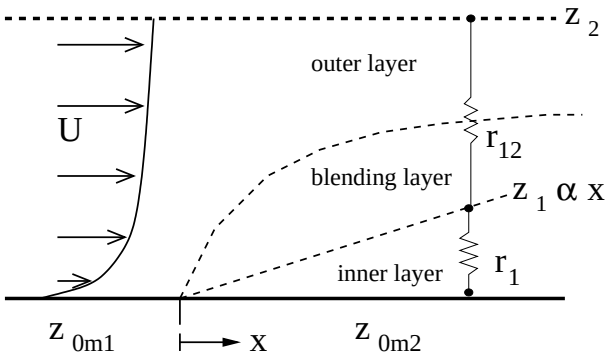

Figure 3.1: Schematic of the resistance network across a developing internal boundary layer.

In an adjusting boundary layer it is not immediately obvious that Equation (3.7) takes the same value for all properties X. In fact, assuming Equation (3.7) holds for the transport of momentum, the resistance to transport of property X depends on the ratio $r_{X\Delta}/r_{u\Delta}$ - when considering heat this ratio is the turbulent Prandtl number. For small scale turbulence and turbulence in a free shear layer the turbulent Prandtl number is approximately 1 (Tennekes and Lumley, 1997, pp. 51). It follows that the resistance to transport of heat (temperature) across a free shear layer is given by $r_{T\Delta} = \Delta u/u_*^2$, where the friction velocity is that of the outer layer.

3.3 The naphthalene sublimation technique for scalar fluxes

Quantifying the facet-averaged scalar flux from a canyon facet is complicated in three main ways. Firstly flux measurements need careful interpretation. Even modern measurement techniques can require *a priori* information which may not be known. For instance scintillometry, which can mea-

sure the sensible heat flux, requires knowledge of the displacement height of the surface (Salmond *et al.*, 2003). Secondly, the source area for the observations must be accounted for (Schmid *et al.*, 1991) and therefore isolating the flux due to one facet from the full flux is impossible. Finally, in full scale observations the boundary layer, particularly its stability, plays a role in determining the scalar flux (Dyer, 1967). Control over these conditions is impossible and knowledge of all necessary variables is rare.

Wind tunnel studies of the flow and turbulence over a rough surface provide a controlled environment to quantitatively assess the influence of surface morphology on the boundary layer. Wind tunnel studies, however, cannot be truly representative of full scale studies; for instance variation in the direction of the mean wind with height or time cannot be simulated, and care must be taken to maintain a high enough Reynolds number. The naphthalene sublimation technique is a wind-tunnel based technique to quantify the flux of a scalar from a complex surface. By using mass transfer as an analogy for scalar transfer, this technique has been used to quantify the facet-averaged flux from the different facets of an urban street canyon and the dependence of these fluxes on canyon geometry by Barlow and Belcher (2002) and Barlow *et al.* (2004). A similar method using water vapour as a tracer has been used by Narita (2003) to quantify the flux of a scalar from the facets of a range of urban geometries.

In the naphthalene sublimation technique, the scalar X in Section 3.2 is represented by naphthalene vapour. The air immediately adjacent to any surface coated with solid naphthalene saturates with naphthalene vapour at a concentration $\langle \bar{X}_s \rangle$ determined by the saturation vapour pressure for naphthalene. This layer of saturated naphthalene vapour is maintained even in high flow speed conditions. Synchronous measurements of the atmospheric pressure and surface temperature allow the calculation of the surface naphthalene vapour concentration (Barlow and Belcher, 2002; C.R.C., 1993). The background concentration of naphthalene vapour ($\langle \bar{X} \rangle$ in Equation (3.2)) can be assumed to be negligible (Barlow and Belcher, 2002). Measuring the change in mass due to loss of naphthalene, m, from a surface of area A over a period of time t allows the transfer velocity w_X to be quantified from

$$F_X = \frac{m}{tA} = w_X \langle \bar{X}_s \rangle \tag{3.8}$$

Measurements are performed over a range of wind speeds and canyon geometries to accurately

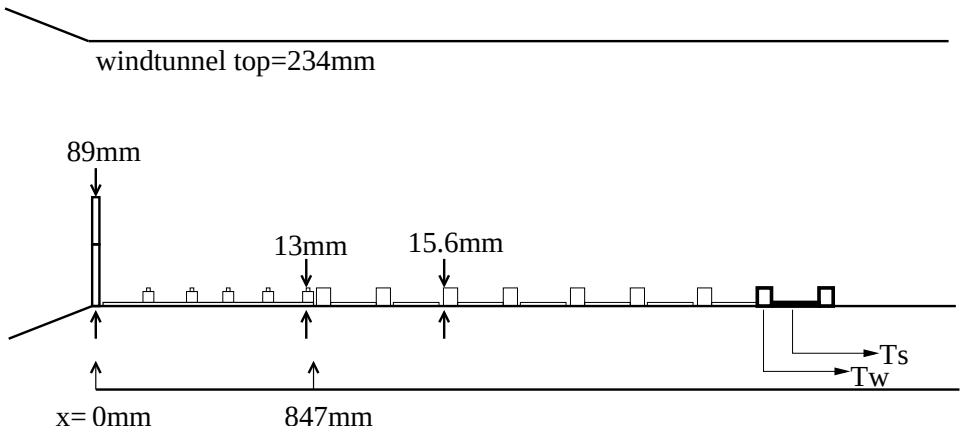

Figure 3.2: Schematic side view of the experimental arrangement used in the Barlow *et al.* (2004) experiment showing the positions of the boundary layer generating fence, Lego^{TM} upstream roughness and street canyons (after Barlow *et al.*, 2004). T_s and T_w are measurements of the street and facet temperatures respectively.

determine the transfer velocity for the flux from each facet in terms of the background wind speed and canyon geometry.

Figure 3.2 shows the experimental set-up used. The observations shown were taken from the eighth in a series of street canyons where the fluxes were observed to have adjusted to the new surface characteristics (Barlow *et al.*, 2004). The range of wind speeds used was from 4 m s^{-1} to 13 m s^{-1}. These wind speeds are sufficiently high that viscous effects do not alter the flow, turbulence or fluxes (Uehara *et al.*, 2003). Experiments were run for thirty or forty minutes, depending on the geometry, to reduce sampling error. The canyon geometry used is square bar roughness with the canyon aspect ratio varied by altering the separation of the bars. For this geometry, the planar area index, λ_p, and frontal area index, λ_f, introduced in Section 1.1 are given by $\lambda_p = \lambda_f = h_e/r_e$.

3.4 Flow patterns in an urban street canyon

The sensible heat flux from an urban area is studied here by considering the scalar flux from a two dimensional street canyon. The scalar flux from the urban street canyon is modelled here by considering the facet-averaged scalar flux from each constituent facet. This is done by constructing a network of resistances to the transport of the scalar between the constituent canyon facets and the air in the inertial sub-layer (Garratt, 1992). The flow patterns within the urban street canyon are considered now in order to develop the resistance network.

The flow within the urban street canyon can be decomposed into two regions, see Figure 3.3.

Firstly, a *recirculation region* forms in the near wake of each building. Secondly, when the street is sufficiently wide, there is a *ventilated region* downstream of the recirculation region. The different flow characteristics in these two regions mean that the fluxes from these two regions scale differently. In addition, the partitioning of the flow into the two regions depends on geometry, as shown in Figure 3.3. Hence the model for the turbulent flux of a scalar from an urban street canyon developed here is based on a parameterisation of the flows in these two regions. Figure 3.4 shows the dimensions of the two regions together with the nomenclature used.

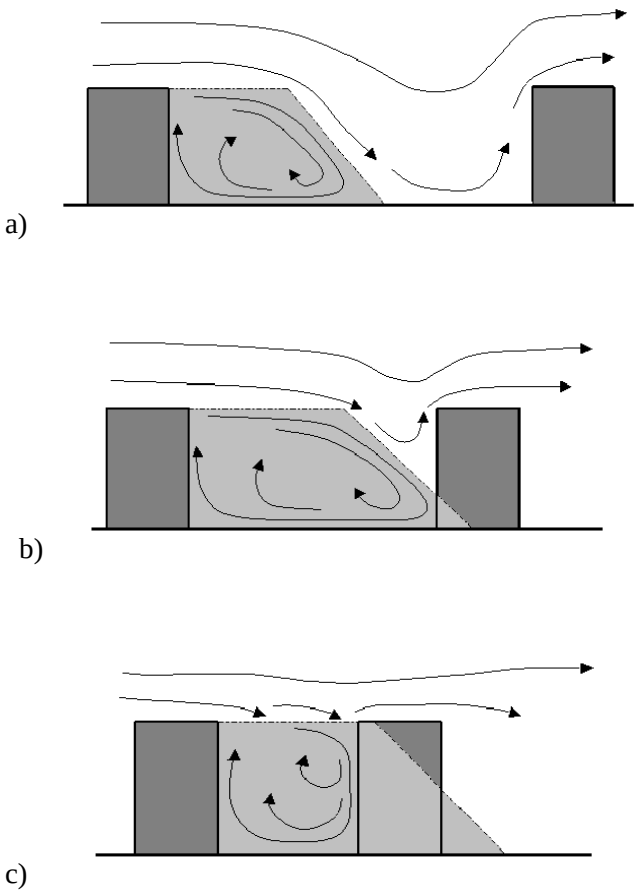

Figure 3.3: Schematic of the streamlines in the three flow regimes. (a) $L_r < w_e$ isolated roughness flow regime; (b) $L_r/2 < w_e < L_r$ wake interference flow regime; (c) $w_e < L_r/2$ skimming flow regime (flow regimes after Oke, 1987).

The recirculation region is taken here to have a trapezoidal cross section (Hertel and Berkowicz, 1989). Measurements show that the maximum length of the recirculation region across all canyon morphologies, L_r, scales on the height of the building. The value of the ratio L_r/h_e depends somewhat on the turbulence levels in the boundary layer above and the shape of the buildings and roof. Oke (1987) suggests $L_r/h_e \approx 2$–3; Castro and Robins (1977) suggest $L_r/h_e \approx 2$ for cubes;

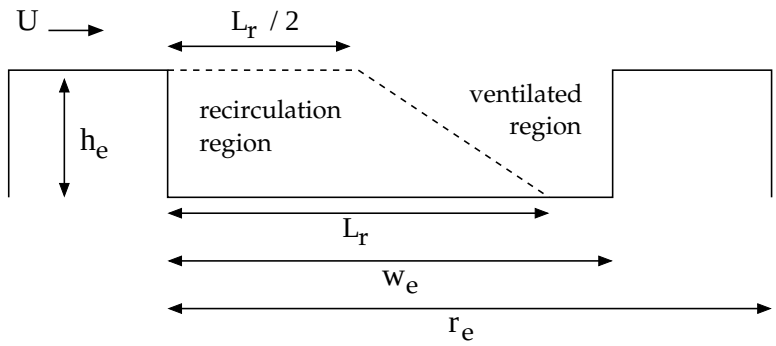

Figure 3.4: Schematic cross-section of an urban street canyon together with characteristic dimensions of the recirculation region.

Okamoto *et al.* (1993) suggest $L_r/h_e \approx 3.5$ for the two dimensional geometry considered here. Here the length of the recirculation region is taken to be $L_r = 3h_e$.

Oke (1987) describes how three flow regimes arise as the canyon aspect ratio is varied. Figure 3.3 shows schematically how the division of the street canyon flow varies with geometry and hence how the flow regimes can be related to the length scales of the two flow regions. For wide street canyons, $L_r < w_e$, so that $h_e/w_e < 1/3$, the recirculation region does not impinge on the downstream building (Figure 3.3(a)). This is the isolated flow regime of Oke (1987). For intermediate street canyons, $L_r/2 < w_e < L_r$, so that $1/3 < h_e/w_e < 2/3$, the recirculation region begins to impinge on the downstream building (Figure 3.3(b)). This is the wake interference flow regime of Oke (1987). For narrow street canyons, $w_e < L_r/2$, so that $h_e/w_e > 2/3$, the entire canyon canyon volume is occupied by the recirculation regime (Figure 3.3(c)). This is the skimming flow regime of Oke (1987).

Within the ventilated region, when it exists, high speed air from above roof level is brought down to street level. An internal boundary layer then develops along the street surface, the vertical profile of the wind adjusts to a log-layer in equilibrium with the underlying street surface.

The flow within the recirculation region is driven by the intermittent injection of a high momentum jet associated with the shear layer that is shed off the upstream roof. This jet decelerates as it progresses around the recirculation region due to the entrainment of slower moving air and due to drag of solid boundaries in a similar way to a rough-boundary wall jet (Townsend, 1976). This picture is supported by observations. Louka *et al.* (2000) show that the mean vertical velocity at the top of a narrow street canyon is negative in a narrow region next to the downstream wall. The compensating region of positive vertical velocities adjacent to the upstream wall was broader and weaker than the region of negative vertical velocities. A similar pattern of mean vertical velocities

at canyon mid-height was found by Caton *et al.* (2003) in observations of street canyon flow in a water flume. Brown *et al.* (2000) show that turbulent intensity varies monotonically across a street canyon with low values adjacent to the upstream wall and high values adjacent to the downstream walls. Finally, Barlow *et al.* (2004) showed that the facet averaged turbulent flux from the downstream wall facet of an urban canyon was, on average, a factor of 2.2 higher than that from the upstream wall facet. All features are consistent with a decelerating wall jet. The strength of the flow within the recirculation region therefore depends on the path length of the jet which in turn depends on the dimensions of the recirculation region. These arguments explain why wind speeds decrease as the jet circulates from the downstream wall across the street, and then up the upstream wall.

At high canyon aspect ratios, the jet may not reach the street surface. Numerical simulations suggest that weak counter-rotating vortices may then form in the lowest portion of the street canyon (e.g. Sini *et al.*, 1996; Baik *et al.*, 2000). Hence the wind speeds, and turbulent fluxes, deep in the canyon will be reduced in this flow regime. The effects of these complex processes on the surface fluxes are modelled here by increasing the deceleration of the jet at these high canyon aspect ratios.

3.5 Resistance network for an urban street canyon

The previous section described a partitioning of the canyon air flow into recirculating air and ventilated air. This partitioning leads to three pathways for the turbulent transport from the surface to the boundary layer above. These pathways are, firstly, from the wall and street surfaces within the recirculation region to the recirculating air and then aloft, secondly, from the wall and street surface within the ventilation region to the ventilated air and then aloft, and finally, from the roof facet to the air aloft. The ventilated air and recirculating air are each assumed to be independently well mixed and so scalar X takes a single, but different, value within each of these two air volumes (Nakamura and Oke, 1988). Figure 3.5 shows the resistance network that is used to represent transport from the facets of an urban surface to the inertial sub-layer along these three pathways.

Flux balances may now be formed for each of the pathways, as follows. Let F_i denote the flux per unit area of scalar X across the ith resistor in Figure 3.5. The flux from the upstream wall and the portion of the street that lies in the recirculation region into the recirculating air (denoted point

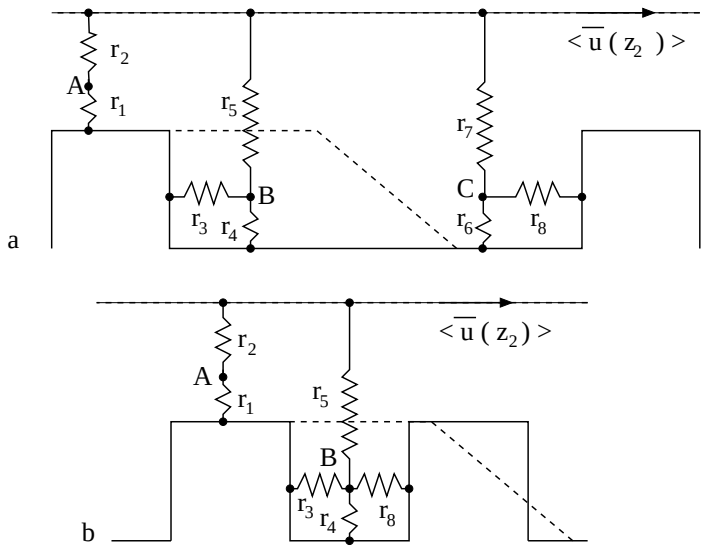

Figure 3.5: The resistance network for (a) a wide canyon, when there are distinct recirculation and ventilation regions, and (b) a narrow canyon, when there is only a recirculation region. The resistance network for the wake interference regime is the linear interpolation between these two networks.

B in Figure 3.5) equals the flux out of the recirculation region into the boundary layer aloft, i.e.

$$h_e F_3 + \min\left[L_r, w_e\right] F_4 = \min\left[\frac{L_r}{2}, w_e\right] F_5. \tag{3.9}$$

Similarly, the flux from the downwind wall and the portion of the street that lies in the ventilated region to the ventilated air (which is denoted point C in Figure 3.5) equals the flux from the ventilation region to the boundary layer aloft, i.e.

$$h_e F_8 + \left(w_e - \min\left[L_r, w_e\right]\right) F_6 = \left(w_e - \min\left[\frac{L_r}{2}, w_e\right]\right) F_7. \tag{3.10}$$

The total flux density across the top of the street canyon, F_c, which can be written in terms of a transfer velocity w_c, i.e. $F_c = w_c \Delta \bar{X}_c$, is then given by,

$$w_e w_c \Delta \bar{X}_c = \left(w_e - \min\left[\frac{L_r}{2}, w_e\right]\right) F_7 + \min\left[\frac{L_r}{2}, w_e\right] F_5. \tag{3.11}$$

Similarly the flux density from the roof, $F_r = w_r \Delta \bar{X}_r$, is given by

$$(r_e - w_e)\, w_r \Delta \bar{X}_r = (r_e - w_e)\, F_2 = (r_e - w_e) F_1. \tag{3.12}$$

Finally the total flux density from the street canyon, $F_t = w_t \Delta \bar{X}_t$, is given by

$$r_e w_t \Delta \bar{X}_t = r_e F_t = (r_e - w_e) F_2 + \min\left[\frac{L_r}{2}, w_e\right] F_5 + \left(w_e - \min\left[\frac{L_r}{2}, w_e\right]\right) F_7. \tag{3.13}$$

The use of the minima of L_r and W or $L_r/2$ and W in Equations (3.9)–(3.13) arises as the dimensions of the recirculating region cannot exceed those of the canyon cavity itself. $\Delta \bar{X}$ in Equations (3.11)–(3.13) represents the difference between the value X takes at the surface, averaged over the surface area of the individual facets concerned, and the value X takes at the atmospheric reference level, z_2. This formulation shows how the value X takes at one facet can influence the flux from the other facets by changing the value of X at the intermediate points A, B and C.

The values of the resistances in the network shown in Figure 3.5 fall into either of two generic types. The resistance to transport from each facet to the intermediate points A, B or C in the figure is determined by that across the internal boundary layers that develop along each facet. The resistance to transport between the intermediate points A, B or C and the reference height z_2 represents the resistance to transport across a free shear layer. Section 3.2 developed the formulae for the resistance to transport across an internal boundary layer (Equation (3.5)) and across a free shear layer (Equation (3.7)).

Section 3.2 formulates each of the resistances to transport in terms of the local wind speeds. Therefore all that remains is the specification of wind speeds to parameterise each of the fluxes F_i in Equations (3.9)–(3.13). Figure 3.6 shows the location and nomenclature used for these representative winds. The geometric dependence of the forcing wind speed $\langle \bar{u}(z_2) \rangle$ and these representative wind speeds is considered next.

3.5.1 Wind profile in the inertial sub-layer

The vertical profile of the wind in the inertial sub-layer of the atmospheric boundary layer is characterised by a roughness length and displacement height for the underlying urban surface,

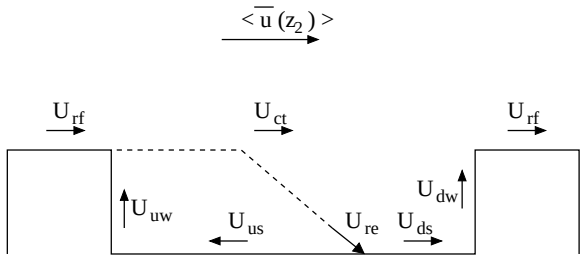

Figure 3.6: Schematic of the representative winds and their positions.

namely

$$\langle \bar{u}(z) \rangle = \frac{u_*}{\kappa} \ln \left(\frac{z - d_T}{z_{0T}} \right), \tag{3.14}$$

where κ is the von Kármán constant taking a value of 0.4 and $u_* = (\tau/\rho)^{1/2}$ is the friction velocity. The dependence of the flow in the inertial sub-layer on the characteristics of the urban area can be represented by a *bulk* or *effective roughness length*, z_{0T}, and *effective displacement height*, d_T (Grimmond and Oke, 1999a). Macdonald *et al.* (1998) calculate the vertically integrated drag on an array of cubes and deduce analytical forms for the roughness length and displacement height as functions of the morphological characteristics of the surface. These expressions have many of the observed features of urban roughness lengths and displacement heights (Grimmond and Oke, 1999a). These functions are used here with the morphological characteristics appropriate for two dimensional street canyons, namely

$$\frac{d_T}{h_e} = 1 - \frac{w_e}{r_e} A^{-(1-w_e/r_e)}, \tag{3.15}$$

$$\frac{z_{0T}}{h_e} = \left(1 - \frac{d_T}{h_e}\right) \exp\left\{ - \left(\frac{C_D}{\kappa^2} \left(1 - \frac{d_T}{h_e}\right) \frac{h_e}{w_e} \frac{w_e}{r_e} \right)^{-1/2} \right\}, \tag{3.16}$$

where $C_D \simeq 1.2$ is the drag coefficient relating to the mean wind at canyon top and $A \simeq 4.43$ is an empirical constant whose value depends on the building layout.

Figure 3.7 shows the effective roughness length and effective displacement height, normalized by the building height, for a series of street canyons with the buildings represented by square bars oriented normally to the wind at varying separations. Figure 3.7 also shows the wind speed at twice the building height normalized by the free-stream wind speed, U_δ, which is taken to be the externally imposed forcing of the scalar transport. To facilitate comparison between the model

and observations (Section 3.6) the free-stream wind is taken at the height of the reference wind in the wind tunnel of Barlow *et al.* (2004), i.e. $z_\delta = 9.5h_e$. Note how, as the canyon aspect ratio increases, there is a rapid drop and subsequent slow rise in the wind speed at $z_2 = 2h_e$ due to the combined effects of roughness and displacement.

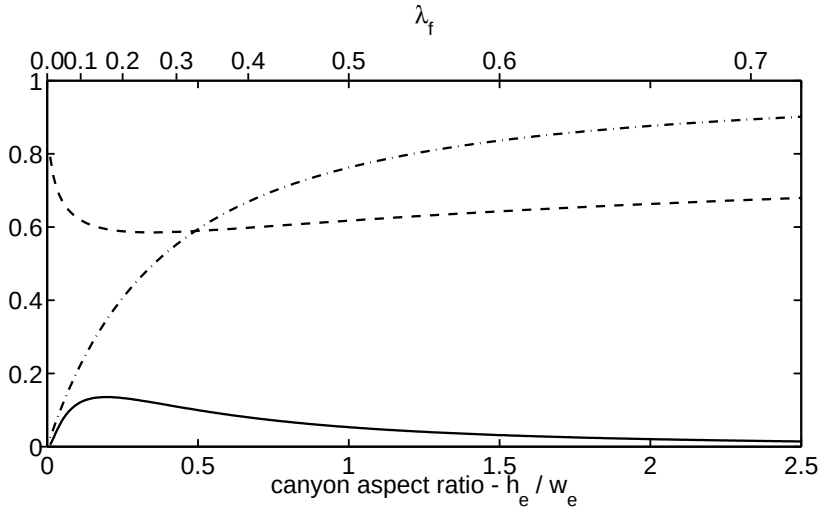

Figure 3.7: Normalized effective parameters for the vertical profile of the mean wind in the inertial sub-layer over a sequence of street canyons calculated using the method of Macdonald *et al.*, (1998). Solid line, roughness length for momentum, z_{0T}/h_e; dashed-dotted line, displacement height of flow, d_T/h_e; dashed line, wind speed at twice building height normalized by the free stream flow, $\langle\bar{u}(z_2)\rangle/U_\delta$.

Cheng and Castro (2002) observe in wind tunnel studies over an urban-type roughness that when the vertical wind profile is spatially averaged the log-layer observed in the inertial sub-layer extends right down to roof level. The wind speed at the reference level, $z_2 = 2h_e$, and wind speed at canyon top, u_{ct}, are then,

$$\langle\bar{u}(z_2)\rangle = \frac{u_*}{\kappa}\ln\left(\frac{2h_e - d_T}{z_{0T}}\right), \tag{3.17}$$

$$\frac{u_{ct}}{U_\delta} = \ln\left(\frac{h_e - d_T}{z_{0T}}\right)\Big/\ln\left(\frac{z_\delta - d_T}{z_{0T}}\right). \tag{3.18}$$

This variation of wind speed at canyon top with geometry exerts one of the strong controls on scalar transport from the surface (Section 3.6).

3.5.2 Transport from the roof

The resistance to transport from the roof, and indeed each facet, to the intermediate point A represents the resistance to transport across the internal boundary layer that develops along its length. Since the depth of the internal boundary layer grows as the length of the roof facet increases, it follows that the resistances increase with facet length. For simplicity, the depth of the internal boundary layer is taken to be 10% of the facet length.

As for the wind speed at canyon top the representative wind speed for the roof facet, u_{rf}, is obtained by extrapolating the wind profile in the inertial sub-layer down to the depth of the internal boundary layer along the roof facet, namely

$$\frac{u_{rf}}{\langle \bar{u}(z_2) \rangle} = \ln\left(\frac{h_e + \delta_{rf} - d_T}{z_{0T}}\right) \Big/ \ln\left(\frac{z_2 - d_T}{z_{0T}}\right) . \tag{3.19}$$

The resistance to transport from the roof facet to this point, A in Figure 3.5, is then given using Equation (3.5) and the resistance from A to the air aloft using Equation (3.7), which yield

$$r_1 = \ln\left(\frac{\delta_{rf}}{z_{0m}}\right) \ln\left(\frac{\delta_{rf}}{z_{0X}}\right) / \kappa^2 u_{rf}, \tag{3.20}$$

$$r_2 = \frac{\langle \bar{u}(z_2) \rangle - u_{rf}}{u_*^2}, \tag{3.21}$$

where z_{0m} and z_{0X} are the roughness lengths for momentum and X respectively for the surface material of the roof facet, and u_* is calculated from the wind profile in the inertial sub-layer. Finally δ_{rf} is the thickness of the internal boundary layer developed along the roof facet, taken as $\delta_{rf} = \min[0.1(r_e - w_e), z_2 - h_e]$.

3.5.3 Transport from the recirculation region

The measurements of Barlow *et al.* (2004) and the fluid dynamical ideas developed in Section 3.4 motivated a description of the flow in the recirculation region as that of a jet that decelerates as it travels around the canyon. Balancing advection, $u\partial u/\partial x$, and turbulent drag, $\tau \sim c_D u^2$ in the jet, yields a flow speed in the jet that decelerates exponentially with distance. There are a number of more sophisticated theoretical descriptions of the deceleration and entrainment of a jet

on a flat wall, (e.g. Townsend, 1976; Hogg *et al.*, 1997). However, the jet within the street canyon turns corners as it circulates within the canyon and so this work is not immediately applicable. Additionally, these more detailed models add further parameters to the formulation of the flow with no method of determining their value or their geometric dependence. Here, therefore, the simple exponential description is used.

First consider the wind speed of the jet when it first impinges on the street facet, u_{re}. This wind speed is then the wind speed at canyon top, u_{ct}, scaled down exponentially to account for entrainment, i.e.

$$u_{re} = u_{ct} \exp\left\{-\alpha_1 L_{se}/h_e\right\}, \tag{3.22}$$

where L_{se} is the length of the sloping edge of the recirculation region. The strongest flow and highest turbulent intensity along the canyon facets is then located at the end of the recirculation region as observed by Okamoto *et al.* (1993).

The jet then circulates along the street and wall facets in the recirculation region, and the wind speed varies as

$$u(x) = u_{re} \exp\left\{-\alpha_2 x/h_e\right\}, \tag{3.23}$$

where x is the total distance travelled by the jet from the end of the recirculation region. The two exponents α_1 and α_2 are different due to the different physical processes which they represent.

The wind speeds representative of the turbulent flux from the upstream wall, u_{uw}, from the fraction of the street facet in the recirculation region, u_{us}, and from the downstream wall if it is in the recirculation region, u_{dw}, are taken as the average of the flow $u(x)$ along each facet, namely

$$u_{\dagger} = \frac{u_{re}}{b} \int_a^{a+b} \exp\left\{-\alpha_2 x/h_e\right\} \mathrm{d}x, \tag{3.24}$$

where $\dagger$ is one of uw, us or dw, the total distance travelled by the jet to the start of the facet in question is a and b is the length of the facet. For example, when considering the transfer from the upstream wall, in the isolated roughness regime $a = L_r$ and $b = h_e$, and in the skimming flow regime $a = w_e + h_e$ and $b = h_e$.

Internal boundary layers of a fixed depth of $0.1h_e$ are then taken on each facet. The resistances to transport, r_3, r_4, r_5 and r_8 (in the skimming flow regime) are then calculated from Equations (3.5) and (3.7) as

$$r_3 = \ln\left(\frac{0.1h_e}{z_{0m}}\right)\ln\left(\frac{0.1h_e}{z_{0X}}\right)/\kappa^2 u_{uw}, \tag{3.25}$$

$$r_4 = \ln\left(\frac{0.1h_e}{z_{0m}}\right)\ln\left(\frac{0.1h_e}{z_{0X}}\right)/\kappa^2 u_{us}, \tag{3.26}$$

$$r_5 = \frac{\langle\bar{u}(z_2)\rangle - u_{us}}{u_*^2}, \tag{3.27}$$

$$r_8 = \ln\left(\frac{0.1h_e}{z_{0m}}\right)\ln\left(\frac{0.1h_e}{z_{0X}}\right)/\kappa^2 u_{dw}, \tag{3.28}$$

where u_* is the friction velocity calculated from the wind profile in the inertial sub-layer. u_{us} is used in Equation (3.27) and not u_{uw} or u_{dw} as these are representative wind speeds for the turbulent transfer in the narrow regions next to each wall whereas r_5 represents the transfer across the entire top of the recirculation region.

3.5.4 Transport from the ventilated region

Part of the jet that impinges on the street facet moves along the street facet into the ventilated region. Within the ventilated region high momentum air is transported downwards so that the jet is only decelerated somewhat. This mechanism is not available in the recirculation region which therefore has lower wind speeds. The wind speeds representative of the turbulent transport from the downstream fraction of the street, u_{ds}, and the downstream wall in the isolated roughness regime case, u_{dw}, are given as

$$u_{ds} = \frac{u_{re}}{w_e - L_r}\int_0^{w_e - L_r} \exp\left\{-\alpha_2 x/h_e\right\}\mathrm{d}x, \tag{3.29}$$

$$u_{dw} = \frac{u_{re}}{h_e}\int_{w_e - L_r}^{w_e - L_r + h_e} \exp\left\{-\alpha_2 x/h_e\right\}\mathrm{d}x. \tag{3.30}$$

As before these wind speeds are taken to be located $0.1h_e$ away from the facets.

As explained above, the mixing of high momentum air downwards in the ventilated region street places prevents the turbulent transport in the ventilated region from decreasing to the extent happening in the recirculation region. Here this process is represented by placing a minimum bound on the wind speeds computed using Equation (3.29) and (3.30). These bounds are taken from the wind profile established in an undisplaced boundary layer in equilibrium with the underlying surface when forced by the wind speed u_{ct} at a height $z = h_e$. The minimum wind speed for u_{ds} is the value taken from this profile at $z = 0.1h_e$, namely

$$\min u_{ds} = u_{ct} \ln\left(\frac{0.1h_e}{z_{0m}}\right) / \ln\left(\frac{h_e}{z_{0m}}\right). \tag{3.31}$$

Similarly, the equilibrated wind profile would then be incident on the downstream wall. The resulting turbulent transport from the wall scales as the vertical average of the wind profile. It follows that there is a minimum bound on the wind speed u_{dw} in the isolated roughness and wake interference flow regimes which is

$$\min u_{dw} = \frac{u_{ct}}{h_e - z_{0m}} \int_{z_{0m}}^{h_e} \ln\left(\frac{0.1h_e}{z_{0m}}\right) / \ln\left(\frac{h_e}{z_{0m}}\right) \mathrm{d}z. \tag{3.32}$$

The resistances to transport r_6, r_7 and r_8 (in the isolated roughness flow regime) are then given as

$$r_6 = \ln\left(\frac{0.1h_e}{z_{0m}}\right) \ln\left(\frac{0.1h_e}{z_{0X}}\right) / \kappa^2 u_{ds}, \tag{3.33}$$

$$r_7 = \frac{\langle \bar{u}(z_2) \rangle - u_{ds}}{u_*^2}, \tag{3.34}$$

$$r_8 = \ln\left(\frac{0.1z}{z_{0m}}\right) \ln\left(\frac{0.1h_e}{z_{0X}}\right) / \kappa^2 u_{dw}, \tag{3.35}$$

where u_* is the friction velocity calculated from the wind profile in the inertial sub-layer.

The resistance to transport r_8 in the wake interference flow regime is calculated by taking a weighted average of u_{dw} calculated in the two regions and then linking r_8 to both points B and C in Figure 3.5.

3.5.5 Model parameters

The model has five parameters. The surface material roughness lengths, z_{0m} and z_{0X}, are determined by the underlying surface material. Here, for simplicity, $z_{0X} = 0.1z_{0m}$ is used to represent the typical relation between the roughness lengths of momentum and heat for the facet surfaces (Garratt, 1992). The two exponents, α_1 and α_2, represent the deceleration of the jet due to the entrainment of slower moving fluid by the jet and frictional effects from the canyon facets. These exponents are found by comparison with the observations and take the values $\alpha_1 = 0.19$ and $\alpha_2 = 0.15 \times \max[1, 1.5h_e/w_e]$. The second factor in α_2 represents the increase in the deceleration of the jet due to its lack of penetration deep into the canyon cavity at high canyon aspect ratios as described in Section 3.4. α_1 is a property of the fluid; α_2 incorporates a dependence on the surface material roughness. Finally, as explained in Section 3.4, L_r/h_e is taken to be 3. The precise value of the ratio is found to have little impact on the model results provided L_r falls in the reasonable range of 2–4 building heights.

3.6 Comparison with observations

The results from the model are now compared with the wind tunnel measurements from Barlow and Belcher (2002) and Barlow *et al.* (2004). Results are shown in the form of the transfer velocity for each flux across a horizontal plane at building height (w_c or w_r) normalised by the wind speed at the top of the boundary layer, U_δ. The results are plotted against the canyon aspect ratio (bottom axis) and the frontal area index (top axis). The comparisons are made by calculating the transfer velocity from the model and comparing directly with the observations. This is done in preference to a comparison of resistances calculated from the observations as this requires prior knowledge of the model structure. The roughness length for momentum has one value for all four canyon facets determined by comparison with the observations to be $z_{0m} = 5 \times 10^{-5}$ m.

3.6.1 Flux off the roof

Figure 3.8 shows the normalized transfer velocity for the flux density from the roof facet (w_r/U_δ). The solid line is the model prediction and the symbols are observations from Barlow *et al.* (2004). For h_e/w_e greater than about 0.2, both the model and observations indicate that the flux from the roof facet varies little with canyon geometry.

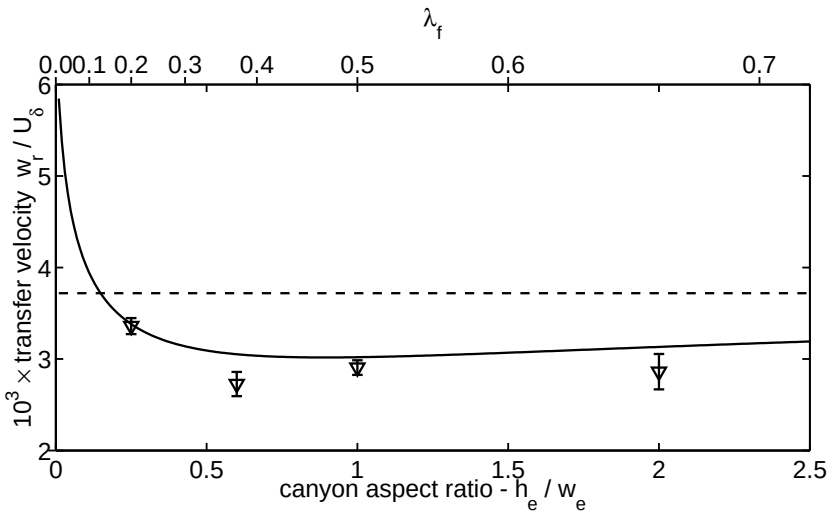

Figure 3.8: Variation of the transfer velocity for the canyon top flux density for the roof facet normalized by the free stream velocity, w_r/U_δ, with canyon aspect ratio. Solid line, model prediction; triangles, equivalent wind tunnel measurements taken from Barlow *et al.* (2004). Roughness lengths have the values $z_{0m} = 5 \times 10^{-5}$ m, $z_{0x} = 5 \times 10^{-6}$ m. Dashed line, equivalent prediction from scaled version of Masson (2000).

The model shows how the flux varies largely because of the variation of the wind speed in the inertial sub-layer with canyon geometry (see Section 3.5.1 and Figure 3.7). In the range of the observations, this variation in the wind speed is small resulting in the flat profile. At small h_e/w_e, when the building separation becomes large, the wind speed in the inertial sub-layer is increased, and the flux from the roof correspondingly increased. The transfer from the roof is higher than the transfer from a horizontal surface of the same material, w_{0t} as calculated from Equations (3.3) and (3.7) ($w_{0t}/U_\delta = 2.50 \times 10^{-3}$). At large h_e/w_e, as the buildings approach each other and the surface resembles a horizontal surface displaced to roof level, the flux from the roof facet asymptotes to that from a horizontal surface of the same material but displaced to roof level ($w_r/U_\delta = 2.93 \times 10^{-3}$). The asymptote is approached from above and is attained only for very large canyon aspect ratios ($h_e/w_e \sim 20$).

3.6.2 Flux off the street

Figure 3.9 shows the normalised transfer velocity across canyon top for the flux density from the street facet (w_c/U_δ) and its variation with canyon aspect ratio. The solid line is calculated from the model. The symbols are observations from a single street canyon (crosses, Barlow and Belcher, 2002) and a series of street canyons (squares, Barlow *et al.*, 2004). The model successfully captures several features in the observations including the dip at $h_e/w_e \simeq 0.3$, the peak at

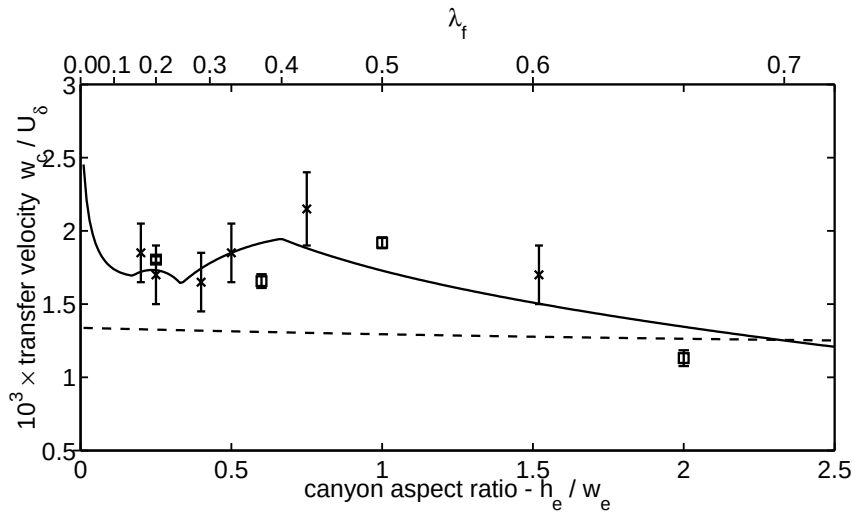

Figure 3.9: Variation of the transfer velocity for the canyon top flux density from the street facet normalized by the free stream velocity, w_c/U_δ, with canyon aspect ratio calculated from the weighted average of the flux through the recirculation and ventilated regions. Solid line, model prediction; symbols, equivalent wind tunnel measurements taken from Barlow and Belcher (2002) (crosses) and Barlow *et al.* (2004) (squares). Roughness lengths have the values $z_{om} = 5 \times 10^{-5}$ m, $z_{ox} = 5 \times 10^{-6}$ m. Dashed line, equivalent prediction from a scaled version of Masson (2000).

$h_e/w_e \simeq 0.6$ and the almost linear decrease as the canyon aspect ratio increases further. The transfer from the street is notably lower than from the roof facet (Figure 3.8) for all canyon aspect ratios.

The model of the flux from the street facet has the correct limit as the canyon aspect ratio tends to zero, namely that of a horizontal surface of the same material located at $z = 0$, which yields $w_{0t}/U_\delta = 2.50 \times 10^{-3}$. The initial decrease and subsequent general increase in w_c/U_δ as the canyon aspect ratio increases from zero to 0.6 follows the variation in the wind speed in the inertial sub-layer (shown in Figure 3.7). The flow pattern within the street canyon also influences the flux as explained in Section 3.5. The jet within the recirculation region decelerates as it progresses round the canyon cavity. The deceleration is particularly marked at high canyon aspect ratios, $h_e/w_e > 0.6$, due to the decreased penetration of the jet into the canyon cavity. This explains the reduction in w_c/U_δ when $h_e/w_e > 0.6$.

3.6.3 Flux off the walls

Figure 3.10 shows the normalised transfer velocities across a horizontal plane at canyon top for the flux from the two wall facets (w_c/U_δ). The transfer velocities are expressed in terms of the flux density across canyon top for ease of comparison with the flux from the street facet. This

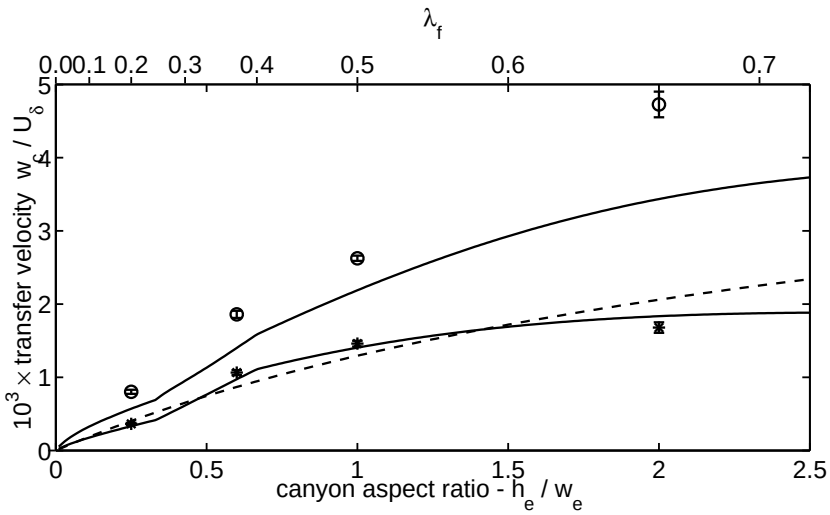

Figure 3.10: Variation of the transfer velocities for the canyon top flux density from the two wall facets normalized by the free stream velocity, w_c/U_δ, with canyon aspect ratio. Lower solid line, transfer from the upstream wall; upper solid line, transfer from the downstream wall calculated as a weighted average of the flux through the recirculation and ventilated regions; symbols, equivalent wind tunnel measurements adapted from Barlow *et al.* (2004) for the upstream wall (stars) and downstream wall (circles). Roughness lengths have the values $z_{0m} = 5 \times 10^{-5}$ m, $z_{0x} = 5 \times 10^{-6}$ m. Dashed line, equivalent prediction for both walls from a scaled version of Masson (2000).

normalisation introduces a dependence on the relative surface areas of the walls and canyon top, i.e. the ratio h_e/w_e, which leads to w_c/U_δ being approximately proportional to h_e/w_e.

The flux from the downstream wall is greater than the flux from the upstream wall by approximately a factor of two for all canyon aspect ratios. The difference between the two fluxes, taking the relative surface area into account, is increased as the canyon aspect ratio increases. These two features relate to the variation in turbulent intensity across the street canyon. The downstream wall experiences higher wind speeds and a higher turbulent intensity than the upstream wall for all canyon aspect ratios. The deceleration of the flow around the recirculation region results in reduced flow and hence reduced turbulent transport from the upstream wall. As for the flux from the street facet, this deceleration is more marked as the canyon aspect ratio increases beyond $h_e/w_e \simeq 0.6$ which increases the difference in the flux from the two walls.

3.6.4 Total flux

Figure 3.11 shows the contribution to the flux through a horizontal plane in the inertial sub-layer from each of the canyon facets, normalised by the transfer velocity from a horizontal surface of the same material located at $z = 0$, which has $w_{0t}/U_\delta = 2.50 \times 10^{-3}$. Also shown is the transfer

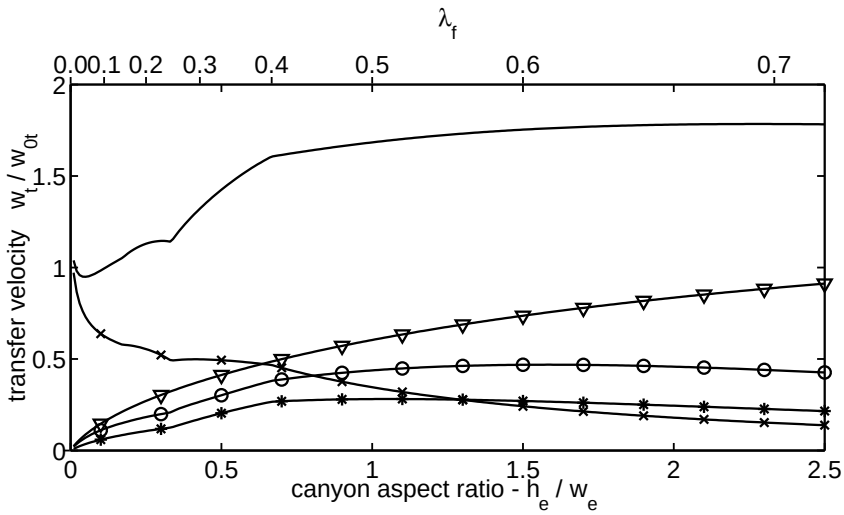

Figure 3.11: Transfer velocities from each of the facets and the whole canyon surface normalized by the transfer velocity from a flat surface of equivalent surface material properties and total planar area (w_t/w_{0t}). Circles, downstream wall; stars, upstream wall; crosses, street; triangles, roof; solid line; total transport.

velocity associated with the total flux from the canyon surface, w_t, calculated assuming that X takes the same value on all facets. Hence Figure 3.11 shows how much more efficient an urban street canyon is at releasing scalars by turbulent transport than is a flat surface.

As Equations (3.9) and (3.10) show, the flux from one canyon facet can influence the flux from another facet. This is achieved by altering the value of the scalar X in the recirculation or ventilated regions. When there is more than one source of the scalar, the transfer velocity for the total flux from the canyon, w_c, is therefore calculated through the resistance network and is not a simple addition of the single facet transfer velocities. For example, consider the skimming flow regime; the value of the scalar in the canyon cavity can be found through the resistance network as

$$w_e \frac{X_c - X_2}{r_5} = w_e \frac{X_{st} - X_c}{r_4} + h_e \frac{X_{uw} - X_c}{r_3} + h_e \frac{X_{dw} - X_c}{r_8}, \tag{3.36}$$

$$\Rightarrow X_c = \left[w_e \left(\frac{X_{st}}{r_4} + \frac{X_2}{r_5} \right) + h_e \left(\frac{X_{uw}}{r_3} + \frac{X_{dw}}{r_8} \right) \right] \Big/ \left[\frac{w_e}{r_4} + \frac{w_e}{r_5} + \frac{h_e}{r_3} + \frac{h_e}{r_8} \right]. \tag{3.37}$$

Hence, assuming that X takes the same value X_s on all facets, the transfer velocity w_c can be

found as

$$F_c = w_c \left(X_s - X_2 \right), \tag{3.38}$$

$$\Rightarrow w_c = \frac{1}{r_5} \left[w_e \frac{1}{r_4} + h_e \left(\frac{1}{r_3} + \frac{1}{r_8} \right) \right] \Big/ \left[w_e \left(\frac{1}{r_4} + \frac{1}{r_5} \right) + h_e \left(\frac{1}{r_3} + \frac{1}{r_8} \right) \right]. \tag{3.39}$$

w_t is then the average of w_c and w_r weighted by the surface area at canyon top through which each of the flux densities passes.

It is important to note that while the model performs well when compared to observations from a single-facet source of the scalar this does not guarentee similar success when considering sources from more than one facet. This is again because the fluxes can interact. Agreement then relies not only on the total resistance to transport being correct, but also the partitioning of the total resistance to transport between the individual resistances being correct. This remains a topic for future research.

Figure 3.11 shows that the flux from each individual facet is smaller than that off a horizontal surface for almost all canyon aspect ratios (the transfer from the roof asymptotes $\simeq$ 1.2). The reason is that the canyon geometry reduces the near-surface flow, turbulent intensity and hence the flux. The total flux is however greater than from a horizontal surface. This increase is due to the increased surface area, indicated by the approximately linear increase in the total flux as the canyon aspect ratio increases from zero to about $h_e/w_e = 0.75$. At high canyon aspect ratios, $h_e/w_e > 0.75$, the reduction in the near-surface flow is sufficient to reduce the increase in the total flux with total surface area.

Figures 3.8–3.10 also show values for the normalized transfer velocities calculated using the model of Masson (2000) with a building height of 10 m (dashed lines). The order of magnitude from the two models agree due to the similarity in the values common parameters take. The model presented here accounts for the additional physical processes of the variation of the wind speed in the inertial sub-layer as the geometry varies and the systematic variation in the flow field within the street canyon. Only when these processes are accounted for do the the model predictions show the variation with geometry found in the observations.

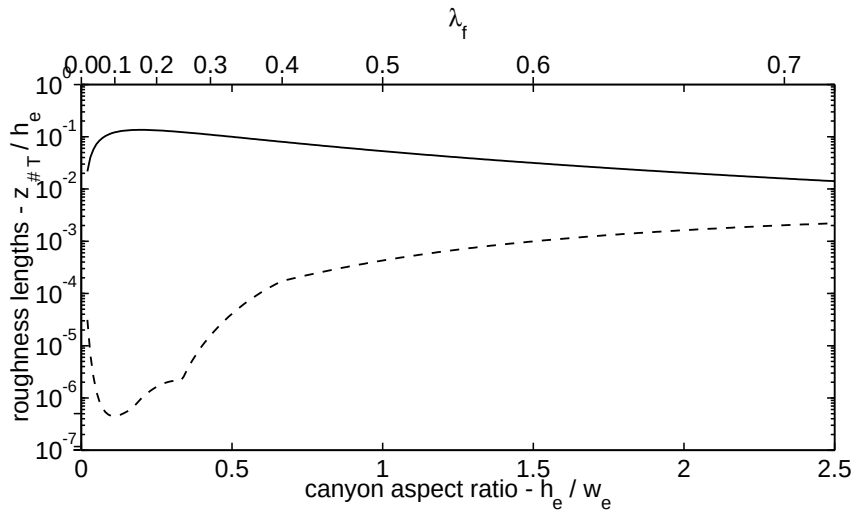

Figure 3.12: Bulk roughness lengths for momentum (solid line) (Macdonald, 1998) and scalar X (dashed line) normalised on the building height h_e for a series of square bar street canyons. Note the log-scale.

3.7 Roughness lengths for scalars

The bulk roughness length for momentum for an urban area, z_{0T}, represents the combined effects of the building array on the mean wind speed and Reynolds stresses in the inertial sub-layer. In an analogous way, the *bulk* or *effective roughness length for a scalar*, z_{XT}, would represent the combined effects of the buildings on the mean profile and flux of scalar X in the inertial sub-layer. As the flow field experiences form drag in addition to the viscous and turbulent stresses over rough surfaces, unlike the scalar field, these two roughness lengths vary differently with surface morphology (Roth, 2000). Within numerical weather prediction models, the effects of complex surfaces such as orography are commonly parameterized through the use of effective roughness lengths (e.g. Wood and Mason, 1991; Hewer and Wood, 1998). The bulk roughness length for a scalar is defined by analogy to the transfer from a flat but displaced surface (Equation (3.5), or Hewer and Wood, 1998). The value taken by z_{XT} gives the same area-averaged scalar flux for a given mean surface to air difference, namely

$$z_{XT} = (z_2 - d_T) \Big/ \exp\left\{ \frac{\kappa^2 \langle \bar{u}(z_2) \rangle}{\ln\left((z_2 - d_T)/z_{0T}\right) w_t} \right\} \tag{3.40}$$

where z_2 is the reference level in the inertial sub-layer and w_t is the transfer velocity for the total flux.

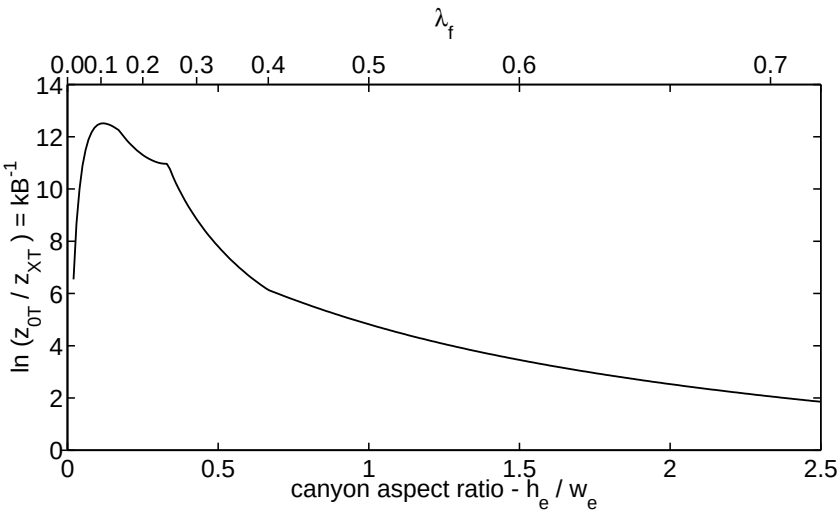

Figure 3.13: Ratio of the bulk roughness lengths for a series of urban street canyons expressed on a log scale - kB^{-1}.

Figure 3.12 shows the bulk roughness lengths for momentum and scalar transport for a series of urban street canyons as inferred from the model. At low canyon aspect ratios the bulk roughness length for momentum is greatly increased (Figure 3.7) whereas the total flux of the scalar is increased only slightly (Figure 3.11) from the flat surface values. The bulk roughness length for the scalar X is therefore greatly reduced. As the canyon aspect ratio increases the total flux remains relatively constant (Figure 3.11) and the bulk roughness length for momentum decreases due to the transition into skimming flow (Figure 3.7). The bulk roughness length for scalar transport correspondingly increases and at high canyon aspect ratios, $h_e/w_e > 2$, exceeds that for the flat surface.

The ratio of the bulk roughness lengths for momentum and heat, expressed on a log-scale $\left(\ln(z_{0T}/z_{XT}) = kB^{-1}\right)$ is used to describe the relative efficiencies of momentum and scalar transport for different surfaces. Over bare soil and vegetated surfaces this ratio takes a value of around 2 (Garratt, 1992). Verhoef *et al.* (1997) showed that over sparsely vegetated surfaces this ratio can increase up to a value of 7. Synchronous observations of the sensible heat flux and Reynolds stresses over Vancouver, Canada ($\lambda_f \approx 0.2$, Voogt and Grimmond, 2000) indicate that this ratio takes a larger value in the range of 13–27 over an urban area. Similarly, Sugawara *et al.* (2003) observed values of kB^{-1} of between 6–30 over Tokyo. These values are influenced by the time of day and the method used to determine the 'surface' temperature (Voogt and Grimmond, 2000).

Figure 3.13 shows the ratio kB^{-1} as calculated from the model for the range of surface morphologies considered. For canyon aspect ratios of less than 0.5 the model values lie within, but

at the low end, of the range of observations of Voogt and Grimmond (2000) and Sugawara *et al.* (2003). However, for higher canyon aspect ratios kB^{-1} falls below outside the range of the observations. There is currently insufficient observational data across the range of urban surface morphologies to determine whether the model prediction is correct. However, there are two reasons why the reduction in kB^{-1} for high canyon aspect ratios may not apply to real urban areas. Firstly, the bulk roughness length for real urban areas is unlikely to decrease as much as Macdonald *et al.* (1998) predict due to variability in the building height and the variety of roof shapes (Macdonald, pers. commun.). Accounting for this would increase the ratio kB^{-1} particularly for the higher canyon aspect ratios. Secondly, the full scale observations incorporate spatially varying surface values of the scalar and stability effects on the turbulent transport. Little is known about how either process impacts on the scalar flux or on how these processes are influenced by surface morphology. This issue is one example of doubts over the applicability of applying results from wind tunnel studies, under neutral conditions within generic units of the urban surface, to real urban areas.

3.8 Sensitivity to surface morphology

Urban area comprise building morphologies other than street canyons comprised of square bar buildings. Figures 3.14 and 3.15 show the sensitivity of the model to varying h_e/w_e and w_e/r_e separately with the other parameter held constant. In both cases the transfer velocities across a plane at canyon top, normalised by the flat surface value, reflect the same processes as Figure 3.11. In each case the total flux remains above the value of a flat surface due to the increase in total surface area. In all cases except for the flux from the roof in the case of wide roofs and narrow street canyons (left hand side of Figure 3.15), the fluxes from the individual facets are less than that of a flat surface. The exception highlighted above results from the form of the bulk roughness length and displacement height which for the particular geometries concerned gives a displaced but unroughened flow and therefore increased transport. This illustrates again the balance between the reduction in the near surface flow, and hence reduced flux densities, and the increase in the total surface area, which increases the total flux.

A noticeable feature is that the observed features of the turbulent transport from the street, namely the dip and peak in the transport, are not found when varying the canyon aspect ratio on its own. This implies that w_e/r_e is a key parameter when determining the turbulent fluxes from an

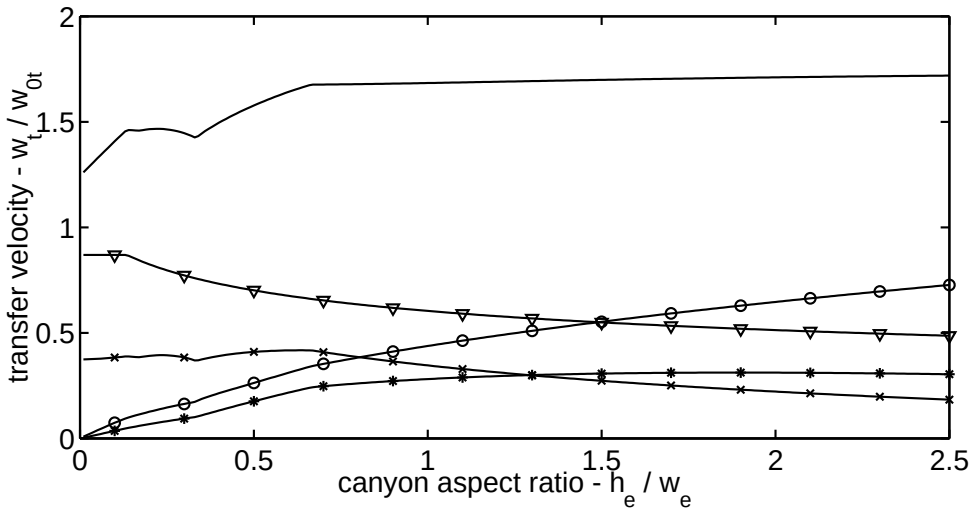

Figure 3.14: Transfer velocities from each of the facets and the whole canyon surface normalized by the transfer velocity from a flat surface of equivalent surface material properties and total planar area (w_t/w_{0t}) while varying the canyon aspect ratio with $w_e/r_e = 0.5$. Circles, downstream wall; stars, upstream wall; crosses, street; triangles, roof; solid line; total transport.

urban area and attention should be paid in determining a representative value for this parameter as well as for the canyon aspect ratio in real cities.

3.9 Summary and conclusions

Barlow and Belcher (2002) and Barlow *et al.* (2004) showed that the flux of a passive scalar from an urban street canyon under transverse flow depends on the geometry of the canyon. The variation with canyon geometry is as much as 50% and importantly differs for each facet of the canyon. This variation is sufficient to warrant inclusion in models of the urban surface energy balance.

The model developed here is based on a partitioning of the canyon air into two distinct regions namely a recirculation region and a ventilated region. The partitioning ensures the correct limit for the transfer velocities as the canyon aspect ratio becomes very small or very large. The individual facets of the canyon flux different amounts implying the need for different representative wind speeds. A single canyon wind speed is unable to reproduce the geometric dependence of all of the facets.

It is shown that there are two principal effects of urban morphology on the flux of a passive scalar from the surface. Firstly, canyon geometry acts to reduce the flow in the inertial sub-layer and hence the wind speeds within the vicinity of the street canyon. This reduction in the wind speed reduces the flux densities from the canyon facets. Secondly, the total surface area of a street

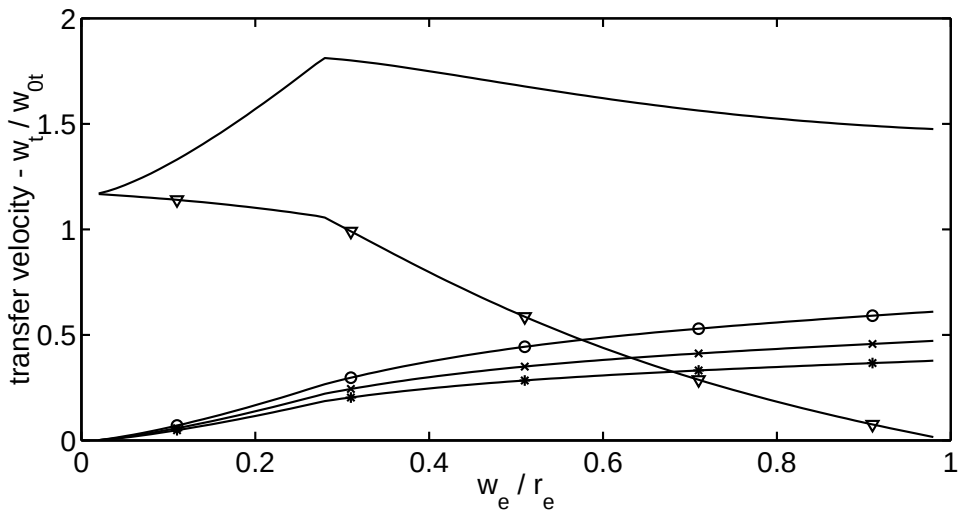

Figure 3.15: Transfer velocities from each of the facets and the whole canyon surface normalized by the transfer velocity from a flat surface of equivalent surface material properties and total planar area (w_t/w_{0t}) while varying w_e/r_e with the canyon aspect ratio held constant at 1.0. Circles, downstream wall; stars, upstream wall; crosses, street; triangles, roof; solid line; total transport.

canyon is increased compared to a flat surface which acts to increase the total flux from the surface. These two processes occur regardless of the specific morphology used to represent the urban area.

The model also accounts for streets and buildings made from different materials through the roughness lengths of the underlying surface material. The transfer velocities from the model depend on the ratios z_{0m}/h_e and z_{0X}/h_e. Increasing either roughness length increases the turbulent transport and increases the magnitude of the peak in the transfer from the street facet. The roughness of one facet can also influence the transfer from the other facets. Increasing the roughness length for momentum of the street facet by a factor of ten to simulate the presence of trees, for instance, increases the transfer from the two walls by 0–5%.

The urban street canyon is only one generic unit of an urban area. Other generic units will have differing low level flow and turbulence fields. The model presented can be extended to other generic arrays of buildings provided the wind speeds representative of the turbulent transfer are adapted to include the appropriate physical processes occurring such as corner vortices or flow separation due to peaked roofs. Such a generalisation remains a task for future work. The sensitivity of the model to urban canyon geometry indicated that the full morphology of the urban area is important in determining the turbulent flux of a scalar from an urban area. Different morphological dependencies arise as the building morphology is varied in different ways with the balance between the reduced near surface flow and increase in total surface area determining the total flux.

The sensible heat flux is a key term in the surface energy balance. The present work shows how the flux of a scalar, such as sensible heat, varies with surface geometry, albeit in neutral conditions. It is suggested that a model for the urban energy balance that is valid over the full range of urban areas will need to account for this variation.

CHAPTER FOUR

Energy balance and boundary layer interactions

Urban areas impose a range of effects on the energy balance and the boundary layer potential temperature profile. The previous chapters considered the effects of surface morphology on the individual terms of the energy balance. The extent to which the observed impacts of urban areas on the local climate can be attributed to the combined effects of surface morphology on the surface energy balance is not accurately known.

The most commonly studied feature of the urban climate is the nocturnal urban canopy heat island (e.g. Oke, 1982; Arnfield, 2003). Like many features of the urban climate this commonly has a distinct spatial pattern with a distinct edge and a core region of high thermal anomalies (e.g. Oke, 1987). While in practice the magnitude of the urban canopy heat island cannot always be correlated accurately with the local surface morphology (Bärring *et al.*, 1985), it is likely that surface morphology does play a role in its evolution.

The surface energy balance of urban areas varies with synoptic conditions, time and position. There are however, many common differences between the energy balance of an urban area and the energy balance of the surrounding rural areas. The ground heat flux is commonly increased, the latent heat flux nearly always decreased and the phase of sensible heat flux is often delayed particularly in the transition to negative values in the early evening (e.g. Cleugh and Oke, 1986; Grimmond and Oke, 1995; Oke *et al.*, 1999). Urban areas can also maintain positive sensible heat fluxes throughout the night even in synoptic conditions where stable boundary layers would otherwise be formed (e.g. Oke *et al.*, 1999). Given the range of the physical processes influencing the urban climate and the variety of urban areas it is surprising that most urban areas show these common traits. This therefore gives support to the idea that a common feature of urban areas, such as surface morphology, may be the principal cause of them.

There are a range of urban energy balance models many of which explicitly incorporate surface morphology (e.g. Arnfield, 1982, 1990; Johnson *et al.*, 1991; Mills, 1993; Mills and Arnfield, 1993; Sakakibara, 1996; Masson, 2000; Kusaka *et al.*, 2001; Martilli *et al.*, 2002). A full investigation of the influence of the canyon aspect ratio on the rates of nocturnal cooling was considered by Johnson *et al.* (1991) and Oke *et al.* (1991), however, their study considered the idealised case of no turbulent heat exchange. The shape factor effect on the longwave radiation (Chapter 2) was shown to be the key physical process acting. Other properties such as the substrate material were found to be of secondary importance. Mills (1993) and Mills and Arnfield (1993) considered the effects of surface morphology on the energy balances of the individual facets and on the energy balance at canyon top. Surface morphology was found to influence all terms of the energy balance of the individual facets whereas little influence on the energy balance at canyon top was observed due to interactions within the canyon cavity. Masson (2000) considered the mean annual cycle of the energy balance of an urban street canyon for two canyon aspect ratios. Increasing the canyon aspect ratio tended to increase the ground heat flux at the expense of the sensible heat flux. These studies, however, considered the surface energy balance scheme when forced by the atmosphere and did not allow the possible feedbacks between the surface energy balance and boundary layer (e.g. Brubaker and Entekhabi, 1996). Martilli (2002) considered the variation in the boundary layer over an urban area as the mean building height was varied. The nocturnal urban boundary layer was deeper, the lowest levels warmer and a layer above these cooler than that of a neighbouring rural boundary layer. As the majority of the observed climatological features common to most urban areas are atmospheric phenomena, the interaction between the surface and the boundary layer must be considered when investigating these features. A detailed investigation as to which features of the urban boundary layer can be explained by surface morphology and the identification of the individual physical mechanisms resulting from the surface morphology that explains them has not been done.

This chapter therefore focusses on the influence of surface morphology on the energy balance of an urban area and on the boundary layer above. In Sections 4.1–4.3, results from Chapters 2 and 3 are used to formulate an energy balance model for an urban street canyon. This energy balance model is then coupled to the one-dimensional boundary layer model of Busch *et al.* (1976). The energy balance model developed therefore incorporates the detailed physical processes occurring at the street scale but ignores variation in the surface type on the neighbourhood scale. The urban energy balance and boundary layer are then able to interact as if the urban area were uniform

and infinitely sized and allows an investigation into the impacts of surface morphology on the equilibrated boundary layer. The idealised diurnal cycle of the energy balance and boundary layer over an urban area is compared to that from a flat surface in Section 4.5. A detailed analysis of the model results allows an investigation into which features of the urban climate can be attributed to surface morphology and the precise physical mechanisms responsible. Finally, Section 4.7 considers the sensitivity of the energy balance to surface morphology and seeks to relate this to the spatial variation of the urban modifications of the local climate.

4.1 The surface energy balance model

The evolution of the boundary layer over any surface is determined by the surface energy balance, and more strictly the vertical divergence of the bulk sensible heat flux. For complex surfaces such as urban areas, there are a range of methods to calculate the surface energy balance including spatial averaging (Grimmond and Oke, 2002) and considering representative points on (e.g. Johnson *et al.*, 1991) or averages over each part of the surface in turn (e.g. Mills, 1993; Masson, 2000; Kusaka *et al.*, 2001; Martilli *et al.*, 2002). This work uses the last of these three options. For the purposes of this work this method has two advantages. Firstly, facet-averaging is an inherent part of the experimental work to determine the turbulent flux of a scalar from an urban street canyon (Chapter 3) so results from this work can be applied directly to the energy balance model. Secondly, the impacts of a range of surface morphologies can be easily investigated using this method unlike volumetric averaging methods. The facet-averaged energy balances for the four facets of an urban street canyon are developed incorporating the effects of surface morphology on the radiative and turbulent fluxes identified in previous chapters. The *bulk energy balance* for an urban area is the combination of these four energy balances.

4.1.1 The thin-layer approximation

The energy balance for a flat surface can be written as

$$(1-\alpha)(K_{sf}+K_{df})+\varepsilon L_{\downarrow}-L_{\uparrow}-G-H-LE \;=\; 0, \tag{4.1}$$

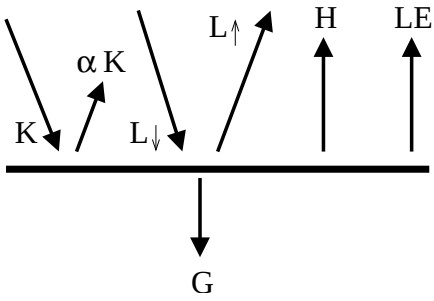

Figure 4.1: Schematic of the energy balance for a surface. The terms are introduced in the text. The direction of the arrows indicate the direction of positive flux densities.

where K_{sf} and K_{df} are the flux densities of direct and diffuse shortwave radiation respectively, $L_{\downarrow}$ and $L_{\uparrow}$ the downwelling and emitted longwave radiative flux densities respectively, and α and ε the (wavelength averaged) material albedo and emissivity respectively. G is the flux density of heat into the substrate and H and LE are the turbulent flux densities of sensible heat and energy due to the evaporation of water, respectively, from the surface into the boundary layer. Figure 4.1 shows a schematic of the surface energy balance where the direction of the arrows indicates a positive value of the flux.

Equation (4.1) arises by considering the energy balance of the surface layer of the substrate and letting the depth of this layer tend to zero. The first law of thermodynamics states that the change in internal energy of a system (in this case the layer-average temperature for the surface layer of the substrate) is determined by the difference between the heat added to the system (in this case the balance of the different fluxes) and the work done by the system (in this case zero). This version of the surface energy balance is commonly used (e.g. Smirnova *et al.*, 1997) and can be written as,

$$\Delta z\, c_s \frac{\partial T_{1/2}}{\partial t} \;=\; (1-\alpha)(K_{sf}+K_{df}) + \varepsilon L_{\downarrow} - L_{\uparrow} - G - H - LE, \tag{4.2}$$

where $T_{1/2}$ is the layer-averaged temperature of the surface layer of the substrate of thickness Δz and c_s is the volumetric heat capacity of the substrate.

Two further approximations are made to the surface energy balance at this stage. Firstly, the urban fabric is considered to be dry therefore the latent heat flux, LE, is set to zero. To allow an investigation into the effects of surface morphology alone all energy balances are therefore dry. Secondly, some terms in the energy balance depend on the skin temperature of the surface. The

skin temperature is approximated by the layer-average temperature, $T_{1/2}$, of the thin surface layer. This approximation is justified provided the surface layer is thin so that the temperature variation across the layer is small. If the surface layer is not thin enough that this approximation can be made, the gradient of temperature normal to the surface should be incorporated when calculating terms involving the skin temperature (Best, 1998b). For the results shown here the surface layer is 5 mm or thinner for which this approximation is valid (Smirnova *et al.*, 1997).

4.1.2 The substrate temperature profile

To accurately calculate the ground heat flux and hence the surface temperature, the temperature profile within the substrate is needed. The temperature profile within the substrate is governed by the heat conduction equation, namely

$$G = k\,\frac{\partial T}{\partial z}, \tag{4.3}$$

$$c_s\,\frac{\partial T}{\partial t} = \frac{\partial G}{\partial z}, \tag{4.4}$$

where k is thermal conductivity of the substrate material in WK^{-1}m^{-1}, c_s is the volumetric heat capacity of the substrate material in JK^{-1}m^{-3} and the z-axis is positive out of the substrate (i.e. $z = 0$ at the surface and decreases into the substrate). k and c_s can vary within the substrate but for the results shown here take one value each through the entire depth of the substrate.

Equations (4.3) and (4.4) require two boundary conditions as well as an initial temperature profile. The first of the boundary conditions surface energy balance, namely

$$G = (1-\alpha)(K_{sf} + K_{df}) + \varepsilon L_{\downarrow} - L_{\uparrow} - H \qquad \text{at } z = 0. \tag{4.5}$$

The second boundary condition is given by either prescribing a temperature or heat flux at the base of the calculated temperature profile i.e. prescribing either T_{in} or G_{in} in Figure 4.2. For the flat surface energy balances used to represent 'rural' conditions the second boundary condition is $G_{in} = 0$.

Equations (4.2)–(4.4) form a coupled set of equations relating the temperature profile in the substrate to the surface energy balance. These equations are solved numerically by discretizing

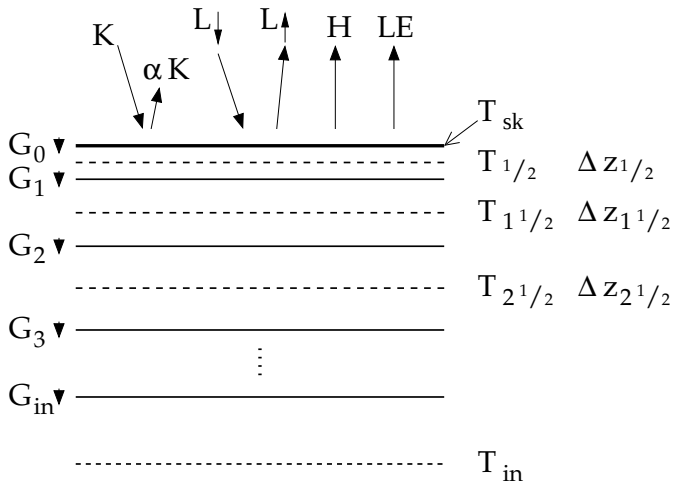

Figure 4.2: Schematic of the discretized system used to numerically solve the temperature profile within the substrate. Fluxes and layer-average temperatures are staggered in the vertical.

the substrate into a number of layers as shown in Figure (4.2) with the locations of the heat flux and layer temperatures staggered. The discretized equations are then,

$$\Delta z_{i+1/2}\, c_s \frac{\partial T_{i+1/2}}{\partial t} = G_i - G_{i+1}, \tag{4.6}$$

$$G_i = k\, \frac{T_{i-1/2} - T_{i+1/2}}{1/2(\Delta z_{i-1/2} + \Delta z_{i+1/2})}, \tag{4.7}$$

with Equation (4.5) giving a boundary condition on G_0 and a condition on T_{in} or G_{in} being the other boundary condition.

4.1.3 The radiative and turbulent fluxes

The previous section showed how the ground heat flux and surface energy balance combine to form a coupled set of equations for the temperature profile in the substrate. All that remains is the prescription of the radiative and turbulent terms in the surface energy balance.

In numerical weather prediction models the external forcing terms, i.e. the shortwave and downwelling longwave radiative fluxes, are calculated through a complex radiative transfer model and depend on the atmospheric temperature profile and aerosol loading. Appendix A describes the simple model used to calculate the direct facet-averaged shortwave flux density for a plane at an arbitrary elevation and orientation. For simplicity $L_\downarrow$ is taken as a constant.

The emitted longwave radiative flux density is calculated using a linearised form of the Stefan-

Boltzmann equation, namely

$$L_{\uparrow} \;=\; \varepsilon\sigma T_{sk}^{4} \approx \varepsilon\sigma T_{1/2}^{4} \simeq \varepsilon\sigma T_{L}^{3}(4T_{1/2} - 3T_{L}), \tag{4.8}$$

where $T_{L} = 273\text{K}$ is a background temperature.

Finally, the turbulent sensible heat flux is formulated using the bulk aerodynamic method (Garratt, 1992; Section 3.2). Using this method the turbulent sensible heat flux is related, on dimensional grounds, to the surface temperature, $T_{1/2}$, and the temperature, $\theta(z_2)$ at a reference level in the inertial sub-layer, z_2, namely

$$H \;=\; \rho\, c_p\, w_{T}\, (U(z_2))\, \big(T_{1/2} - \theta(z_2)\big)\,, \tag{4.9}$$

where ρ is the density of air, c_p the specific heat capacity of air at constant pressure, and w_{T} is the transfer velocity from the surface to the reference level. The transfer velocity is a function of the mean wind speed at the reference level, $U(z_2)$, the surface material roughness lengths for momentum and heat and the atmospheric stability (Section 3.2 and Appendix B).

4.2 The energy balance for an urban street canyon

The energy balance for an urban street canyon is developed from the facet-averaged energy balances and substrate temperature profiles for the four facets of the urban street canyon. Figure (4.3) shows a schematic of the four facet-averaged energy balances and the nomenclature used.

There are four differences between the energy balances for the urban street canyon and that of a horizontal surface. Firstly, the second boundary condition on the ground heat flux varies between a zero heat flux for the street facet (as that of the horizontal surface) and a constant temperature for the other facets. The maintenance of a constant internal temperature acts as an anthropogenic source of heat. Secondly, the transfer velocities, w_{T}, for the sensible heat flux from each facet differ and vary with canyon geometry as described in Chapter 3. Thirdly, the external radiative forcing terms vary depending on canyon geometry (Chapter 2 and Appendix A). Finally, and the key difference between the canyon facet energy balances and the energy balance of a horizontal surface is that the energy balances interact through the radiative and turbulent heat fluxes. These

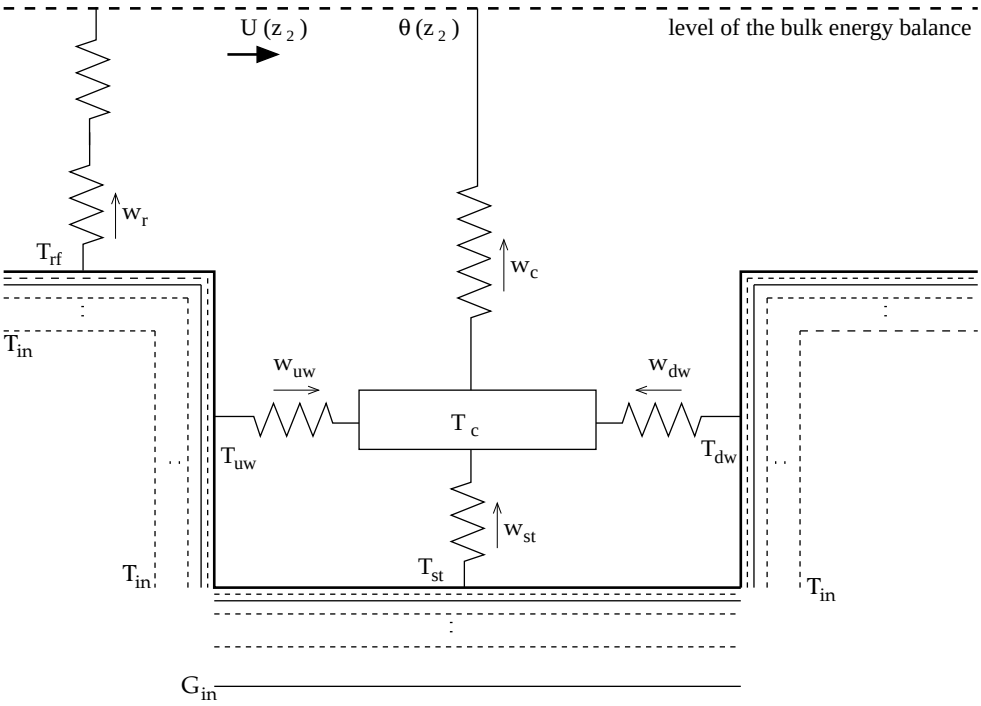

Figure 4.3: Schematic of the facet-averaged energy balances of the urban street canyon. Separate, but interacting through the surface energy balances, facet-averaged substrate temperature profiles are constructed for the roof (rf), street (st) and both the upstream (uw) and downstream (dw) walls. The interior boundary conditions for the roof and wall facets are a constant internal temperature T_{in}, that for the street facet is a zero ground heat flux $G_{in} = 0$.

interaction terms are considered in the next section.

The influence of surface morphology on the energy balance of the urban street canyon can be investigated through two sets of diagnostics. Firstly, the energy balance and surface temperatures for each of the facets can be considered. Secondly, the *bulk energy balance* and boundary layer air temperatures associated with the bulk energy balance can be considered. The bulk energy balance is the balance of energy forms across a plane at the base of the inertial sub-layer, as marked by the dashed line in Figure 4.3, and is the energy balance to which the boundary layer responds.

4.2.1 Interaction terms - Radiative fluxes

Chapter 2 described how geometry influences the exchange of diffuse radiation in an urban street canyon. The matrix method developed in Chapter 2 is used for both the long and shortwave radiative flux densities for the street and wall facets of the canyon with the common assumptions of diffuse reflections and uniform flux densities. To use the matrix method the surface material albedo or emissivity and the emitted radiative fluxes must be specified. The radiation balance for

the roof facet is that of a horizontal surface.

When applying the method to the shortwave radiative fluxes, the emitted flux densities from the canyon facets are equivalent to that fraction of the direct solar radiative flux density which is reflected. The emitted flux density for the sky facet is the diffuse radiative density. The assumptions of uniform radiative flux densities is unlikely to hold in practice but is in line with, and will be of secondary importance, to the facet-averaging of the energy balances. The matrix method is therefore applied to the shortwave radiative flux densities, using the nomenclature of Chapter 2, with

$$\Omega_i = \alpha_i K_{sf\,i}, \quad \text{for } i = st, uw, dw, \tag{4.10}$$

$$\Omega_i = K_{df\,i}, \quad \text{for } i = sk, \tag{4.11}$$

$$\text{where } \alpha_{sk} = 0.$$

When applying the method to the longwave radiative fluxes, the emitted flux densities from the canyon facets are the emitted flux densities according to the approximated Stefan-Boltzmann equation (Equation 4.8). The emitted flux density from the sky facet is the (diffuse) downwelling longwave radiative flux density. The matrix method is then applied with,

$$\Omega_i = \varepsilon_i \sigma T_L^3 \left(4T_{1/2\,i} - 3T_L\right), \quad \text{for } i = st, uw, dw, \tag{4.12}$$

$$\Omega_i = L_{\downarrow}, \quad \text{for } i = sk, \tag{4.13}$$

$$\text{where } \varepsilon_{sk} = 1,$$

and $T_{1/2\,i}$ is the layer-averaged temperature of the surface layer of each of the ith canyon facet.

The matrix method gives that the resultant net radiative flux density for each facet, Q_i, can be expressed as,

$$Q_i = \sum_i \left(\psi_{Kij}\Omega_{Kj} + \psi_{Lij}\Omega_{Lj}\right) + (1-\alpha_i)K_{sf\,i} - \Omega_{Li}, \tag{4.14}$$

where the matrices ψ are determined as in Chapter 2 and the subscripts K and L denote those terms relating to the diffuse shortwave and longwave radiation terms respectively. The energy balances

for the canyon facets are therefore coupled both in the external forcing, through reflections, and directly, through the shape factor effect on the longwave radiation.

4.2.2 Interaction terms - Turbulent fluxes

Chapter 3 described how surface morphology influences the turbulent exchange of a scalar, such as heat, from the surfaces of an urban street canyon. The model presented in Section 3.5 is used to determine the facet-averaged turbulent sensible heat flux from the individual facets with two modifications.

Firstly, the model developed in Chapter 3 considered only flow normal to the street canyon. Flow parallel to the street canyon is dealt with in an analogous way to the minimum bounds on the flow in the ventilated region of a wide street canyon. The component of the wind parallel to the canyon is extrapolated down to roof level from the reference level as per the component of the wind normal to the canyon. The flow parallel to the canyon below building height is parameterized as a log-profile determined by the surface material roughness length and the component of the wind parallel to the canyon at roof level. The flow parallel to the canyon at street level takes the value this parameterized flow takes at a height $z = 0.1h_e$. The flow parallel to the canyon along the wall facets takes the value of this parameterized flow averaged over height. The resistances to transport are calculated using the recombined total wind speeds using the formulae given in Section 3.5.

Secondly, the resistances to transport from a flat surface are influenced by the stability of the atmosphere (Dyer, 1967). This dependence will apply to the turbulent transport from an urban area as it does rural areas. To allow for this effect the resistances to transport are scaled according to the larger scale atmospheric stability. The resistance to transport from a flat surface with the equivalent bulk roughness length as that of the urban street canyon has a known dependency on atmospheric stability (Dyer, 1967; Businger *et al.*, 1971; Beljaars and Holtslag, 1991). The fractional change in this resistance to transport is calculated given the atmospheric stability (Monin-Obukhov length). Each resistance to transport, r_1–r_8, is then scaled in the same way from the neutral value given in Chapter 3. This technique is likely to simplify the effect of stability on the transport of heat from the urban street canyon as it does not account for features such as asymmetric heating of the canyon air. However, in an urban area the mechanical generation of turbulence generally exceeds that of the thermal generation/suppression of turbulence so this modification is likely to be small (Roth, 2000).

Barlow *et al.* (2004) illustrated how the turbulent flux from one facet can influence the fluxes from other facets. This effect is present in the formulation used to determine the turbulent fluxes of heat from the canyon facets. For instance, in Figure 4.3, the sensible heat flux density from the street facet in this narrow street canyon is given by (dropping the subscript $_{1/2}$ for convenience),

$$H_{st} \;=\; \rho c_p w_{st}(U(z_2))\,(T_{st} - T_c)\,. \tag{4.15}$$

T_c, the mean-temperature of the air in the canyon, is dependent on the sensible heat flux densities from each of the canyon facets and therefore the surface temperatures of those facets. Conserving turbulent fluxes in the roughness sub-layer layer (for the skimming flow case) gives,

$$T_c \;=\; \frac{w_c\theta(z_2) + w_{st}T_{st} + h_e/w_e\,(w_{uw}T_{uw} + w_{dw}T_{dw})}{w_c + w_{st} + h_e/w_e\,(w_{uw} + w_{dw})}. \tag{4.16}$$

The four facet-averaged energy balances of the urban street canyon therefore interact through the radiative and turbulent heat fluxes and must be solved as one system.

4.3 Boundary layer formulation

The energy balances developed above are coupled to a one dimensional boundary layer model (Busch *et al.*, 1976) to represent the full surface-boundary layer system. This allows the impacts of urbanisation on the boundary layer to be investigated and also allows interactions to occur between the energy balance and boundary layer (e.g. Brubaker and Entekhabi, 1996). Applying the hydrostatic approximation and Reynolds averaging to the Navier Stokes equations under horizontal homogeneous conditions gives the following prognostic equations for the mean state of the atmospheric boundary layer.

$$\frac{\partial\overline{u}}{\partial t} \;=\; -f\,(\overline{v} - v_g) - \frac{1}{\rho}\frac{\partial}{\partial z}\left(\rho\,\overline{u'w'}\right), \tag{4.17}$$

$$\frac{\partial\overline{v}}{\partial t} \;=\; f\,(\overline{u} - u_g) - \frac{1}{\rho}\frac{\partial}{\partial z}\left(\rho\,\overline{v'w'}\right), \tag{4.18}$$

$$\frac{\partial\overline{\theta}}{\partial t} \;=\; -\frac{1}{\rho}\frac{\partial}{\partial z}\left(\rho\,\overline{\theta'w'}\right), \tag{4.19}$$

where the overbar indicates the time (and spatial) average value and the prime marks the instantaneous departure from the mean value. u_g and v_g are the westerly and southerly components of the geostrophic wind respectively. The horizontal homogeneous condition is equivalent to stating that there has been sufficient fetch of homogeneous surface for a fully adjusted boundary layer to exist.

The turbulent terms are parameterised using a first order closure. The turbulence terms are related to the vertical gradients of the mean properties, namely

$$\overline{u'w'} = -K_m \frac{\partial \overline{u}}{\partial z}, \tag{4.20}$$

$$\overline{v'w'} = -K_m \frac{\partial \overline{v}}{\partial z}, \tag{4.21}$$

$$\overline{\theta'w'} = -K_h \frac{\partial \overline{\theta}}{\partial z}. \tag{4.22}$$

K_m and K_h are the turbulent diffusivities for momentum and heat respectively. The values the diffusivities take are model dependent but are related to the mean wind and temperature profiles. Appendix B gives more details of the formulation of the specific closure method used by Busch *et al.* (1976).

The surface energy balance-boundary layer coupling is achieved by carefully matching the surface values of the turbulence terms with those from the energy balance model, i.e.

$$\overline{\theta'w'}\Big|_s = H/\rho\, c_p, \tag{4.23}$$

$$-\left(\overline{u'w'}\Big|_s^2 + \overline{v'w'}\Big|_s^2\right)^{1/2} = u_*^2. \tag{4.24}$$

Equations (4.17)–(4.24) are solved by discretizing the atmosphere in the vertical and using the finite difference forms of the equations. The atmospheric lowest model level is within the inertial sub-layer and used as the representative atmospheric level in Equations (4.9), (4.15) and (4.16).

The influence of surface morphology on the surface energy balance and boundary layer is investigated in two stages. Firstly, a detailed investigation of an example case is done to illustrate the coupled nature of the system and the physical causes of thermal differences. Secondly, the sensitivity to canyon geometry is considered. Together this allows an investigation into which

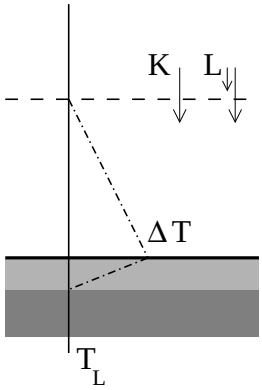

Figure 4.4: Schematic of the initial temperature profile (solid line) and the temperature profile after one time period (dash-dotted line) used in the analysis of the role of surface area in determining the impacts of surface morphology on the energy balance of an urban area.

observed features of urban areas can be explained by the influence of surface morphology on the energy balance and its spatial variation.

4.4 The role of surface area

The morphology of urban areas imposes two properties on the surface: An increased surface area and surface geometry, i.e. h_e and the ratios h_e/w_e, w_e/r_e and combinations thereof. Knowledge of how one property alone influence the terms of the energy balance is useful as it allows an assessment of the relative importance of the two properties. The probable impacts of alternative building configurations can then be estimated. Investigating the impacts of surface geometry alone is impractical. Assessing the role of surface area alone in determining the impact of surface morphology on the surface energy balance is possible however as varying the surface area is equivalent to varying the incoming radiative flux densities. To tackle this issue consider the simple analysis below.

Consider an isothermal temperature profile through the atmosphere and substrate as shown schematically in Figure 4.4; it follows that we can set $T_a = T_g = T_L$. The incidence of solar and/or downwelling longwave radiation implies that the surface temperature will change; let the change in surface temperature in one time period be denoted by ΔT. For the purposes of this analysis this change in temperature is assumed to be positive. The case of a negative change in temperature is analogous with the conclusions given then relating to the magnitude of the changes.

The approximate form for the surface energy balance is then (Bristow, 1987),

$$(1-\alpha)(K_{sf}+K_{df})+\varepsilon L_{\downarrow}-\varepsilon\sigma T_{L}^{3}(T_{L}+4\Delta T)-\rho c_{p}w_{T}\Delta T-k\Delta T/\Delta z \;=\; 0. \tag{4.25}$$

where the other symbols take their usual meaning.

Suppose that the surface area of the surface increases by a relative factor of A but the bulk external radiative forcing stays the same. Provided that the surface remains flat (physically impossible) the transfer velocity w_{T} stays the same i.e. the value taken in neutral conditions as determined by the wind speed and surface material roughness lengths. Denote the flux densities from the surface where $A=1$ by subscript $_1$, those from the surface of increased surface area by subscript $_A$. The bulk surface energy balance then becomes,

$$\begin{aligned}(1-\alpha)(K_{sf}+K_{df})+\varepsilon L_{\downarrow}-A\varepsilon\sigma T_{L}^{3}(T_{L}+4\Delta T_{A})& \\ -A\rho c_{p}w_{T}\Delta T_{A}-Ak\Delta T_{A}/\Delta z \;=\; 0,& \qquad (4.26)\\ \Rightarrow \Delta T_{A} \;=\; \frac{(1-\alpha)(K_{sf}+K_{df})+\varepsilon L_{\downarrow}-A\varepsilon\sigma T_{L}^{4}}{4A\varepsilon\sigma T_{L}^{3}+A\rho c_{p}w_{T}+Ak/\Delta z} \;=\; \frac{\varphi_0}{A}-\varphi_1,& \qquad (4.27)\end{aligned}$$

where constants φ_0 and φ_1 are positive definite. Equation (4.27) shows that increasing the surface area of the surface necessarily reduces the surface temperature variation.

The flux densities and bulk fluxes from the surface also change as the surface area is increased. The external forcing flux densities vary solely with surface area with the bulk fluxes staying the same, namely

$$K_{sf_A} \;=\; K_{sf1}\,/A, \tag{4.28}$$

$$K_{df_A} \;=\; K_{df1}\,/A, \tag{4.29}$$

$$L_{\downarrow_A} \;=\; L_{\downarrow 1}\,/A. \tag{4.30}$$

The other terms of the energy balance vary as a result of the change in surface area and the change in temperature variation. The emitted longwave radiation flux density, $L_{\uparrow_A}$, and bulk flux, $AL_{\uparrow_A}$,

vary as,

$$L_{\uparrow_A} = \varepsilon\sigma T_L^3 \left(T_L + 4\left(\varphi_0/A - \varphi_1\right)\right) < L_{\uparrow 1}, \tag{4.31}$$

$$AL_{\uparrow_A} = L_{\uparrow 1} + (A-1)\varepsilon\sigma T_L^3 \left(T_L - 4\varphi_1\right) > L_{\uparrow 1}, \tag{4.32}$$

$$\text{as } T_L - 4\varphi_1 = \frac{\rho c_p w_T T_L + kT_L/\Delta z}{4\varepsilon\sigma T_L^3 + \rho c_p w_T + k/\Delta z} > 0. \tag{4.33}$$

The flux density of the emitted longwave radiation therefore decreases as the surface area is increased but the bulk flux of longwave radiation is increased.

Conversely, the bulk fluxes and flux densities of the sensible heat and ground heat vary as,

$$H_A = \rho c_p w_T(\varphi_0/A - \varphi_1) < H_1, \tag{4.34}$$

$$AH_A = H_1 - (A-1)\rho c_p w_T \varphi_1 < H_1, \tag{4.35}$$

$$G_A = \frac{k}{\Delta z}(\varphi_0/A - \varphi_1) < G_1, \tag{4.36}$$

$$\text{and } AG_A = G_1 - (A-1)\frac{k}{\Delta z}\varphi_1 < G_1. \tag{4.37}$$

The density and bulk values of the sensible and ground heat fluxes are all decreased by increasing the surface area of the surface. The effect of increasing the surface area on the energy balance is therefore to reduce the temperature variation and to change the partitioning of energy forms at the surface with more energy going into emitted radiation and less into turbulent sensible and ground heat forms. This finding will be contrasted to the findings when considering the full effects of surface morphology in the next section.

4.5 Case study

The role of surface morphology in determining the energy balance and boundary layer profiles is now considered in relation to a specific case study. A comparison is made between the fully adjusted (i.e. one-dimensional column) boundary layer profiles and the bulk energy balances established over the urban canyon surface and over two flat dry surfaces. The ‘smooth’ surface has the same roughness length as the material roughness length of the urban fabric. The ‘roughened’

surface has the same roughness length as the bulk roughenss length of the urban canyon. Comparing the three cases isolates the effects of surface morphology on the surface and illustrates the advantages and disadvantages of modelling an urban area as a bare soil surface with an increased roughness length (e.g. Myrup, 1969).

For the specific cases considered the surfaces are located at 60°N and the day is the spring equinox. The surface material properties for the coupled systems are equal, $\alpha = 0.1$, $\varepsilon = 0.98$, $k = 0.75\text{WK}^{-1}\text{m}^{-1}$, $c_s = 1.5 \times 10^6\text{JK}^{-1}\text{m}^{-3}$, and are representative of common building materials such as brick (Oke, 1987). The urban geometry considered is an urban street canyon where $h_e/w_e = 1$, and $w_e/r_e = 0.5$, oriented north-south with a building height of 10 m. The surface material roughness length is $z_{0m} = 0.01$ m, the bulk roughness length computed for this canyon morphology is $z_{0T} = 0.53$ m (using Macdonald *et al.*, 1998).

The external forcing conditions are chosen to be representative of synoptic conditions conducive to longwave radiative cooling - light winds and clear skies. These conditions favour large urban-rural thermodynamic differences (Oke, 1987). The shortwave radiative forcing is described in Appendix A. The downwelling longwave radiative flux density is constant at $L_{\downarrow} = 240$ W m^{-2} chosen to minimise the drift in time of the total energy in the flat surface case. The geostrophic wind speed is light at $u_g = 5$ m s^{-1} and $v_g = 0$ m s^{-1}.

The models are initialised at dawn. Figure 4.5 shows the initial temperature profiles in the atmosphere (a) and substrate (b). The atmospheric potential temperature profile is comprised of four layers. From the surface upwards these are a surface inversion layer, a residual layer from the previous day's well-mixed layer, a capping inversion and finally a stable layer in the free troposphere.

The initial conditions in the substrate are an interpolation from the surface temperature to the interior temperature (293 K for the internal building temperature, 285 K for the horizontal surfaces and street facet) dependent on the surface material properties. The depth of the substrate used for the flat surfaces and the canyon facets is greater than 0.5 m, the material properties are such that the depth of penetration of the diurnal temperature signal is approximately 0.12 m (Garratt, 1992) hence the boundary conditions at the base of the substrate temperature profiles are expected to play a minor role. The constant temperature condition used for the interior of the wall and roof facets acts as an anthropogenic heat source in the case where the interior is warmer than the substrate. However, if the substrate is warmer than the interior this condition acts as a heat sink. This is

unrealistic as it implies that another source of energy must be employed to remove the energy from the wall or roof substrate which is not accounted for elsewhere. These initial conditions are representative of the substrate and atmospheric profiles established after a night conducive to radiative cooling.

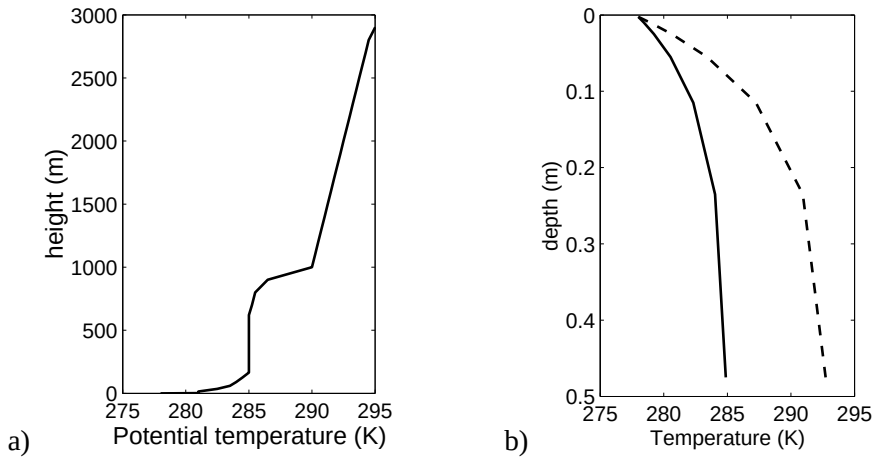

Figure 4.5: The initial conditions used in the case study. (a) Potential temperature profile in the boundary layer. (b) Temperature profiles used in the substrate; solid line, profile for the flat surfaces and the street facet; dashed line, profile for the two wall and roof facet.

The initial wind profiles are determined from the bulk roughness length, the displacement height and the geostrophic wind speed applied at the top of the boundary layer ($z_i = 1$ km), namely

$$u(z) = \begin{cases} u_g \ln\left((z - d_T)/z_{0T}\right) \Big/ \ln\left((z_i - d_T)/z_{0T}\right) & \text{for } z_2 < z < z_i, \\ u_g & \text{for } z \geqslant z_i, \end{cases} \tag{4.38}$$

and similarly for the v-component.

Results are shown for the second model day to allow for an adjustment due to unbalanced initial conditions but to minimise the drift between the different model runs. The energy balances for the three coupled systems, bulk and individual facets, are considered first with the accompanying effects on the surface and atmospheric temperatures considered later.

4.5.1 Case study: The bulk energy balances

The first three panels of Figure 4.6 show the bulk energy balances for the three coupled systems considered. In each case the black solid line is the net radiative flux density, the red dashed line is the sensible heat flux density and the green dash-dotted line is the ground heat flux density calculated as a residual.

Figure 4.6(a) shows the energy balance from the coupled energy balance-boundary layer system with the smooth horizontal surface. The additional dotted line on this plot is the ground heat flux density calculated from the top two substrate layers. The close match between the calculated ground heat flux densities and the theoretically expected reduction in magnitude and phase delay between the two (Garratt, 1992) gives confidence that this part of the energy balance is correct.

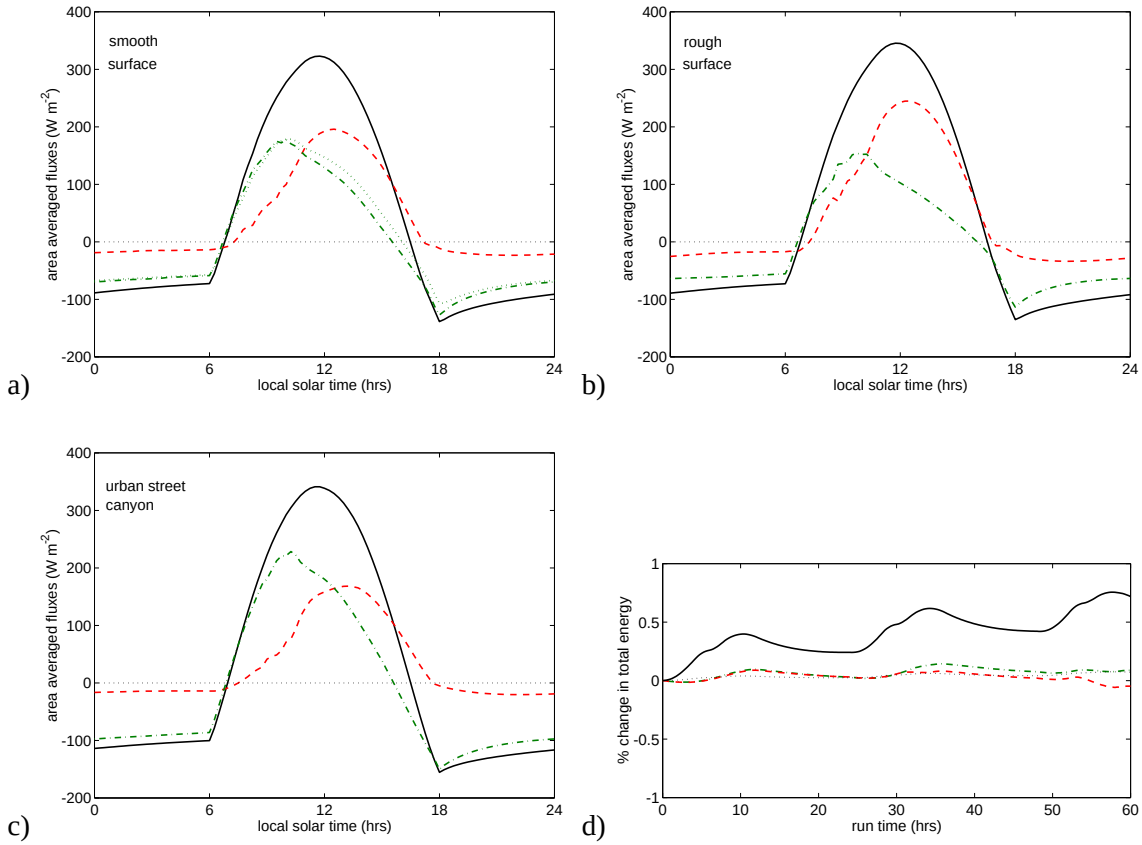

Figure 4.6: Diurnal energy balance profiles for the second day of the case study. (a) Energy balance for the smooth surface; black solid line, net radiation; red dashed line, green sensible heat flux; dash-dotted line, ground heat flux; dotted line, ground heat flux calculated from the top two layers of the discretized substrate temperature profile. (b) Energy balance for the roughened surface, lines as in (a). (c) Bulk energy balance for the canyon surface, line as in (a). (d) Profiles of the change in the total energy within the column (substrate and atmosphere) not explained by the accumulation of energy due to the net radiation. Black solid line, street canyon case; green dash-dotted line, smooth surface case; red dashed line, roughened surface case.

The phase differences between the peak values of the three terms relates to the diurnal temperature profiles. The solar radiative flux peaks at local midday but the emitted longwave radiative flux depends on the surface temperature and peaks after local midday. The result is a peak in the net radiation just before local midday. During the morning, a positive sensible heat flux acts to erode the stable boundary generated by nocturnal longwave radiative cooling. The difference between the surface and air temperature is therefore reduced and the sensible heat flux is small. Correspondingly the ground heat flux is large during the morning and reduces later as the surface-air temperature difference increases and the sensible heat flux increases. The ground heat flux therefore peaks in mid-morning and the sensible heat flux peaks in mid-afternoon. Stability effects on the transfer velocity, w_T in Equation (4.9), mean that the magnitude of the sensible heat flux in stable conditions is less than that in unstable conditions for the same surface-air temperature difference. By night, therefore, the surface energy balance is primarily a balance between the ground heat flux and the net radiation.

Figure 4.6(b) shows the energy balance from the coupled energy balance-boundary layer system with the horizontal surface with increased roughness. Comparing Figures 4.6(a) and 4.6(b) shows that the principal effect of increasing the roughness of a surface is to alter the partitioning between the ground heat and sensible heat forms. Increasing the surface roughness length acts to increase the turbulent mixing and transport from a surface via the transfer velocity w_T. The magnitude of the sensible heat flux for a given surface-air temperature difference is therefore increased and the ground heat flux correspondingly decreases in magnitude. There is also a small increase in the magnitude of the net radiation through the day. This results from the decrease in the diurnal variation in surface temperature, and therefore the emitted longwave radiation, which accompanies the altered sensible heat flux (see Figure 4.8(a)).

Figure 4.6(c) shows the bulk energy balance from the urban canyon. Comparing this energy balance to the other energy balances highlights many different effects. The ground heat flux is slightly advanced and increased in magnitude, the sensible heat flux is decreased in magnitude and delayed - opposite to the effects of increasing the surface roughness length. The net radiative flux is almost identical to the two flat-surface cases despite the large impacts of surface morphology on the radiative flux densities (Chapter 2). The causes of these differences relate to the increase in surface area and surface geometry on the individual facet energy balances as considered in detail in Section 4.5.2.

Comparing the three figures shows that the influence of surface morphology goes some way

to explaining the observed differences between rural and urban bulk energy balances (e.g. Cleugh and Oke, 1986). Surface morphology acts to increase the ground heat flux and delay the sensible heat flux while leaving the net radiation approximately the same. A horizontal surface with increased roughness does not give a satisfactory approximation to the full urban canyon surface so casts doubt on the usefulness of approximating urban areas as bare soil surfaces with increased roughness lengths. It should be noted here that the flat surface energy balances here are not representative of the energy balances of rural areas. The effects of moisture and plant canopies (e.g. Wallace and Verhoef, 1996; Finnigan, 2000) will also play a role in determining the differences between rural and urban bulk energy balances.

Figure 4.6(d) shows the change in the total energy of the soil-atmosphere column from 50 cm depth in the substrate to 2 km in the atmosphere, accounting for absorbed and emitted radiation at the surface, through the model runs. For a truly conservative system this change should be zero. The green dash-dotted line represents the change in total energy from the smooth surface system, the red dashed line that of the roughened surface system and the black solid line that of the canyon system. The horizontal surfaces show little unexplained change in total energy which gives confidence in the models. The total energy of the canyon system has a diurnal signal and a slight drift in time. The diurnal signal results from the approximations used to calculate the total energy in the lowest atmospheric layer. The drift in time is due to the maintenance of the internal building temperature which represents a source of energy. For this particular case this source of energy is equivalent to a 3–4 W m^{-2} anthropogenic heat source. In all cases the change in total energy is small.

4.5.2 Case study: The facet energy balances

The bulk energy balance for the canyon surface is comprised of the facet-averaged energy balances of the four canyon facets. Figure 4.7 shows these four energy balances; (a) is the energy balance for the roof facet, (b) the energy balance for the street facet, (c) the energy balance for the west-facing wall facet and (d) the energy balance for the east facing wall facet with the lines as in Figure 4.6. Unsurprisingly the energy balance of the roof facet is similar to that of the horizontal surfaces.

The principal effect of surface morphology on the energy balances of the canyon facets is the redistribution of the solar radiation. Facet elevation and orientation, together with shadowing, result in the spiked profiles in the net radiation profiles. The effects of reflected radiation can be

observed as secondary peaks in all three of the canyon energy balances. The shape factor effect is most prominent at night, reducing the magnitude of the net longwave radiative flux densities by a factor of 2–3 compared to the roof facet and the horizontal surface energy balances. Section 4.4 showed that increasing the surface area of the surface leads to a reduction in the flux densities from the surface. This does occur but not to the extent predicted. The combined effect of surface morphology is therefore dominated by the effects of surface geometry with the increase in surface area being a secondary importance.

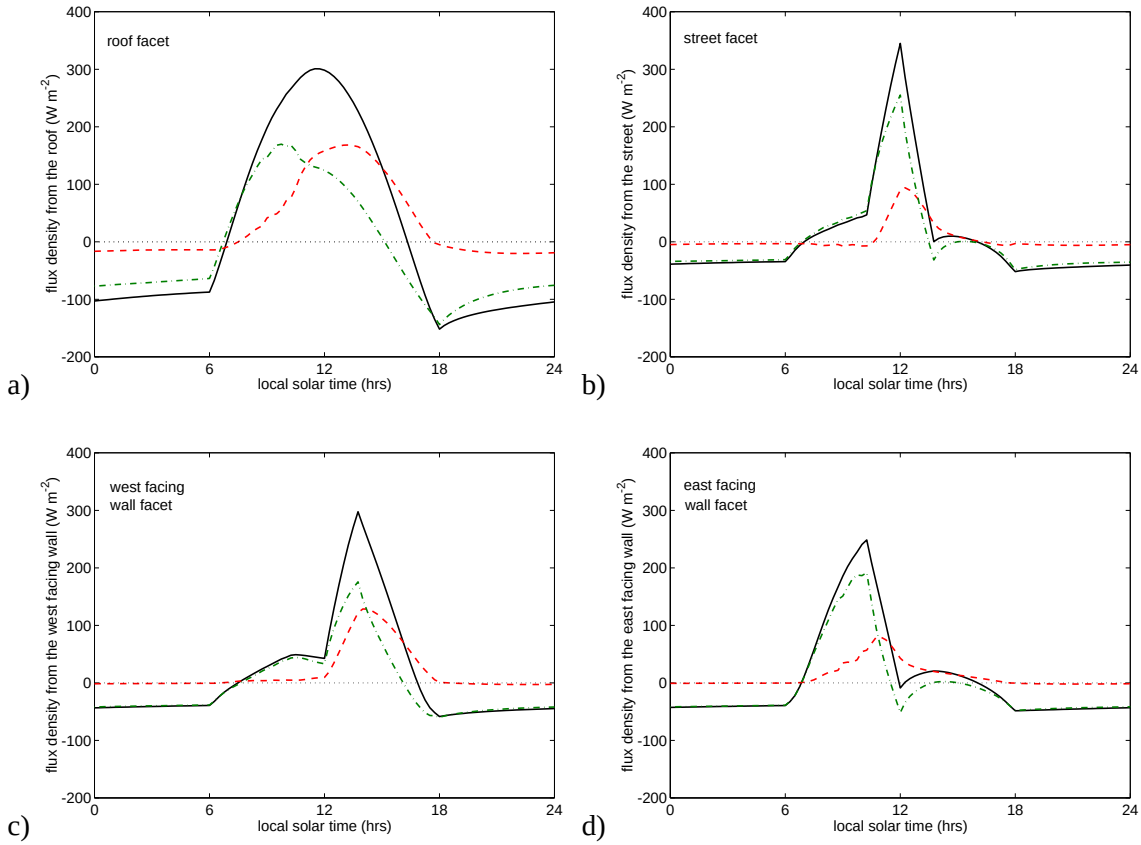

Figure 4.7: Diurnal energy balance profiles for the four canyon facets, lines as in Figure 4.6. (a) roof facet; (b) street facet; (c) west-facing wall facet; (d) east-facing wall facet.

In addition to the effects on the radiation, surface geometry reduces the transfer velocities for the sensible heat fluxes from the canyon facets (Section 3.6.4). This results in a change in the partition between the ground heat and sensible heat flux densities for the canyon facets with more energy passing into the substrate. This explains the increase in the bulk ground heat flux observed in Figure 4.6.

The change in the timings of the peak values of the fluxes in Figure 4.6 is also partly due to the reduction in the transfer velocities. A reduced sensible heat flux by day reduces the temperature

of the air particularly during the morning and correspondingly increases the surface temperature. The shape factor effect then slows the radiative cooling of the surface, maintaining the positive surface-air temperature differences longer into the afternoon (particularly for the west facing wall facet). This acts to delay the timing of the peak value of the sensible heat flux and delay (slightly) the transition to stable conditions in the early evening. Both of these features are observed characteristics of the urban energy balance (Cleugh and Oke, 1986; Oke, 1987).

Figure 4.7 shows that by night the sensible heat flux densities from the three canyon facets remain small. This is a feature common to a range of canyon geometries. The sensible heat flux from the canyon facets can remain positive over night for highly urbanised cases but the bulk sensible heat flux is never positive by night as the small fluxes from the canyon facets are countered by a larger negative flux from the roof facet (see Section 4.7).

4.5.3 Case study: Surface and boundary-layer temperatures

The surface energy balance is only one part of the energy balance/boundary-layer system. Even small changes in the surface energy balance can lead to large changes in the temperature at the surface or in the boundary layer. Figure 4.8 shows the diurnal temperature variation for the surface (a) and the 15 m potential air temperature (b). Solid lines are for the canyon surfaces, the green dash-dotted line for the smooth horizontal surface and the red dashed line for the horizontal surface with increased surface roughness.

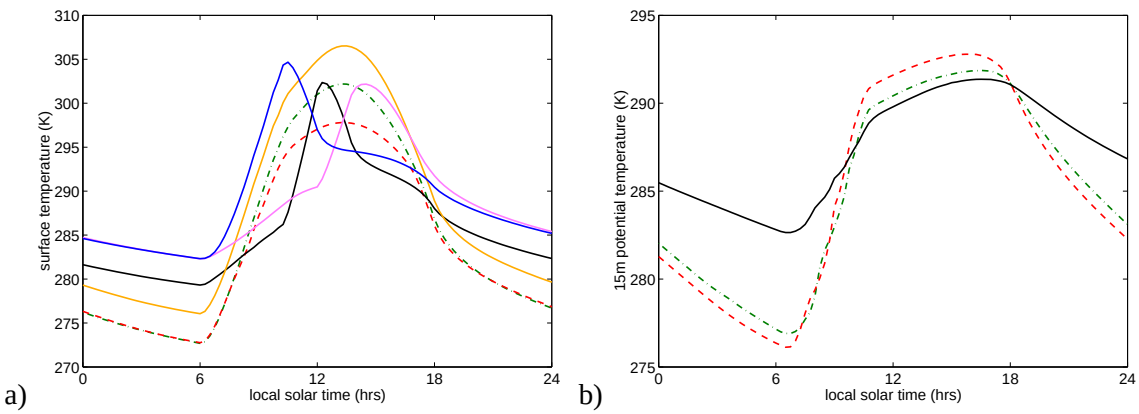

Figure 4.8: Diurnal temperature profiles from the coupled energy balance-boundary layer model. (a) Surface temperature profiles; green dash-dotted line, smooth surface; red dashed line, roughened surface; orange line, roof facet; black line, street facet; blue line, east facing wall facet; pink line west facing wall facet. (b) 15 m potential temperature profiles; green dash-dotted line, over smooth surface; red dashed line, over roughened surface; black solid line, over canyon surface.

Comparing the green and red lines illustrates the effects that increasing the surface roughness

has on the temperatures. Accompanying an increase in the magnitude of the sensible heat flux density (Figures 4.6(a) and (b)), there is a decrease in the maximum surface temperature and a decrease in the diurnal temperature range at 15 m. The increase in the transfer velocity due to the increase in the surface roughness length acts to couple the surface and air temperatures more strongly. The maximum surface temperatures achieved in unstable conditions are therefore reduced. By night the principal energy balance is between the ground heat flux and the net radiation resulting in surface temperatures which are very similar. Changing the surface roughness length acts to redistribute the energy in the column. The relative sizes of the heat capacities of the substrate and atmosphere mean that a small (indistinguishable) difference in the substrate temperature can correspond to a larger difference in the atmospheric temperature profiles at night, as seen in Figure 4.8(b).

The solid lines in Figure 4.8(a) show the surface temperatures of the canyon facets (orange is the roof facet, black the street facet, blue the east-facing wall facet and pink the west-facing wall facet). The non-uniformity of the solar radiation due to the elevation and orientation of the different facets and shadowing are again the dominant processes acting by day. There is a reduction in the diurnal range of the surface temperatures and an offset in the mean surface temperature. The reduction in the diurnal range of the surface temperatures is expected due to the increase in surface area (Section 4.4). The offset in the mean temperature results from the shape factor effect on the net radiation (Chapter 2) and the interactions between the surface and the boundary layer. The shape factor effect acts to reduce the longwave radiative cooling of the canyon facets, particularly at night, and gives the warmer nocturnal surface and air temperatures seen in the two figures. For the geometry considered, the shape factor effect reduces the longwave radiative cooling of the street facet less than that of the wall facets giving rise to the difference between the wall and street temperatures during the night. The shape factor effect by itself cannot explain the increased night time temperature of the roof facet when compared to the horizontal surfaces. This increased temperature arises due the interactions between the surface and the boundary layer. The reduced nocturnal cooling of the canyon facets leads to a reduction in the cooling of the boundary layer (the bulk sensible heat flux is reduced) and a reduction in atmospheric stability. This reduction in stability acts to further increase the transfer velocity for the roof facet (w_r) which is greater than that of a flat surface (Section 3.6.1). The roof and 15 m temperatures are therefore more strongly coupled during the night than a flat surface and the surface temperature does not cool as much despite no radiative impacts on the net radiation.

Figure 4.9 shows boundary layer potential temperature profiles from the three systems considered every three hours through the day. In each figure the black solid line is the profile above the canyon surface, the green dash-dotted line that over the smooth horizontal surface and the red dashed-line that over the horizontal surface with the increased surface roughness length. Only the lowest 500 m of the boundary layer is shown as above this level the differences between the cases are small.

Most of the boundary layer remains near-neutral throughout the day in all of the cases considered. The neutral profiles are established by deep turbulent mixing during the day and maintained through the night as there are no radiative processes acting in the boundary layer model and the turbulent cooling of a stable boundary layer acts only in the lowest layers. The differences between the neutral parts of the boundary layer profiles result from the differences in the time-integrated sensible heat flux from the three surfaces. The differences in the profiles are small since during the day, when the differences in the surface forcing are greatest, the boundary layer is deep, extending to over 1 km.

In a stable boundary layer, stability effects limit the depth through which turbulent mixing can occur and the boundary layer is shallower. Any differences in the surface forcing are therefore concentrated in this shallower layer and are likely to be of greater magnitude. The stability of the boundary layer is determined by the surface temperature, and therefore the surface energy balance, and the turbulent mixing within the boundary layer. The two horizontal surfaces have approximately the same surface temperature during the night (Figure 4.8). The increase in turbulent mixing due to the increased surface roughness length mixes the nocturnal cooling through a deeper layer. Increasing the surface roughness length therefore acts to deepen and cool the stable nocturnal boundary layer.

The large differences between the nocturnal boundary layers over the horizontal surfaces and the canyon surface illustrate the coupled nature of the system. The surface temperatures of the canyon facets remain warmer than those of the horizontal surfaces (Figure 4.8). With a boundary layer that has developed with the surface through the day, this automatically results in a reduction in the magnitude of the (negative) turbulent sensible heat flux and therefore a reduction in the stability of the boundary layer. However, two other boundary layer processes act to reinforce the nocturnal thermal differences between the boundary layers over the horizontal and canyon surfaces. Firstly, the increase in the bulk surface roughness has the same effect as before acting to spread the cooling in the vertical. Secondly, the turbulent mixing in the boundary layer is stabil-

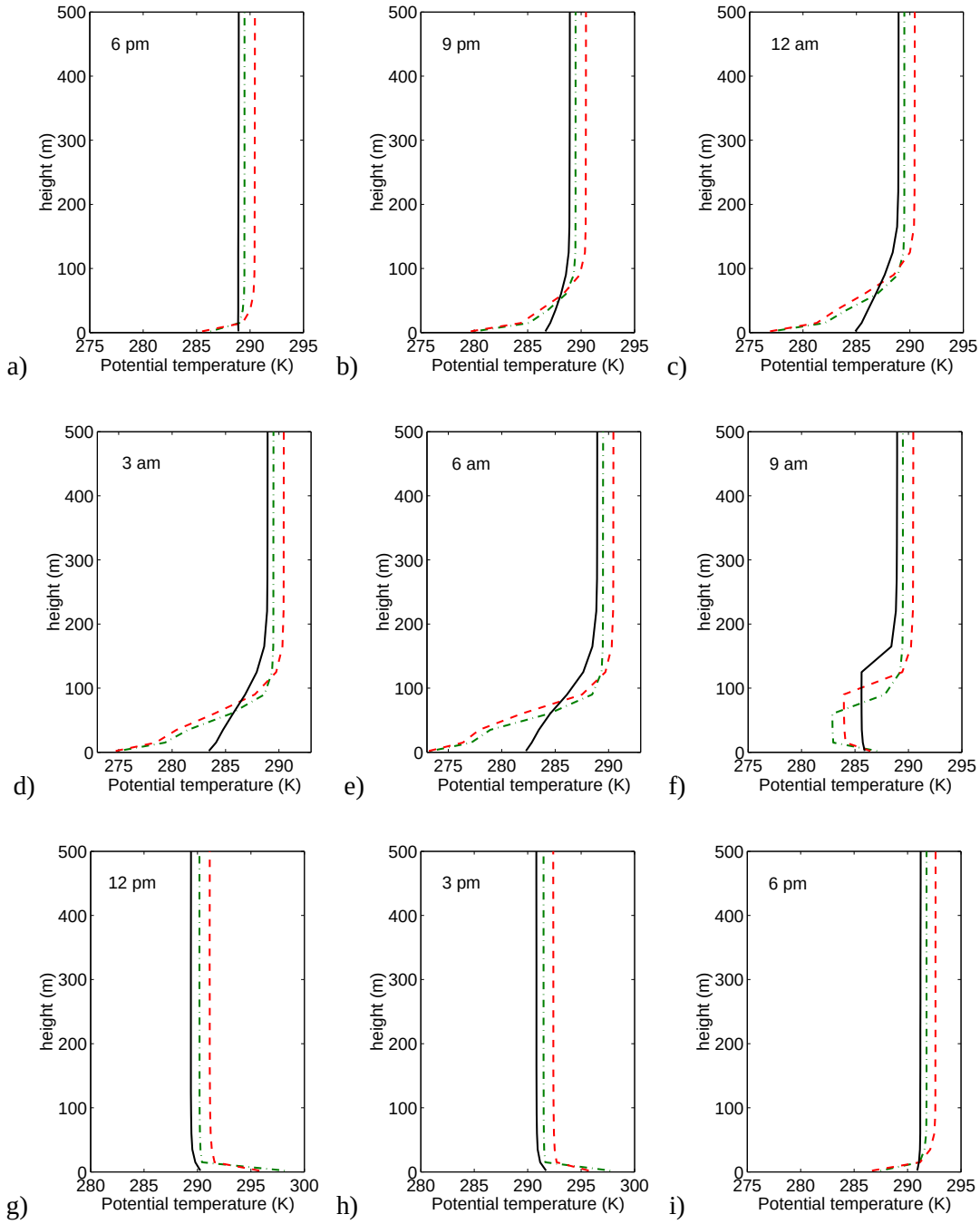

Figure 4.9: Boundary layer potential temperature profiles every 3 hours through the day. Green dash-dotted line, profile over smooth surface; red dashed line, profile over roughened surface; black solid line, profile over canyon surface.

ity dependent. A reduction in the stability of the boundary layer increases the turbulent mixing allowing heat from the overlying residual layer to be mixed downwards which reduces further the stability of the boundary layer by warming the lowest layers and deepening the stable boundary layer. The combined effects of surface morphology on the energy balance/boundary-layer system thus results in deeper, warmer, less stable nocturnal boundary layers when compared to a boundary layer over a horizontal surface. These boundary layer features are commonly observed during heat island conditions (e.g. Oke and East, 1971).

4.5.4 Case study: Summary

The boundary layer potential temperature profile and surface energy balance are interdependent. Differences between the potential temperature profile over different surfaces relate to physical processes acting in the energy balance, e.g. the nocturnal atmospheric temperature differences relate primarily to the shape factor effect on the longwave radiation. Increasing the surface area does act to decrease the temperature variation and reduce the mean flux densities as expected (Section 4.4); however, the accompanying effects of surface geometry often outweigh this simple expectation.

Surface geometry imposes a number of changes to the surface energy balance each with its own impact on the climatology of urban areas. These impacts are

- Shadowing and the shape factor effect on the net radiation are important effects determining the magnitude of the diurnal temperature variations. These are key impacts explaining the urban-rural differences in the mean surface temperature and the generation of surface and near-surface temperature differences during the night (e.g. Oke, 1987; Oke *et al.*, 1991).

- The increased bulk roughness length accompanying the change in surface geometry acts to deepen and reduce the stability of the nocturnal boundary layer. Increasing the bulk roughness length also increases the turbulent intensity of the urban boundary layer as compared to rural boundary layers (e.g. Roth, 2000).

- The geometric effect on the transfer velocities for the sensible heat flux densities from the canyon facets acts to alter the partition between the ground heat and sensible heat fluxes. In conjunction with an interacting boundary layer this explains the change in phase of the terms of the bulk energy balance of urban areas (e.g. Cleugh and Oke, 1986).

To capture the full effects of surface morphology on the urban energy balance all of these impacts must be incorporated.

4.6 The effects of incomplete treatment radiation

Chapter 2 showed how approximating the net radiation balance of the canyon facets by ignoring reflected radiation can yield large errors in the net radiative fluxes densities calculated. These errors can have dramatic effects on the modelled energy balance and boundary layer potential temperature profile as shown in Figure 4.10. For illustrative purposes a case is chosen when the approximate solutions to the radiation balance are expected to be inaccurate ($h_e/w_e = 2.75, w_e/r_e = 0.5, \varepsilon = 0.75, \alpha = 0.1$). However, some building materials do have emissivities of this order (Clarke, 1985). Figure 4.10(a) shows the bulk energy balance from the urban street canyon using the full radiation scheme. Figure 4.10(b) shows the bulk energy balance from the urban street canyon where the $\mathcal{R}_1$ approximation (only one reflection of radiation is considered) has been used for the interacting radiation terms. Figure 4.10(c) shows the bulk energy balance from the urban street canyon where the $\mathcal{R}_0$ approximation (no reflections of radiation are considered) has been used for the interacting radiation terms. In all figures the lines are the same as in Figure 4.6.

Figures 4.10(a)–(c) show that the principal effect of ignoring reflected radiation is that the net radiation is reduced throughout the day. The $\mathcal{R}_1$ and $\mathcal{R}_0$ underestimate the incoming radiation for the canyon facets (see Figures 2.4, 2.6 and 2.7) resulting in the reduction in the net radiation as shown in the figure. The underestimation of the net radiation has a large impact on the other terms of the energy balance and on both the surface and boundary layer temperatures. Figure 4.10(d) shows the surface temperatures from the two horizontal surfaces with the same material albedo and emissivity (green dash-dotted line, the smooth surface temperature; red dashed line, the roughened surface temperature) and the surface temperatures of the street facet from the three canyon energy balances (black, full energy balance; blue, $\mathcal{R}_1$ approximation; pink, $\mathcal{R}_0$ approximation). The approximations reduce the incoming radiation and therefore the surface temperatures. The accompanying reduction in the bulk sensible heat flux reduces the boundary layer temperature. Although the energy balances of the full and $\mathcal{R}_1$ approximations are similar, the coupled nature of the energy balance and boundary layer system results in large temperature differences. The full (infinite reflections) solution for the radiation interactions in an urban street canyon should therefore be used.

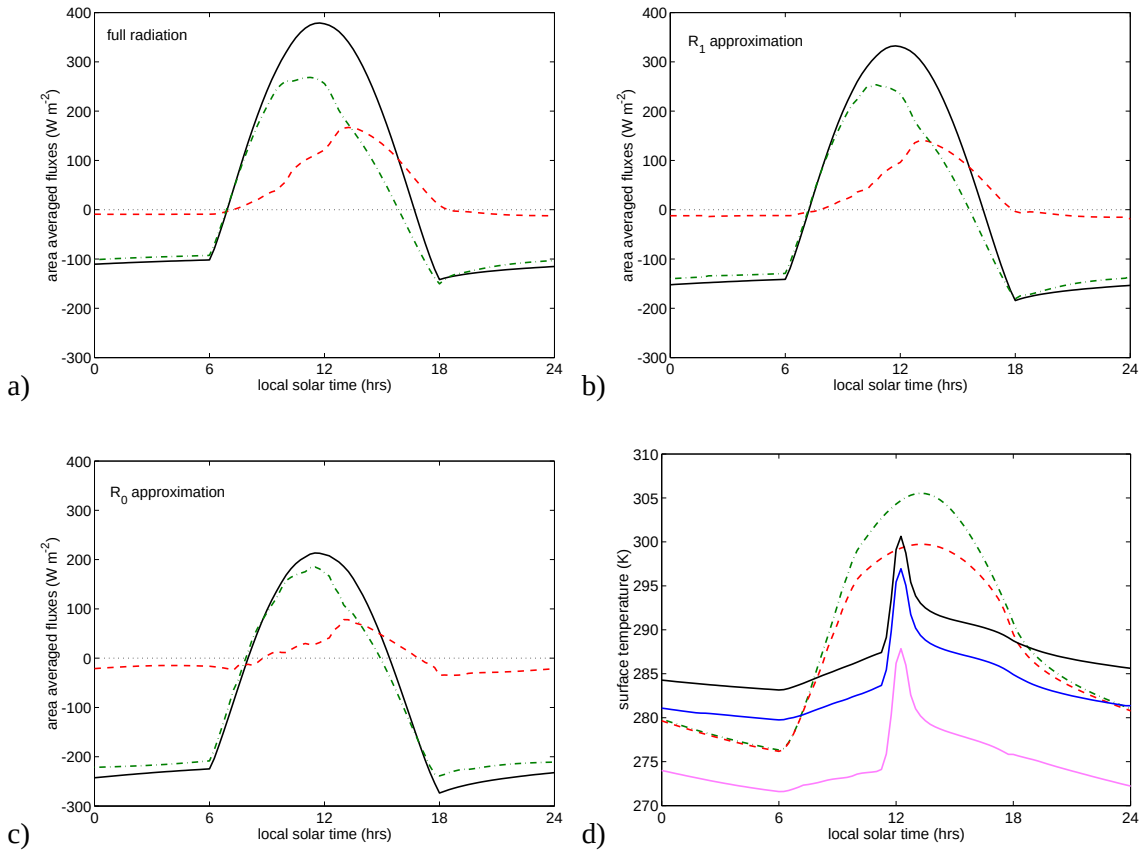

Figure 4.10: The effects of incomplete radiation on the energy balance and street surface temperature. (a) Bulk energy balance of the urban street canyon incorporating multiple reflections, lines as in Figure 4.6. (b) Bulk energy balance using the $\mathcal{R}_1$ approximation. (c) Bulk energy balance using the $\mathcal{R}_0$ approximation. (d) Surface (street) temperature profiles; green dash-dotted line, smooth surface; red dashed line, roughened surface; solid lines, street facet - black line, full radiation; blue line, $\mathcal{R}_1$ approximation; pink line, $\mathcal{R}_0$ approximation.

4.7 Sensitivity to urban morphology

The modifications to the local climate induced by an urban area vary across the town or city. Common features of this spatial variation are a sharp change in the climate at the edge of the city and a core region with large modifications to the climate located near to the city centre (Oke, 1987). The spatial variation in the modification to the local climate relates to the spatial variation in the energy balance and boundary layer. A range of observational campaigns of the bulk energy balance of urban areas show that the partitioning of energy into different forms at the surface varies between cities and across individual cities (Grimmond and Oke, 2002; Christen *et al.*, 2003). One possible cause of the variation in the observed bulk energy balance of urban areas is the variation of the underlying surface morphology. Are the spatial variations in the urban modifications to the local climate determined by the spatial variation of the surface?

The urban canyon energy balance model developed in Sections 4.1-4.3 is used to investigate the sensitivity of the coupled energy balance and boundary layer system to surface morphology. The urban street canyon has two independent morphological parameters, the canyon aspect ratio, h_e/w_e, and the ratio w_e/r_e. In real urban areas both these parameters vary spatially; here the two parameters are first varied separately and then varied together. In all cases the building height is constant at 10 m and located at 60°N, the day considered is the spring equinox.

4.7.1 Sensitivity to the canyon aspect ratio

A key parameter describing the extent of urbanisation is the canyon aspect ratio. Highly urbanised areas tend to have high canyon aspect ratios, $h_e/w_e > 1$, and high building heights. Figure 4.11 shows the diurnal variation of the bulk sensible heat flux (a) and 15 m potential temperature (b) calculated using the model developed in Sections 4.1-4.3 for a range of canyon aspect ratios. For these cases $w_e/r_e = 0.5$, and the canyon was oriented north-south.

Consider first the variation of the bulk sensible heat flux with canyon aspect ratio. Increasing the canyon aspect ratio decreases the diurnal range and maximum value of the bulk sensible heat flux. These effects are partly due to the increase in total surface area (Section 4.4). However, the dominant process occuring is the reduction in the transfer coefficients for the sensible heat flux densities from the street and wall facets as the canyon aspect ratio increases. A key feature in Figure 4.11(a) is the delay in the phase of the sensible heat flux, as considered in Section 4.5.1. This is more pronounced as the canyon aspect ratio is increased resulting in delayed peak values and delayed transitions to stable conditions in the early evening. Grimmond and Oke (2002) show a reduction in the magnitude of the sensible heat flux and a delay in its phase with increasing urbanisation for a range of North American cities.

The variation in the bulk sensible heat flux influences the diurnal variation of the 15 m potential temperature. The diurnal range is reduced at high canyon aspect ratios, due to both the reduced surface forcing (Figure 4.11(b)) and the offset in surface temperatures due to the shape factor effect on the net radiation. The maximum temperature difference between the flat surface and the urban street canyon occurs at dawn in all cases and shows a rapid change as the canyon ratio is increased from low values. This increase slows markedly as the canyon aspect ratio increases past $h_e/w_e = 1$. By night the key terms in the energy balance are the net radiative terms which, as Chapter 2 showed, vary rapidly around $h_e/w_e = 0.5$. At higher canyon aspect ratios the further

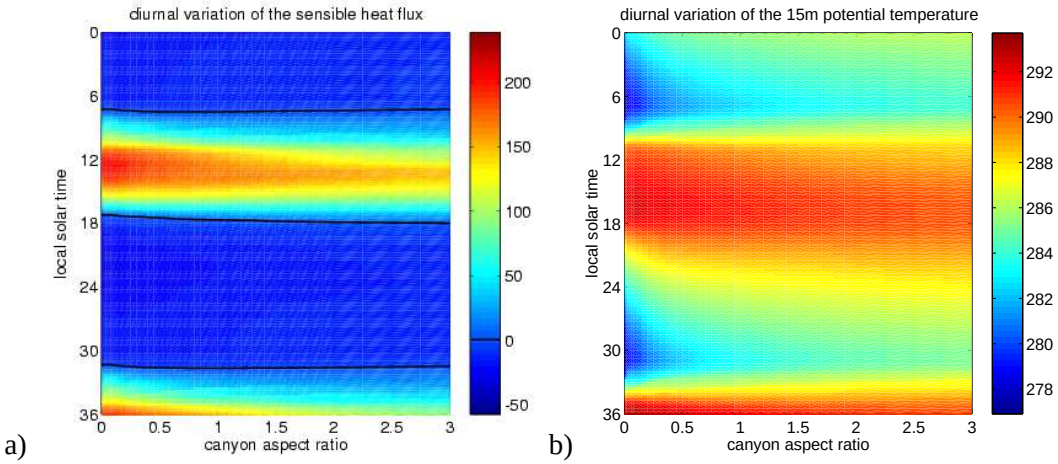

Figure 4.11: Hovmüller plots of the sensible heat flux (a) and 15 m potential temperatures (b) as the canyon aspect ratio is varied. Colour scales indicate the variation in W m^{-2} (a) and K (b). Values along the left-hand axis are for the smooth surface. Black lines in panel (a) mark the zero contour.

change in the radiative terms are small and result in little change in the potential temperature. This may explain the sharp change in thermal climate from rural to sub-urban conditions at the edge of a city.

4.7.2 Sensitivity to the planar area index

Changes in the planar area index, $\lambda_p = 1 - w_e/r_e$, more commonly denotes changes in surface usage than the degree of urbanisation. Residential areas typically have low values of the planar area index; industrial complexes with low broad workhouses, typically have higher planar area indexes. Figure 4.12 shows the diurnal variation of the bulk sensible heat flux (a) and 15 m potential temperature (b) calculated using the model developed in Sections 4.1-4.3 for a range of w_e/r_e values. For these cases the canyon aspect ratio was constant at $h_e/w_e = 1.0$, and the canyon was oriented north-south.

Varying w_e/r_e results in only small changes to the bulk sensible heat flux. As the sensible heat flux from the canyon is smaller than from the roof facet (Section 4.5.2) there is a corresponding decrease in the bulk sensible heat flux as w_e/r_e increases. The impacts of varying w_e/r_e on the phase of the bulk sensible heat flux is more complicated. The maximum bulk sensible heat flux remains delayed and its timing does not change as w_e/r_e is increased. The transition to stable conditions in the evening varies with w_e/r_ebeing delayed further as w_e/r_e is increased. These two features would appear to contradict each other if the physical mechanism which causes the delay in the sensible heat flux is the reduction of the transfer velocities and the feedback onto the

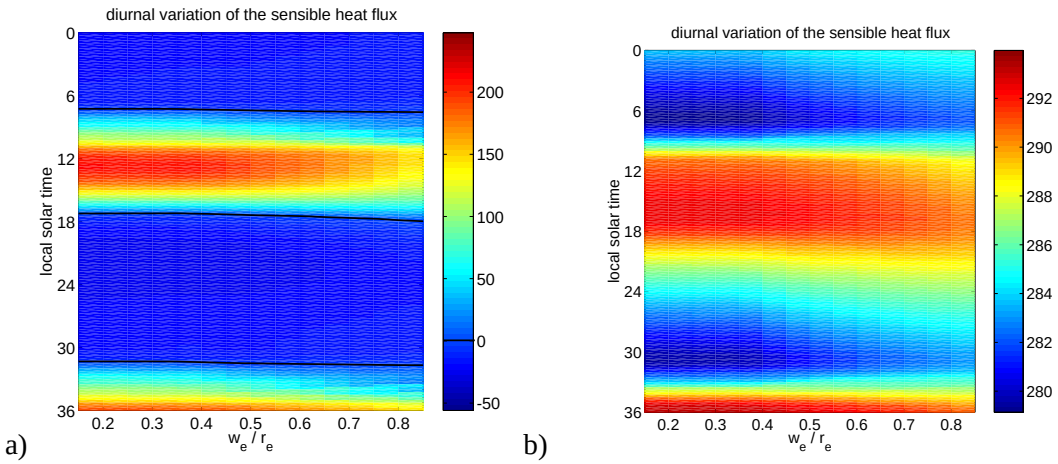

Figure 4.12: Hovmüller plots of the sensible heat flux (a) and 15 m potential temperatures (b) as w_e/r_e is varied. Colour scales indicate the variation in W m^{-2} (a) and K (b). Values along the left-hand axis are for the smooth surface. Black lines in panel (a) mark the zero contour.

boundary layer as suggested in Section 4.7.1.

The explanation for this apparent contradiction lies in the morphological dependence of the bulk roughness length and bulk displacement height of the canyon. Increasing the ratio w_e/r_e acts to decrease the displacement height leading to an increase in the transfer velocities for the sensible heat flux. This increase acts to reduce the phase delay of the peak value of the flux from the canyon fraction of the surface. The delay in the transition to stable conditions remains as this is partly due to the shape factor effect which is not altered.

Increasing the ratio w_e/r_e influences the 15 m potential temperature by reducing the diurnal variation. This is expected as a greater fraction of the surface is influenced by the shadowing and the shape factor effect on the net radiation which both act to reduce the diurnal temperature variation. The minimum temperatures do not however increase as much as expected as w_e/r_e increases. This is again due to the increase in the transfer velocities which, during the night, acts to cool the boundary layer.

4.7.3 Co-varying the canyon aspect ratio and planar area index

Commonly both the canyon aspect ratio and planar area index vary together across a town. Figure 4.12 shows the diurnal variation of the bulk sensible heat flux (a) and 15 m potential temperature (b) calculated using the model developed in Sections 4.1-4.3 for a range of canyon aspect ratios where now $w_e/r_e = 1/(1 + h_e/w_e)$ i.e. square bar roughness. For these cases the canyon was oriented north-south.

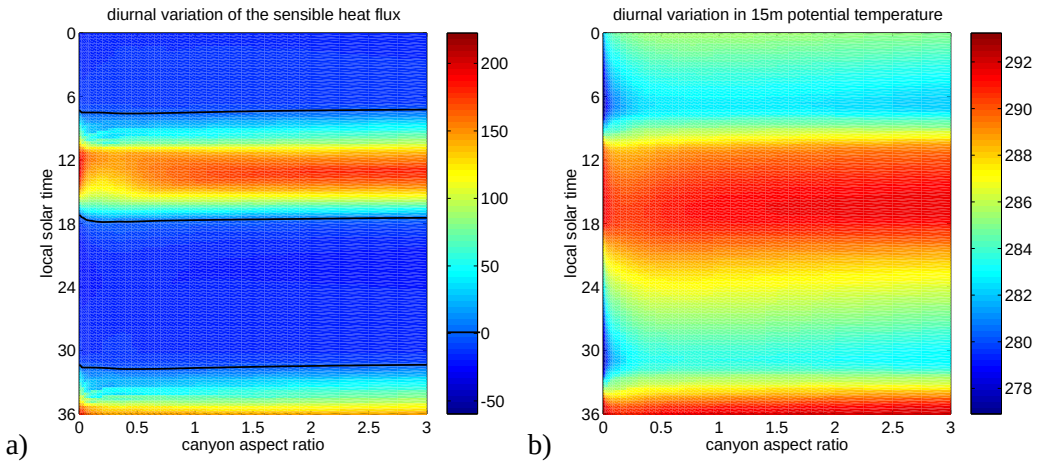

Figure 4.13: Hovmüller plots of the sensible heat flux (a) and 15 m potential temperatures (b) as the canyon geometry is varied as square bar roughness. Colour scales indicate the variation in W m^{-2} (a) and K (b). Values along the left-hand axis are for the smooth surface. Black lines in panel (a) mark the zero contour.

The effects of the initial dip in the transfer velocities for the sensible heat flux from the street facet around a canyon aspect ratio of $h_e/w_e = 0.25$ (Section 3.6.2) can be clearly seen in both the bulk sensible heat flux and the 15 m potential temperature particularly during the day. Otherwise the two effects of varying the canyon aspect ratio and planar area index together cancel to a large extent. This is a result of the competing effects of the reduction in the transfer velocities as the canyon aspect ratio and displacement height are increased being balanced by an increase in the offset of the temperatures due to the shape factor effect.

These plots show that surface geometry is a more important effect than the increase in total surface area. As h_e/w_e is increased past 0.5 the diurnal range of the 15 m potential temperature increases which is counter to the effect expected due to the increase in total surface area (Section 4.4). For instance the difference between the minimum temperatures over the canyon and flat surfaces for a canyon aspect ratio of $h_e/w_e = 3$ is smaller than for a canyon aspect ratio of $h_e/w_e = 0.5$. This is illustrates that the boundary layer responds to the bulk energy balance. For the geometry considered, at high canyon aspect ratios the surface resembles a flat but displaced surface (see Figure 1.5(c)). The bulk energy balance therefore principally resembles that of flat surface despite the increase in surface area.

4.7.4 Sensitivity to canyon orientation

A geometric factor not considered in detail until now is the orientation of the canyon. Figure 4.14 shows the diurnal variation of the bulk sensible heat flux (a) and 15 m potential temperature (b)

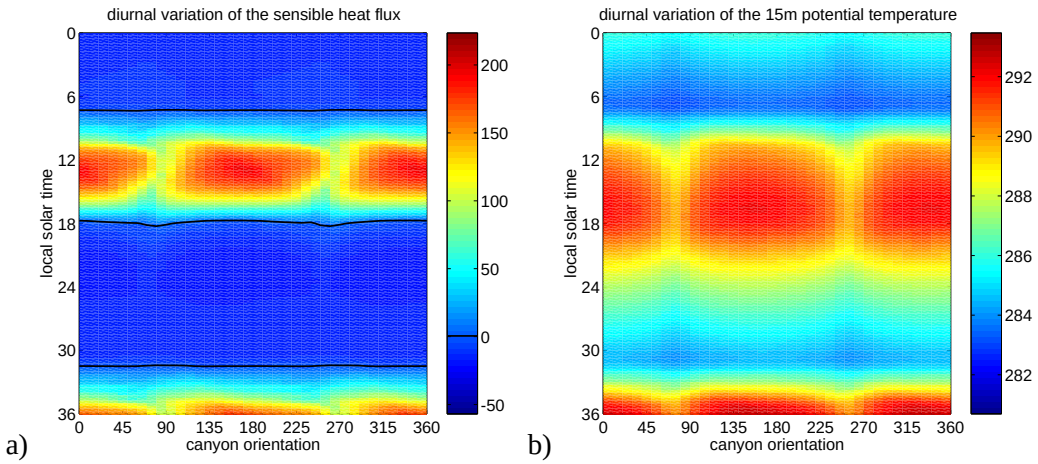

Figure 4.14: Hovmüller plots of the sensible heat flux (a) and 15 m potential temperatures (b) as the canyon orientation is varied. Colour scales indicate the variation in W m^{-2} (a) and K (b). Values along the left-hand axis are for the smooth surface. Black lines in panel (a) mark the zero contour.

calculated using the model developed in Sections 4.1-4.3 for the full range of canyon orientations. For these cases the canyon geometry was $h_e/w_e = 1.0$ and $w_e/r_e = 0.5$.

Canyon orientation primarily influences the direct component of the solar radiative flux densities (Appendix A). It also influences the transfer velocities for the sensible heat flux through the relative orientations of the wind and canyon as described in Section 4.2. Given the physical processes acting it is therefore unsurprising that canyon orientation should play a role. Of the two processes, the impacts of canyon orientation on the radiation balance are more pronounced. The boundary layer potential temperature shows a clear asymmetry during the day when the impacts on the direct solar radiation occur but little asymmetry during the night when only the impacts on the turbulent fluxes are acting. The variation of the bulk sensible heat flux with canyon orientation is of a comparable magnitude to the variation with the planar area index or square bar roughness. Energy balance models for use in numerical weather prediction models should therefore account for real scale variation in canyon orientation.

4.7.5 Sensitivity to urban morphology: Summary

This work has shown that the impacts of surface morphology on the bulk energy balance of, and boundary layer over, an urban area is a key factor determining the modifications to the local climate by urban areas. The effects of surface morphology on the coupled energy balance/boundary layer system explains the changes in magnitudes and phases of the terms of the bulk energy balance and goes towards explaining the observed variation in boundary layer potential temperature across an

urban area (e.g. Oke, 1987). The work reinforces the idea that the canyon aspect ratio is the key geometric parameter determining the thermal effects of the building array (Oke *et al.*, 1991) but in a context which includes a turbulent sensible heat flux and an interacting boundary layer.

The canyon aspect ratio is not the only geometric parameter that is important. Although of lesser importance, the planar area index does affect the bulk energy balance and the boundary layer and can counter the effects of increasing the canyon aspect ratio. Similarly, the orientation of the street canyon affects the coupled system markedly. This orientational effect must be considered when devising a energy balance model for urban areas for use in operational weather prediction models where the canyon orientation may not be known and/or poorly defined.

Varying the canyon parameters shows that surface morphology on its own cannot explain a key observed feature of urban areas, namely the maintenance of a positive bulk sensible heat flux through the night (e.g. Oke *et al.*, 1999). In all cases the one-dimensional boundary layer model gives a stable boundary layer during the night. An explanation is that in this one-dimensional model the only process which cools the boundary layer is a negative bulk sensible heat flux. During the night the dominant feature of the energy balance is long-wave radiative cooling at the surface which, in all cases considered here, cools the surface temperature below that of the overlying boundary layer air by early evening. To maintain a boundary layer that is cooler than the surface and thus a positive bulk sensible heat flux during the night as observed in heat island conditions, a physical process is needed which cools the boundary layer air ahead of the surface induced cooling. An investigation into the physical processes which can accomplish this are considered in Chapter 6.

4.8 Summary and conclusions

Chapter 4 considered the influence of surface morphology on the interactions between the urban energy balance and overlying boundary layer. An urban energy balance was formulated from the facet-averaged energy balances of the four facets of an urban street canyon and coupled to a one-dimensional boundary layer model (Busch *et al.*, 1976).

The influence of surface morphology on the energy balance was shown to explain several key features of the energy balance of urban areas. In an urban area the partitioning of energy between the ground heat flux and the turbulent sensible heat flux is altered to favour the ground heat flux (e.g. Grimmond and Oke, 2002). The net radiation remains approximately the same with the

peak value of the sensible heat flux occuring later and a general reduction in the magnitude of the sensible heat flux by night (e.g. Cleugh and Oke, 1986). These features are explained primarily by the shape factor effect on the longwave radiation, i.e. some of the incoming long-wave radiation for the canyon facets originates from the other canyon facets and not the sky (Chapter 2). The reduction in the transfer velocities for the sensible heat flux due to surface geometry is important in altering the phase of the terms of the bulk energy balance.

Observed climatological features of the urban boundary layer can also be explained by the influence of surface morphology on the processes coupling the surface and boundary layer. The boundary layer over the canyon surface is shown to vary little from that over a flat surface by day despite the large differences in surface forcing but with significant thermal excesses during the night (e.g Atkinson, 1985). This results from the depth of the boundary layer over which the differences in forcing are exerted (deep by day, shallow by night) and illustrates the importance of the boundary layer in controlling the depth and magnitude of the urban heat island (e.g. Arnfield, 2003). Nocturnal urban boundary layers are seen to be deeper, less windy, and less stable than their rural counterparts (e.g Atkinson, 1985). Here it is shown how surface morphology controls these differences. The key physical process resulting from surface morphology is the shape factor effect on the net radiation but other processes such as the increased surface roughness and variation of the turbulent fluxes with geometry are also important. These latter processes are important when explaining changes in the phase of the individual terms of the bulk energy balance.

The variation of the surface morphological influences on the energy balance and boundary system also explain, to some degree, the spatial patterns of the urban modifications to the local climate. For instance the shape factor effect has a rapid onset as the canyon aspect ratio is increased past 0.1, which may explain the sharp transition in climate at the edge of cities (e.g. Oke, 1987). Additionally, the core regions of cities experience the largest perturbations associated with the largest canyon aspect ratios and therefore largest shape factor effects. Although the canyon aspect ratio is the dominant geometrical ratio, the planar area index does influence the energy balance and boundary layer most notably through the induced changes to the turbulent exchange. Surface morphology is, however, unable, on its own, to explain the maintenance of positive sensible heat fluxes and neutral urban boundary layers during the night. This key observation of the urban boundary layer is considered further in Chapter 6.

CHAPTER FIVE

A simplified urban energy balance

5.1 Intoduction

The modifications to the local climate induced by urban areas can be instantaneously large and qualitatively important for their occupants (Oke, 1987; Dabbert *et al.*, 2000) therefore requiring accurate forecasts. Evidence for the urban modification of the local weather comes from rainfall distribution changes (e.g. Cotton and Pielke, 1995), the delay of frontal systems (e.g. Loose and Bornstein, 1977; Bornstein and Thompson, 1981) and the trigggering of convection (e.g. Bornstein and Lin, 2000; Rozoff and Adegoke, 2003) as well as the urban heat island studies (see Arnfield, 2003, for a review). Urban areas, however, remain a small fraction of the total land surface area of the Earth and there is little evidence to indicate that urban areas significantly modify the weather away from the local area. A possible method of forecasting the weather within urban areas is to take forecasts from numerical weather prediction models that do not incorporate urban areas and statistically downscale offline for the urban areas. Given the degree of interaction between the boundary layer and urban energy balance shown in the previous chapters it is unlikely that this approach would be satisfactory across the full range of urban surfaces and synoptic conditions. This poses a problem of how best to, and the required detail needed to, incorporate urban areas into numerical weather prediction models.

At the heart of this problem is the issue of scale (Section 1.1). The previous chapters showed, and much of the current understanding indicates (Britter and Hanna, 2003), that much of the impact of urban areas is determined by physical processes acting at the street scale and the subsequent feedback through the boundary layer. Numerical weather prediction models act at the city (or at most the neighbourhood) scale seeking to predict the bulk effects and not the fine scale features. Methods must therefore be identified which enable the impacts of the street scale processes on the

neighbourhood scale to be captured which rely only on information known at the neighbourhood scale and without the complexity of working at the street scale.

Accompanying this issue of scale is an issue of complexity. The urban canyon models possess a large number parameters specific to the street scale which must be specified (e.g. Masson, 2000). Two issues relate to these parameters when working within numerical weather prediction models. Firstly, working at the neighbourhood scale implies that the variation in these properties across the neighbourhood cannot be captured. Which value of these parameters is representative of the neighbourhood and how should they be determined? Grossman-Clarke *et al.* (2003) illustrates the complexity required to calculate some of these parameters from reality at only a moderate resolution. Secondly, the averaging length scale on which these parameters are calculated requires careful consideration. Is it possible to relate this length scale to the resolution of the model or some physically relevant length scale? Within climate modelling, where whole cities can fit into one grid box, both of these issues will be even more complex.

The parameterization of the surface energy balance within numerical weather prediction models must be kept as simple as possible. All of the major types of urban energy balance model (Section 1.3) have been incorporated into mesoscale weather prediction models (Best, 1998a; Taha, 1999; Masson *et al.*, 2002; Martilli *et al.*, 2002). Only the simple energy balance model of Best (1998a, 1999) is currently operational; the other models have been used to investigate specific events such as the heat island and urban circulations (Taha, 1999; Lemonsu and Masson, 2002; Martilli, 2002). The current Met Office Unified Model surface exchange scheme, MOSES (Essery *et al.*, 2001, 2003), is configured for surface heterogeneity but is not configured to allow for directly interacting surfaces. The urban street canyon model presented in Chapter 4 has direct interactions between the wall and street facets in both the radiative and turbulent terms (Sections 4.2.1 and 4.2.2). It would be desirable therefore if these interaction terms can be approximated.

This chapter therefore focusses on possible ways to approximate the urban canyon energy balance so that it can be incorporated into numerical weather prediction models yet which preserve the most significant features of the urban energy balance as highlighted in Chapter 4. Two approximations to the full urban street canyon energy balance model are presented in Section 5.2. A comparison between the two approximations and the full scheme is presented in Section 5.3. Finally, results from this chapter will be used to address the complexity of the model of the urban energy balance model required and the specification of required input parameters in numerical weather prediction models.

5.2 Approximations to the urban street canyon model

To simplify the urban street canyon model (Section 4.1) two approximations to the full urban street canyon model are investigated. Firstly, an average over all canyon orientations is taken to account for uncertainties and variation of the canyon orientation in real towns. This involves averaging the direct solar radiation term for the wall and street facets and averaging the wind speeds parallel and perpendicular to the street canyon when determining the resistance network for the turbulent sensible heat fluxes. This model resultant after this approximation is denoted as the $\mathcal{F}_4$ scheme. This approximated model could not be incorporated into the current MOSES scheme as it still retains interaction terms. Secondly, one of two further approximations was applied; a one facet approximation (denoted the $\mathcal{F}_1$ scheme) or a two facet approximation (denoted the $\mathcal{F}_2$ scheme). These two further approximations are used to determine the extent of simplification possible while capturing the most significant impacts of the urban street canyon energy model on the bulk energy balance and boundary layer.

Both the $\mathcal{F}_1$ and $\mathcal{F}_2$ schemes are formulated by taking averages, weighted by surface area, of the temperature profiles in the substrate of the different canyon facets and calculating how this averaged profile would respond to the averaged surface energy balance. In the $\mathcal{F}_2$ scheme the temperature profiles of the two walls and street facet are averaged. This leaves two facets, the roof facet and the composite canyon facet, with their energy balances interacting solely through the inertial sub-layer. In the $\mathcal{F}_1$ scheme the temperature profiles of the two wall, street and roof facets are all averaged. Figure 5.1 shows schematically the three schemes with the shading indicating those facets which respond to a common energy balance. Both of these approximations could be incorporated into the current MOSES scheme as the interaction terms are removed although their effects on the averaged temperature profile are kept.

Figure 5.1: Schematic of the three approximations to the full urban street canyon energy balance model - the shading indicates separate substrate temperature profiles. (a) the $\mathcal{F}_4$ scheme with four temperature profiles; (b) the $\mathcal{F}_2$ scheme with two temperature profiles; (c) the $\mathcal{F}_1$ scheme with one temperature profile.

A key part of the averaging process is that the influences of canyon geometry on the energy

balances are maintained. Consider first the $\mathcal{F}_2$ scheme; a temperature profile $T_{\mathcal{F}_2}$ is formulated as the average, weighted by surface area, of the temperature profiles T_{st}, T_{uw} and T_{dw} together with an average volumetric heat capacity for the three facets $c_{s\,\mathcal{F}_2}$, namely

$$(w_e + 2h_e)\, T_{\mathcal{F}_2} = w_e T_{st} + h_e \left(T_{uw} + T_{dw}\right), \tag{5.1}$$

$$(w_e + 2h_e)\, c_{s\,\mathcal{F}_2} = w_e c_{s\,st} + h_e \left(c_{s\,uw} + c_{s\,dw}\right). \tag{5.2}$$

The energy balance to which this temperature profile responds is given as

$$\begin{aligned} \Delta z\, c_{s\,\mathcal{F}_2} \frac{\partial T_{\mathcal{F}_2\,1/2}}{\partial t} &= \frac{\Delta z}{w_e + 2h_e} \left[w_e c_{s\,st} \frac{\partial T_{st\,1/2}}{\partial t} + h_e c_{s\,uw} \frac{\partial T_{uw\,1/2}}{\partial t} + h_e c_{s\,dw} \frac{\partial T_{dw\,1/2}}{\partial t} \right], \\ &= \frac{\Delta z}{w_e + 2h_e} \left[w_e (1-\alpha_{st}) \tilde{K}_{sf\,st} + h_e (1-\alpha_{uw}) \tilde{K}_{sf\,uw} + h_e (1-\alpha_{dw}) \tilde{K}_{sf\,dw} + \dots \right., \end{aligned} \tag{5.3}$$

where the subscript $_{1/2}$ refers to the surface layer of the substrate and the tilde indicates the orientational average. The approximation $T_{st} = T_{uw} = T_{dw} = T_{\mathcal{F}_2}$ is used in all terms including the interaction terms present on expanding the square brackets.

Applying the approximation $T_{st} = T_{uw} = T_{dw} = T_{\mathcal{F}_2}$ can introduce differences in the bulk energy balance obtained from the $\mathcal{F}_4$ and $\mathcal{F}_2$ schemes as well as the energy balances for the individual facets. These differences arise from the averaging of terms involving the co-variation of the temperature profile and facet specific parameters. For example the sensible heat flux density out of the canyon air volume is given by $H_c = \rho c_p w_c \left(\theta(z_2) - T_c\right)$, where T_c is a linear combination of the facets' surface temperatures as given by Equation (4.16). Unless the transfer velocities w_{st}, w_{uw} and w_{dw} are equal then applying the approximation will introduce an error in T_c and therefore H_c from the $\mathcal{F}_4$ and $\mathcal{F}_2$ schemes will differ. Similarly differences between the two schemes can arise through the co-variation of the temperatures of the different facets with the direct solar radiative flux densities, with the thermal conductivities or heat capacities of the substrates, or with the shape factor effect on the longwave radiative flux densities. Part of this work is to assess the importance of these co-varying terms in determining the bulk energy balance of an urban street canyon. Differences between the two schemes can be reinforced via a feedback occuring through the influence of stability on the turbulent mixing in the boundary layer and the subsequent impacts on the bulk sensible heat flux.

The differences between the $\mathcal{F}_4$ and $\mathcal{F}_2$ schemes imposed by averaging these co-variating terms are however expected to be small for two reasons. Firstly, the differences between the temperature profiles of the separate facets (the $\mathcal{F}_4$ scheme) and the averaged temperature profile (the $\mathcal{F}_2$ scheme) are much smaller than absolute value of the temperature. This implies that the differences in the emitted longwave flux densities will be small. Secondly, the effects of surface morphology on the facet specific parameters and the individual terms of the energy balance are commonly a factor of two or more. This is commonly much greater than the variation of the facet specific parameters between the different facets. It follows that the differences between the two schemes resulting from averaging the three temperature profiles will be small when compared to those associated with the combined effects of surface morphology. The exception to this general rule are the impacts of averaging the direct solar radiative flux densities which is the primary cause of the differences between the facets (Section 4.5). It follows that convoluted canyon morphologies, which impose greatly different direct solar flux densities on the wall and street canyon facets, are likely to impose large differences between the $\mathcal{F}_4$ and $\mathcal{F}_2$ schemes.

In practical terms, the influence of surface morphology on the resistances to transport (r_1–r_8) and on the canyon air temperature (Equation (4.16)) is kept but the possible differences between the surface temperatures in Equation (4.16) have been removed. Similarly, the surface temperatures used in the calculation of the emitted longwave radiation from the canyon facets are now equal but the effects of surface morphology on the shape factor effect and multiple reflections of radiation (Chapter 2) are kept. In this way the influence of surface morphology on the radiative and turbulent sensible heat fluxes is preserved but now there is only one surface and substrate temperature for the three canyon facets.

The $\mathcal{F}_1$ scheme is formulated in an equivalent way. A temperature profile $T_{\mathcal{F}_1}$ is formulated as the average, weighted by surface area, of the temperature profiles of all four facets together with an averaged volumetric heat capacity for the facets $c_{s\,\mathcal{F}_1}$, namely

$$(r_e + 2h_e)\, T_{\mathcal{F}_1} = w_e T_{st} + (r_e - w_e) T_{rf} + h_e \left(T_{uw} + T_{dw}\right), \tag{5.4}$$

$$(r_e + 2h_e)\, c_{s\,\mathcal{F}_1} = w_e c_{s\,st} + (r_e - w_e) c_{s\,rf} + h_e \left(c_{s\,uw} + c_{s\,dw}\right). \tag{5.5}$$

The energy balance to which this averaged temperature profile responds is

$$\Delta z\, c_{s\,\mathcal{F}_1} \frac{\partial T_{\mathcal{F}_1\,1/2}}{\partial t} = \frac{\Delta z}{r_e + 2h_e} \Bigg[w_e c_{s\,st} \frac{\partial T_{st\,1/2}}{\partial t} + (r_e - w_e) c_{s\,rf} \frac{\partial T_{rf\,1/2}}{\partial t} + h_e c_{s\,uw} \frac{\partial T_{uw\,1/2}}{\partial t} + h_e c_{s\,dw} \frac{\partial T_{dw\,1/2}}{\partial t} \Bigg]. \quad (5.6)$$

Differences between the $\mathcal{F}_4$ and $\mathcal{F}_1$ schemes occur as with the $\mathcal{F}_2$ scheme. Here, however the differences between the co-variation terms of the roof facet and of the street and wall facets are larger than those between the street and wall facets and so averaging over the co-varying terms is expected to lead to larger differences.

The evolution of the temperature profiles (Equations (5.1) and (5.4)) requires two boundary conditions. The first boundary condition is given by expanding Equations (5.3) or (5.6) but the second boundary condition is a final consideration. This second boundary condition is only of concern if the depth of the substrate is shallow enough that the diurnal signal is influenced by the boundary condition (Section 4.5). Here this boundary condition is a weighted average of the boundary conditions on the facet substrate temperature profiles and the depth of these substrates is sufficient that the boundary condition does not play a significant role.

5.3 Comparison between the $\mathcal{F}_1$, $\mathcal{F}_2$ and $\mathcal{F}_4$ schemes

For any simplification of the urban street canyon energy balance to be useful, the bulk energy balance and boundary layer potential temperature profiles should be similar to the $\mathcal{F}_4$ scheme. The three schemes were used for the same forcing conditions as Section 4.5 for a range of canyon geometries.

Figures 5.2 and 5.3 show the differences in each of the terms of the energy balance between the $\mathcal{F}_2$ and $\mathcal{F}_4$ schemes (left panels) and $\mathcal{F}_1$ and $\mathcal{F}_4$ schemes (right panels). In each case the solid line is the difference in net radiation, the dashed line the difference in the bulk sensible heat flux and the dash-dotted line the difference in the ground heat flux. The left and right panels are plotted on the same vertical axis for ease of comparison.

Figure 5.2 shows how the different schemes fare as the canyon aspect ratio is varied for a constant value of $w_e/r_e = 0.5$. As the averaging of the direct solar radiative flux densities imposes the largest differences between the schemes it is expected that at low canyon aspect ratios the

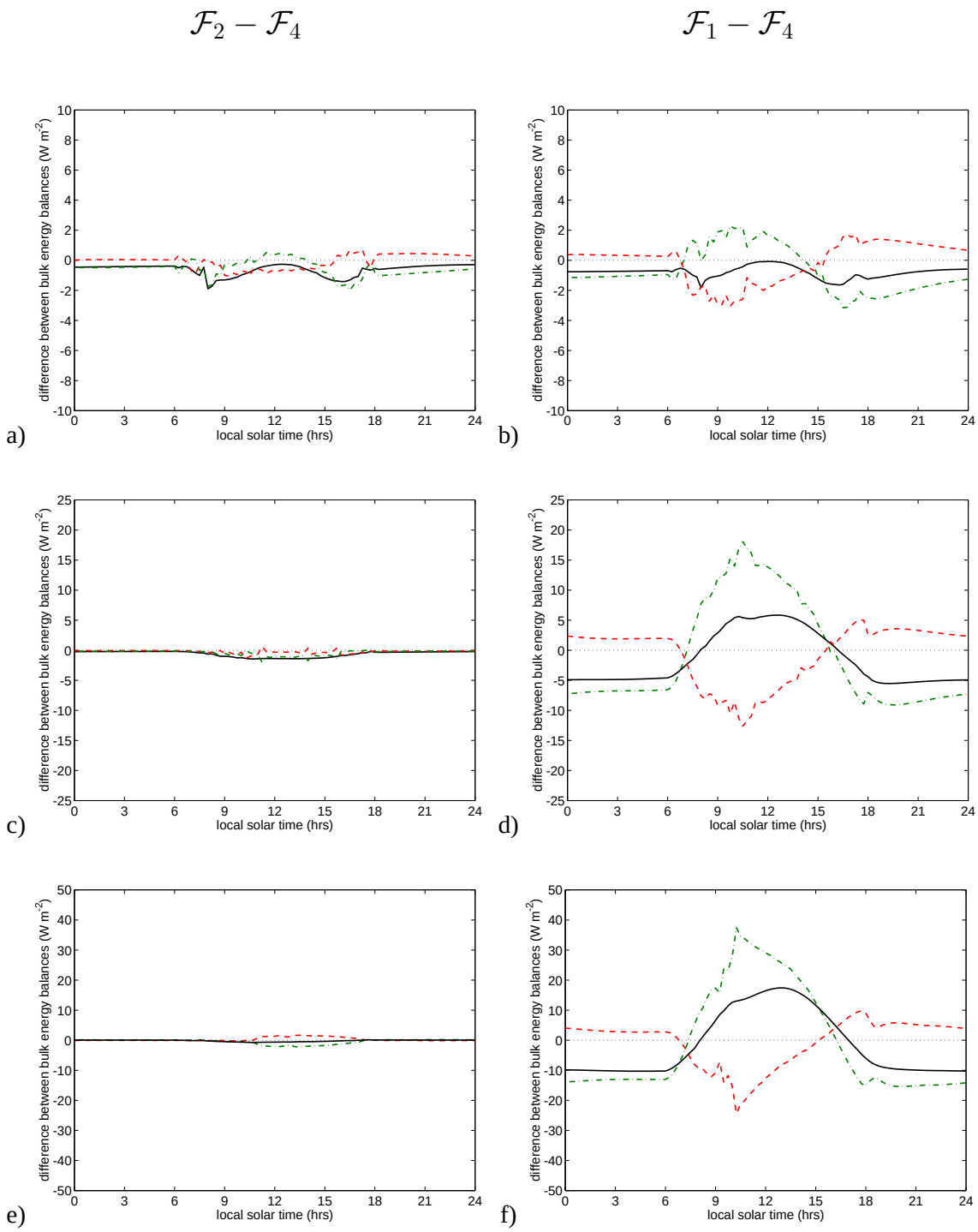

Figure 5.2: Differences between the energy balances of the three approximations. Left panels, differences between the $\mathcal{F}_2$ and $\mathcal{F}_4$; right panels, differences between the $\mathcal{F}_1$ and $\mathcal{F}_4$. Black solid lines, difference in the net radiative flux; green dash-dotted lines, difference in the ground heat flux; red dashed lines, difference in the sensible heat flux. Panels (a) and (b) $h_e/w_e = 0.25$; panels (c) and (d) $h_e/w_e = 1.0$; panels (e) and (f) $h_e/w_e = 2.0$; all panels $w_e/r_e = 0.5$.

three schemes should be similar. Indeed at small canyon aspect ratios (top panels $h_e/w_e = 0.25$) both approximations are accurate with differences of only a few percent occuring. As the canyon aspect ratio is increased (middle panels $h_e/w_e = 1.0$, bottom panels $h_e/w_e = 2.0$) both approximations become less valid, however the $\mathcal{F}_1$ scheme becomes much worse than the $\mathcal{F}_2$ scheme. The differences between the $\mathcal{F}_1$ and $\mathcal{F}_4$ schemes can be as much as 40% of the value of the flux itself. This degree of error renders the $\mathcal{F}_1$ approximation of little practical value. The $\mathcal{F}_2$ scheme remains accurate for all canyon aspect ratios. A similar pattern of differences occurs if the canyon geometry is varied with the square bar geometry (see Section 4.7.3).

Figure 5.3 shows how the differences between the three schemes vary as w_e/r_e is varied and the canyon aspect ratio is held constant at $h_e/w_e = 1$. The degree of variation between the cases shown is smaller than when the canyon aspect ratio is varied; however, there are differences in this variation between the two schemes. The differences between the $\mathcal{F}_2$ and $\mathcal{F}_4$ schemes always remain small but are greatest when w_e/r_e is high (bottom panel $w_e/r_e = 0.8$). The differences between the $\mathcal{F}_1$ and $\mathcal{F}_4$ schemes is greatest at intermediate values of w_e/r_e (middle panel $w_e/r_e = 0.5$). The degree of agreement between the $\mathcal{F}_2$ and $\mathcal{F}_4$ schemes shows that the averaging over the co-varying terms does not impose large differences.

A comparison of the timings of the maximum and minimum values of the terms of the energy balance for the three approximations shows no change in the phases of the fluxes with the approximations. This suggests that the physical processes determining the phase shifts in the urban energy balance, namely the effects of surface morphology on the diffuse longwave radiation and the transfer velocities, have been preserved. Comparing the value of the fluxes at specific time allows a quantitative examination of the differences between the approximations. Table 5.1 gives a comparison of the differences in the maximum ground heat flux between the three schemes across the full range of surface morphologies. This quantitative analysis confirms the qualitative analysis from Figures 5.2 and 5.3 and illustrates the importance of the non-uniformity of the direct solar radiative flux densities in determining the bulk effect of the urban street canyon.

The $\mathcal{F}_2$ approximation (bracketed numbers) is always more accurate than the $\mathcal{F}_1$ approximation (unbracketed numbers). Both approximations degrade at high canyon aspect ratios due to the averaging over the canyon facets which removes the non-uniformity of the solar forcing (Equation (5.3)). The two approximations show different patterns as w_e/r_e is varied. This again relates to the non-uniformity of the solar forcing, only this time it refers to the non-uniformity between the fully lit roof facet and the partially lit canyon facets. The $\mathcal{F}_2$ approximation is least accurate at

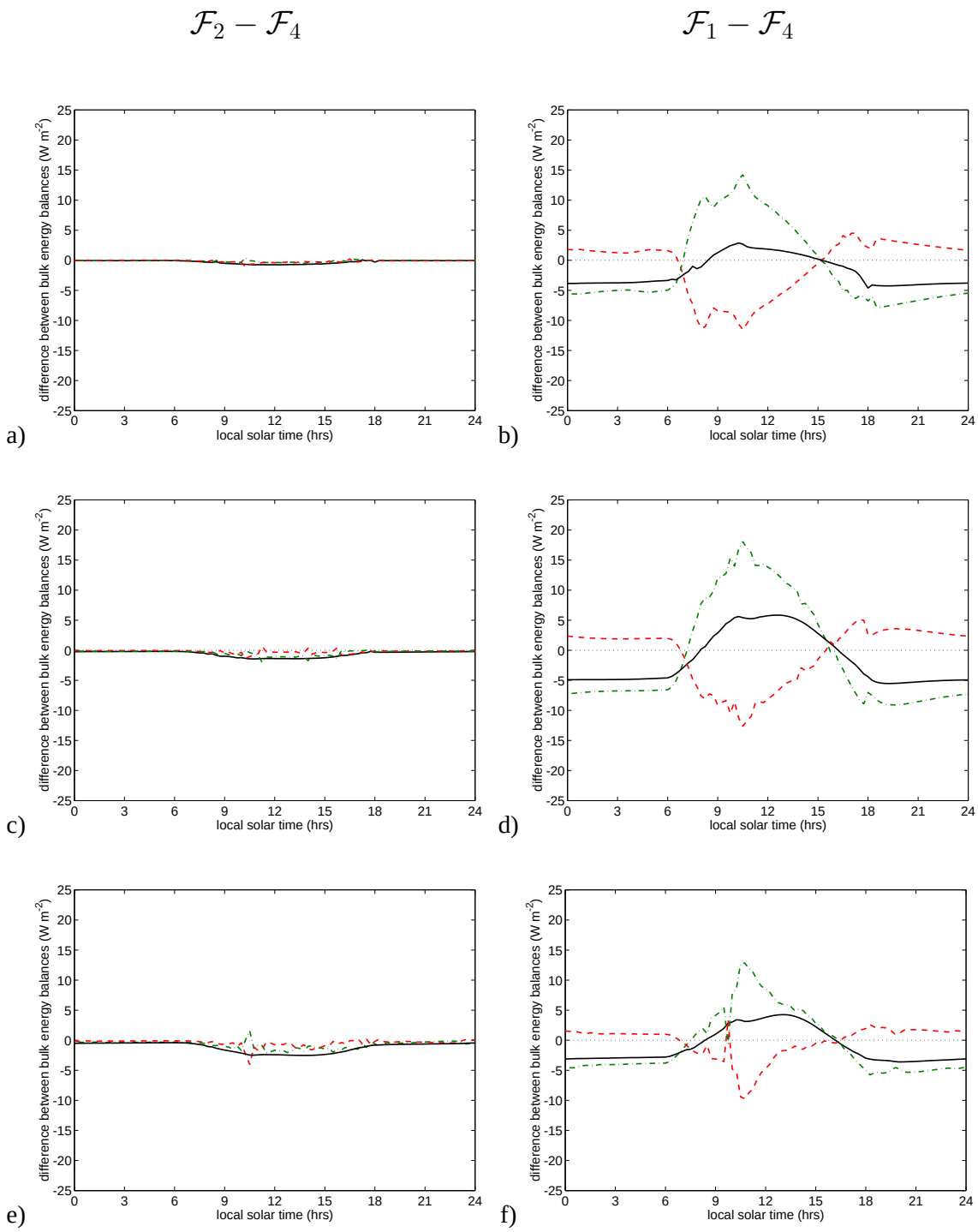

Figure 5.3: Differences between the energy balances of the three approximations. Left panels, differences between the $\mathcal{F}_2$ and $\mathcal{F}_4$; right panels, differences between the $\mathcal{F}_1$ and $\mathcal{F}_4$. Black solid lines, difference in the net radiative flux; green dash-dotted lines, difference in the ground heat flux; red dashed lines, difference in the sensible heat flux. Panels (a) and (b) $w_e/r_e = 0.2$; panels (c) and (d) $w_e/r_e = 0.5$; panels (e) and (f) $w_e/r_e = 0.8$; all panels $h_e/w_e = 1.0$.

Table 5.1: Difference (%) in the maximum bulk ground heat flux from the four facet model and the two approximate models for a range of canyon geometries. Unbracketed numbers refer to the $\mathcal{F}_1$ approximation; bracketed numbers refer to the $\mathcal{F}_2$ approximation.

$\mathbf{w_e/r_e}$	$\mathbf{h_e/w_e}$				
	0.25	0.5	1.0	2.0	4.0
0.2	1.0 (<0.1)	3.5 (0.4)	8.2 (0.3)	17.6 (0.2)	26.7 (0.1)
0.35	1.1 (0.1)	3.2 (0.2)	8.0 (0.4)	18.6 (0.4)	26.5 (0.6)
0.5	1.2 (0.1)	2.9 (0.3)	7.9 (0.5)	16.9 (0.5)	20.5 (1.2)
0.65	1.1 (0.2)	2.7 (0.5)	7.3 (0.7)	10.2 (0.7)	14.6 (0.9)
0.8	0.9 (0.2)	1.0 (0.3)	4.8 (0.6)	6.3 (0.6)	7.5 (0.7)

high values of w_e/r_e. The averaging of the solar forcing over the canyon facets is most prominent for these surface morphologies as the non-uniformity between the roof and canyon is preserved. Conversely, the $\mathcal{F}_1$ approximation, with the additional averaging over the roof facet, is least valid at low to mid values of w_e/r_e. This reflects both averaging across fully lit and partially lit surfaces and the surface area onto which the direct solar radiative flux is impinging (Equation (5.6)). The values of these differences shows that for a wide range of canyon morphologies the $\mathcal{F}_2$ approximation is sufficiently accurate that other uncertainties in the model will introduce larger errors than this approximation. However, there is only a limited range of canyon morphologies where the $\mathcal{F}_1$ approximation is sufficiently accurate for use.

Figure 4.10 showed that small differences in the bulk energy balance can result in large differences in the boundary layer temperature profile. Figure 5.4 shows the impacts that the differences in the bulk energy balances from the three schemes have on the boundary layer potential temperature for the case study considered in Section 4.5. The black solid line is the boundary layer potential temperature from the $\mathcal{F}_4$ scheme, the red dashed line is that from the $\mathcal{F}_2$ scheme, and the green dash-dotted line that from the $\mathcal{F}_1$ scheme at midday (left panel) and midnight (right panel). The differences between the potential temperature profiles show the same characteristics as in Section 4.5.3 with small differences during the day and larger differences at night relating as before to the depth of the boundary layer on which the different surface forcings act. Reflecting the small differences between the bulk energy balances from the $\mathcal{F}_2$ and $\mathcal{F}_4$ schemes, there is no distinguishable differences between the potential temperature profiles from these two schemes. A larger difference is observed in the potential temperature profiles from the $\mathcal{F}_1$ and $\mathcal{F}_4$ schemes at midnight, which is sufficient to invalidate the approximation.

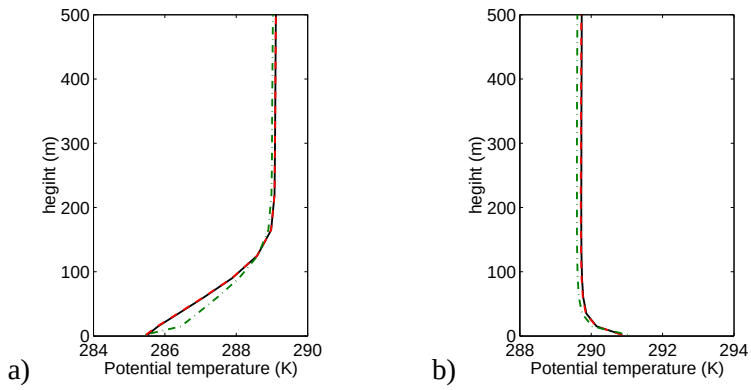

Figure 5.4: Potential temperature profiles from the three approximations. (a) Profiles at midnight; (b) profiles at midday. Black solid line, profile from the $\mathcal{F}_4$ scheme; red dashed line (overlying solid black line), profile from the $\mathcal{F}_2$ scheme; green dash-dotted line, profile from the $\mathcal{F}_1$ scheme

5.4 Summary and conclusions

Chapter 5 considered the complexity of urban energy balance model needed to capture the properties of the urban street canyon in as simple a method as possible. Two approximations were compared to the orientationally averaged form of the urban energy balance model presented in Chapter 4 across a range of surface morphologies.

From this comparison we conclude that, provided the substrate depth is deep enough that the diurnal signal is not influenced by the bottom boundary condition, two facets are needed to represent urban areas in operational weather prediction models. A single-facet surface energy balance cannot simulate the bulk energy balances or potential temperature profiles from two or more interacting surfaces. This includes the single-facet surface energy balance where the interaction terms have been preserved in an approximate form. Differences do occur between the four-facet ($\mathcal{F}_4$) and two-facet schemes ($\mathcal{F}_2$) but these are smaller than errors expected due to uncertainties in other parts of the model. The approximate solutions also show, as expected, that the influence of surface morphology is most keenly felt with highly convoluted surfaces. This is due to the thermal differences that occur over the roof and within the street canyons when the canyon aspect ratio is high due to the shadowing, and hence non-uniformity, of the direct solar radiation.

This chapter has shown that the averaging of the direct solar radiation is the primary cause of differences in the bulk energy balances of the four- ($\mathcal{F}_4$), two- ($\mathcal{F}_2$) and one-facet ($\mathcal{F}_1$) schemes. Therefore the orientational averaging performed to account for uncertainty in the orientation of street canyon in real cities plays an important role in determining the accuracy of, in particular, the $\mathcal{F}_2$ scheme. In a system where the orientational averaging had not been performed the difference

between the solar fluxes for the wall and street facets is greater and therefore the $\mathcal{F}_2$ scheme would not perform as well. However, the sensitivity to canyon orientation of the full canyon energy balance model is sufficiently large (Section 4.7.4) that unless there is a known preferred canyon orientation the orientationally averaged street canyon energy balance should be used.

These approximations do not address the complexity of the input parameters needed. The surface material properties are now averaged and so cannot reasonably take measured values and as such now resemble tunable parameters. Other parameters such as the mean building height, canyon aspect ratio, planar area index and bulk roughness length remain tied to the surface morphology and require determining from the surface land usage. In addressing the length scale over which these properties should be averaged there are two natural criteria. Firstly, parameter changes on less than two grid lengths act as numerical noise. Secondly, Coceal and Belcher (2004) and Barlow *et al.* (2004) show there is an adjustment length scale for the mean wind and turbulent exchange when a flow impacts on an array of buildings. Averaging over a length scale less than either of these two lengths is therefore unreasonable. Chapter 6 will address this issue further.

Finally, Chapters 4 and 5 have shown that all aspects of surface morphology play an important role in determining the urban impact on the local climate. In particular, any model for the urban energy balance which does not include the impacts of surface morphology on the radiation balance, on the bulk roughness length and displacement height and on the turbulent exchange is unlikely to be valid across the full range of urban surfaces.

CHAPTER SIX

Adjustment of the boundary layer over urban areas

6.1 Introduction

Much consideration has gone into understanding the impacts of urban areas on the local climate in terms of the characteristics of the local buildings (e.g. morphology, material properties (Oke *et al.*, 1991)). In particular, the influences that these characteristics have on the energy balance and boundary layer system must explain many of the observed differences between urban areas and their rural surroundings. Clear relationships do exist between some climate diagnostics and these characteristic properties of urban areas (e.g Oke, 1987). However, the hoped-for correlation between the spatial variation in the surface morphology and the spatial variation of the urban impacts is not found. For instance, Bärring *et al.* (1985) show that while the spatial variation of the building geometry and the differences in the street surface temperature in Mälmo, Sweden is highly correlated, the correlation with the differences in near-surface air temperature (the urban heat island) is much smaller and often not statistically significant. Now the interactions between the surface energy balance and the boundary layer are key in determining the urban impacts on the climate. Therefore to fully understand the causes of these impacts both the surface and the boundary layer need to be correct.

Chapter 4 considered the effects of surface morphology on the energy balance and boundary layer in a fully equilibrated, one-dimensional, scenario. The spatial scale of most urban areas (1–10 km) is usually much less than the fetch required to establish a fully equilibrated boundary layer (e.g. Garratt, 1992). Additionally, urban areas themselves are rarely homogeneous because the building characteristics typically vary on short (100's m) length scales. The continual adjustment of the boundary layer as it progresses across an urban area is therefore likely to play a key role in determining the impact of an urban area.

The equilibrated scenarios considered in Chapter 4 showed that many observed features of urban areas can be explained by the effects of surface morphology on the energy balance. However, some key observed features of the urban impact were not satisfactorily captured. Firstly, the diurnal variation in the atmospheric urban heat island is commonly observed to peak a few hours after dusk (Oke, 1987), whereas the one-dimensional model has this peaking at dawn. Secondly, the potential temperature profiles of the boundary layers over urban areas and their rural surroundings approach each other at high altitudes (Oke and East, 1971) unlike the one-dimensional simulations. Finally, the bulk sensible heat flux is observed to remain positive over night (e.g. Oke *et al.*, 1999) whereas the one-dimensional model cannot sustain a positive heat flux after sunset. This is particularly important for applications considering pollution dispersal as the degree of turbulent dispersion is determined by the stability of the boundary layer.

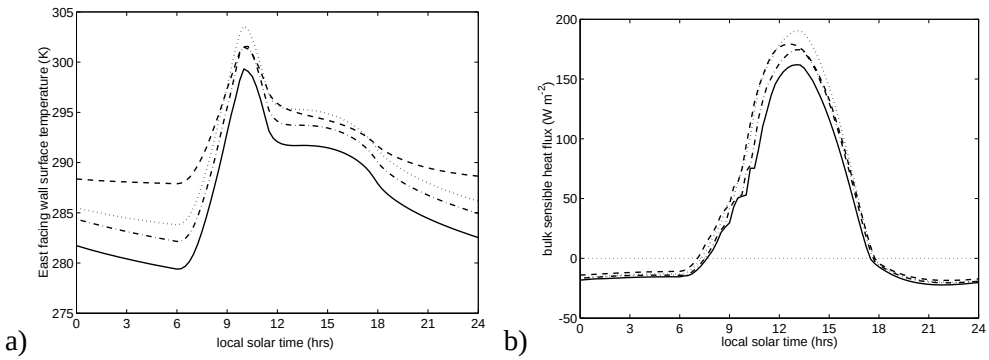

Figure 6.1: Diurnal profiles of the surface temperature of the east facing wall (a) and the bulk sensible heat flux (b) calculated using the coupled canyon energy balance and boundary layer model of Chapter 4. Solid line, case where the wall and roof facet internal temperatures vary with a zero flux boundary condition; dash-dotted line, case where the internal building temperature is raised but still varies according to a zero flux boundary condition; dotted line, the internal building temperature is raised and fixed (the case shown in Chapter 4); dashed line, as dotted line with the material properties of the wall facets altered so that the depth of penetration of the diurnal temperature signal $\left(\mathfrak{D} = \left(86400k/\pi c_s\right)^{1/2}\right)$ is doubled. This is representative of an uninsulated wall.

A range of physical mechanisms have been proposed to explain the maintenance of neutral nocturnal boundary layers including changes in the building material properties, increased storage of energy during the day which is then released at night and anthropogenic heat sources (e.g. Oke, 1987). Sensitivity studies with the coupled energy balance-boundary layer model show that the stable nocturnal boundary layers are always generated in a one-dimensional setting. Varying model properties such as the surface material conductance or heat capacity and raising and fixing the internal building temperature do play a significant role in determining the substrate temperature profiles (see Figure 6.1(a)). However, none of these changes results in positive nocturnal bulk

sensible heat fluxes (Figure 6.1(b)). Stable boundary layers are produced despite large changes in the surface and near surface temperatures; this again illustrates the coupled nature of the system.

A positive bulk sensible heat flux requires the surface temperatures, in some suitably averaged sense, to be warmer than the potential temperature of the inertial sub-layer. During the early evening and night the dominant processes occuring in the surface energy balance is longwave radiative cooling. Therefore to maintain a positive bulk sensible heat flux through the night requires that the boundary layer air cools ahead of the surface. The only process acting to cool the boundary layer in the one-dimensional boundary layer model is a negative bulk sensible heat and therefore stable boundary layers are generated during the night. The divergence of longwave radiative fluxes in the atmosphere can cool the boundary layer. However, the urban surface cools less than the rural surroundings due to the shape factor effect which reduces the divergence of the radiative fluxes and the subsequent cooling of the boundary layer over an urban area. Therefore if radiative divergence in the boundary layer is the explanation for positive nocturnal heat fluxes this should occur more often over rural areas than urban areas which is not the case. Furthermore anthropogenic heat sources act to warm the surface and near surface boundary layer which cannot explain the boundary layer cooling. Together this suggests that another physical mechanism is responsible for the generation of positive nocturnal sensible heat fluxes.

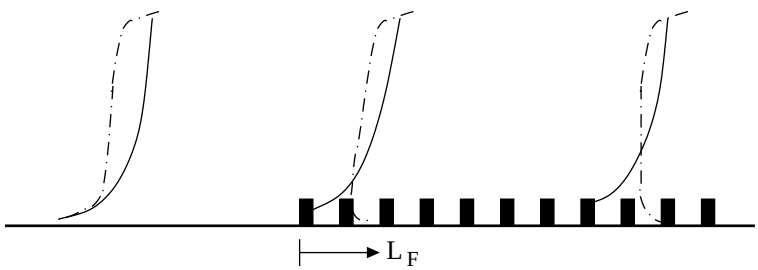

Figure 6.2: Schematic of the adjustment of nocturnal boundary layer profiles to a warmer, rougher urban surface. Solid line, vertical profile of the wind responding to increased roughness and displacement. Dash-dotted line, potential temperature profile eroding the stable boundary layer due to the warmer surface. L_F denotes the distance from the change in surface type.

This chapter investigates whether or not advection can explain these observations. If it can then advection is expected to also play a key role in determining the evolution of the heat island measured within the urban canopy of real cities. A simple two-dimensional scenario is considered, namely the adjustment of a fully equilibrated rural boundary layer to an urban surface, as shown schematically in Figure 6.2. The method used to incorporate the advective process is described in Section 6.2. The impacts of advection on the temperatures and the surface energy balance

are described in Section 6.3 and finally, the implications of this work for operational numerical weather prediction models are considered in Section 6.4.

6.2 Representation of advection in a one-dimensional setting

The adjustment of the boundary layer to an urban area requires that advection from one surface to another is possible. There are a range of methods to do this which include using a full three-dimensional atmospheric model (e.g. Lemonsu and Masson, 2002), using a two-dimensional transect model (e.g. Bornstein, 1975) or parameterising advection in a single column model. For simplicity, this last approach is taken here.

The adjustment of a boundary layer in equilibrium with the energy balance of a flat (smooth) surface to the energy balance of the urban canyon surface is investigated. The diurnal cycle of the boundary layer over the flat surface is calculated as in Chapter 4. The prognostic equations for the atmospheric boundary layer over the canyon surface appropriate to this two-dimensional advection problem are

$$\frac{\partial \bar{u}}{\partial t} + \bar{u}\frac{\partial \bar{u}}{\partial x} = -f(\bar{v} - v_g) - \frac{1}{\rho}\frac{\partial}{\partial z}\left(\rho\,\overline{u'w'}\right), \tag{6.1}$$

$$\frac{\partial \bar{v}}{\partial t} + \bar{u}\frac{\partial \bar{v}}{\partial x} = f(\bar{u} - v_u) - \frac{1}{\rho}\frac{\partial}{\partial z}\left(\rho\,\overline{v'w'}\right), \tag{6.2}$$

$$\frac{\partial \bar{\theta}}{\partial t} + \bar{u}\frac{\partial \bar{\theta}}{\partial x} = -\frac{1}{\rho}\frac{\partial}{\partial z}\left(\rho\,\overline{\theta'w'}\right), \tag{6.3}$$

where the pressure perturbation term $\left(\partial p'/\partial x\right)$ and the co-variation terms (e.g. $\overline{u'\partial u'/\partial x}$) have been neglected in Equations (6.1)–(6.3). The transition in the surface type occurs along the line $y = 0$ so that $\partial/\partial y \equiv 0$. The pressure perturbation term has been shown to be small away from the immediate change in surface type for a change in surface roughness (Belcher *et al.*, 1990) and with a change in displacement height (Belcher *et al.*, 2003). The co-variation terms are neglected using a scaling argument. As before the turbulent fluxes are parameterised using the first-order closure, turbulent diffusivity approach (Appendix B) with K_h and K_m determined from the local wind and potential temperature profiles. The surface boundary conditions are determined from the Reynolds stress and the bulk sensible heat flux at the surface.

To incorporate advection into the one-dimensional column model, the advection terms (e.g.

$\bar{u}\,\partial\bar{\theta}/\partial x$) must be approximated. The approach used is here is a simple first order finite difference approximation. Given an upstream boundary layer profile $\bar{u}_F$, $\bar{v}_F$, and $\bar{\theta}_F$, the advection terms in the boundary layer are approximated by

$$\bar{u}\frac{\partial\bar{u}}{\partial x} = \bar{u}\frac{\bar{u}-\bar{u}_F}{L_F}, \tag{6.4}$$

$$\bar{u}\frac{\partial\bar{v}}{\partial x} = \bar{u}\frac{\bar{v}-\bar{v}_F}{L_F}, \tag{6.5}$$

$$\bar{u}\frac{\partial\bar{\theta}}{\partial x} = \bar{u}\frac{\bar{\theta}-\bar{\theta}_F}{L_F}, \tag{6.6}$$

where L_F is the distance from the change in the surface type. This simplified approach has been successfully used to incorporate the effects of local advection in the UK Met Office Site Specific Forecast Model and shown to be accurate at least for small fetches (Clark *et al.*, 1997; Dunlop and Clark, 1997; Clark and Hopwood, 2001). The influence of the change of surface type on the upstream profile (e.g. Belcher *et al.*, 2003; Coceal and Belcher, 2004) is not considered here.

Hence in practice, two models are run together in parallel. Firstly, the one-dimensional model of Chapter 4 is run to determine the temporal evolution of the boundary layer over the homogeneous flat surface. Secondly, the one-dimensional model incorporating the advective terms is run over the urban canyon surface. The two models are run synchronously with matched time steps to enable the vertical profiles of the wind and potential temperature to be used in the advection terms over the urban canyon surface. The two models have been run for a range of fetches, L_F. The sequential adjustment of the boundary layer as it progresses over the new surface is allowed for by the fetch dependence of the advection terms. Close to the change in surface type the fetch is small and the advection term strongly forces the boundary layer profiles towards those of the upstream boundary layer. Conversely at large distances from the change in surface type the boundary layer evolves in equilibrium with the new surface and the advection term plays little or no role in determining the evolution of the boundary layer. The energy balance of the urban street canyon has been orientationally averaged to represent the variation of street orientations across a real city as discussed in Chapter 5. The influence of advection and fetch on the surface and boundary layer temperatures and on the bulk energy balance are considered in the next section. The particular case considered is the case study of Chapter 4, namely where $z_{0m} = 0.01$ m, $h_e/w_e = 1.0$, $w_e/r_e = 0.5$, at 60°N on the spring equinox. The surface material properties are held constant at

$k = 0.75\,\mathrm{WK^{-1}m^{-1}}$ and $c_s = 1.5 \times 10^6\,\mathrm{JK^{-1}m^{-3}}$.

6.3 Impacts of advection

A number of processes occur as a boundary layer passes from one surface type to another. Both a dynamical adjustment due to a change in the roughness length and the displacement height and a thermodynamical adjustment due to a change in the energy balance can occur with distance from the change in surface type. The quantitative impacts of these processes, and the sequential adjustment and feedback through the boundary layer, on the bulk energy balance of the urban street canyon and on the boundary layer potential temperatures allows an assessment of the importance of advection.

6.3.1 Diurnal cycle of temperatures

The diurnal pattern of the surface and near-surface air temperature is affected by the adjustment process within the boundary layer. Figure 6.3(a) shows the diurnal pattern of the street surface temperature and Figure 6.3(b) the diurnal pattern of the 15 m potential temperature for five cases considered. The thin solid line shows the profile for the upstream flat surface and is that given in Section 4.5. The thick solid line shows the profile for the equilibrated urban canyon surface (i.e. no advection term). The dash-dotted, dotted and dashed lines show the profiles for the urban canyon surface at distances of 100 m, 1,000 m and 10,000 m downstream of the surface change respectively.

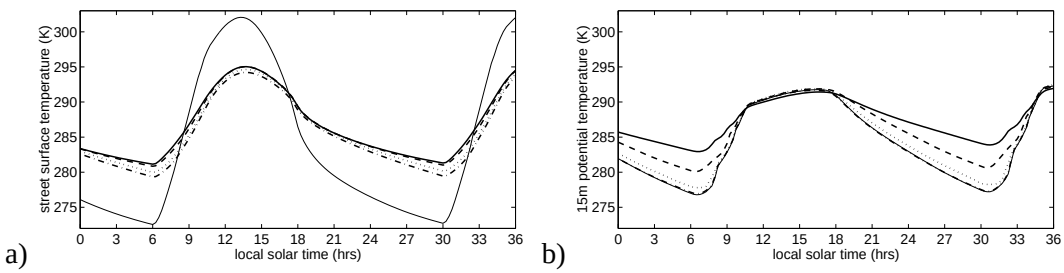

a) b)

Figure 6.3: Diurnal temperature profiles from the coupled model incorporating advection. (a) street surface temperature; (b) 15 m potential temperature. Thin solid line, upstream profile; thick solid line, fully adjusted profile; dash-dotted line, profile after 100 m adjustment to the new surface; dotted line, profile after 1,000 m adjustment to the new surface; dash-dotted line, profile after 10,000 m adjustment to the new surface.

The effects of urbanisation on the surface and near-surface temperatures are mainly felt during the night time. The surface temperature is shown to adjust to the local canyon morphology after

even a very short fetch. Only 20–25% of the difference between the two equilibrated profiles occurs between fetches of 100 m and 10,000 m fetch showing that the adjustment process is of secondary importance when considering the street surface temperature. The physical mechanism dominating the surface temperature change is the shape factor effect on the net radiation. This process depends only on the local geometry and therefore occurs immediately at the change in surface type. The large reduction in the maximum street surface temperature (as compared to Figure 4.8(a)) is due to the orientational averaging performed on the canyon energy balance.

The 15 m potential temperature shows a different dependence with fetch as seen in Figure 6.3(b). By day, the differences are small due to the large depth over which differences in the surface forcing are spread in unstable conditions. By night, however, the 15 m potential temperature shows little change at short fetches unlike the street surface temperature. Indeed, even at a fetch of 10,000 m the 15 m potential temperature still does not approach that of the equilibrated boundary layer! Only approximately 60% of the difference between the boundary layer profiles over the flat and canyon surfaces occurs by a fetch of 10,000 m. The boundary layer potential temperature is dependent on the bulk surface energy balance and on the advection of the upstream profile. These processes require time to alter the boundary layer profile which introduces a fetch dependence on the urban impact modelled. The adjustment process also affects the surface with 25% of the urban impact on the surface temperature occuring in the adjustment process.

6.3.2 Diurnal cycle of the energy balance

Changes in the boundary layer potential temperature profiles are caused by changes in the bulk surface energy balance. The adjustment of the boundary layer can therefore also be observed in the bulk energy balance. Figure 6.4 shows the diurnal profiles of the bulk sensible heat flux from the five cases considered earlier. The differences between the profiles are small, as the radiative forcing and material properties are the same in all cases, but there are important qualitative differences.

Negative sensible heat fluxes occur around dusk in all five cases. The strong radiative cooling of the surface is sufficient to produce stable boundary layers. The surface cooling of the upstream surface is stronger than that of the canyon surface (the shape factor effect) and, over time with atmospheric mixing, is sufficient to cool the upstream near-surface air temperature below the surface temperature of the canyon surfaces. The advection of this cool near-surface air over the warmer

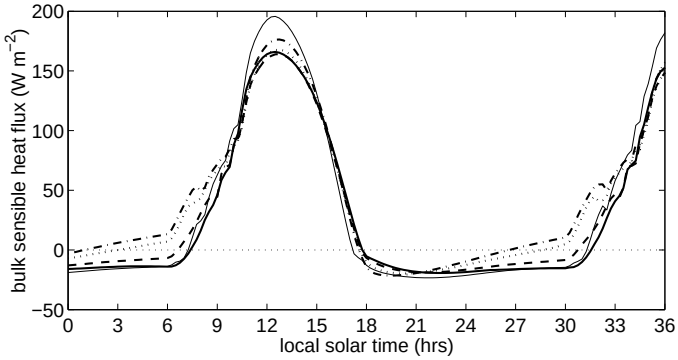

Figure 6.4: Diurnal profiles of the bulk sensible heat flux from the coupled model incorporating advection. Thin solid line, upstream profile; thick solid line, fully adjusted profile; dash-dotted line, profile after 100 m adjustment to the new surface; dotted line, profile after 1,000 m adjustment to the new surface; dashed line, profile after 10,000 m adjustment to the new surface.

canyon facets then triggers positive nocturnal sensible heat fluxes from the canyon surfaces. A positive sensible heat flux acts to cool the surface and warm the boundary layer reducing the magnitude of the sensible heat flux with distance travelled. Therefore the region that releases positive sensible heat flux is restricted to the region of the urban area in the vicinity of the surface change (Figure 6.5).

6.3.3 Adjustment with fetch

There are a range of length scales on which the atmosphere and surface variables respond to a change in the surface type. Knowledge of these length scales is needed when deciding how best to incorporate the adjustment process into numerical weather prediction models. For instance, a rapid adjustment can be incorporated by simply changing the parameter value(s) responsible. However, for a longer adjustment, where the both mean and final effects may be needed, more care needs to be taken. Figure 6.5 shows transects of boundary layer properties across the homogeneous urban area at midnight (thick lines) and at dawn (thin lines) and shows the length scales of adjustment.

Figure 6.5(a) shows transects of the street surface temperature (solid lines) and 15 m potential temperature (dash-dotted lines) with distance from the change in surface type. For reference, the upwind surface temperature at midnight is 277 K and at dawn is 273 K. The upwind 15 m potential temperatures take the same value as at zero fetch. There are two adjustment length scales influencing the change in surface temperature with fetch. Firstly, there is the short (m's to instantaneous) adjustment due to the shape factor effect on the net radiation. Secondly, a longer length scale (10's km) relates to the adjustment of the boundary layer as the wind, turbulence and

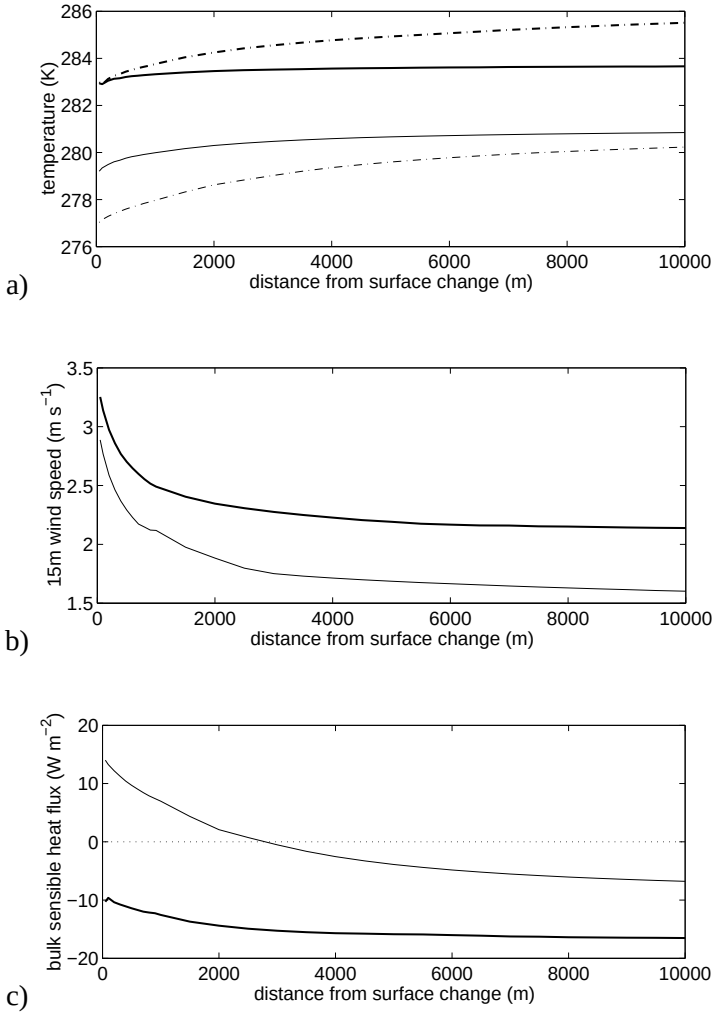

Figure 6.5: Transect of atmospheric variables from the change in surface type. Thick lines, transects at midnight; thin lines, transects at dawn 6 hours later. (a) solid line, street surface temperature; dash-dotted line, 15 m potential temperature; (b) 15 m wind speed; (c) bulk sensible heat flux.

potential temperature profiles adapt to the changing surface energy balance. Within the boundary layer this second length scale dominates.

Figure 6.5(b) shows the transect of the 15 m wind speed. The 15 m wind speed is influenced by two length scales. The first, dominant, length scale (1–2 km) relates to the adjustment to the new bulk roughness length and displacement height. The second length scale relates to the dependence of the mean wind profile on the stability of the boundary layer and hence to the changing surface energy balance.

The surface energy balance is influenced by both the wind speed and the boundary layer potential temperature. Therefore all the length scales for adjustment are present in the transect of the bulk sensible heat flux (Figure 6.5(c)). Note that although the street surface temperature is greater

than the 15 m potential temperature for all fetches considered (Figure 6.5(a)) the bulk sensible heat flux is negative for large fetches due to a larger negative flux into the roof facet (cf. Figure 4.7). The adjustment process within the boundary layer is forced by the changing bulk sensible heat flux. As the bulk sensible heat flux is determined by the surface morphology and surface temperatures (adjusting instantaneously) and the boundary layer wind and potential temperature (adjusting on length scales of 1–2 km's) it is unsurprising that the full adjustment to the new surface type occurs on a range of, and notably long, length scales.

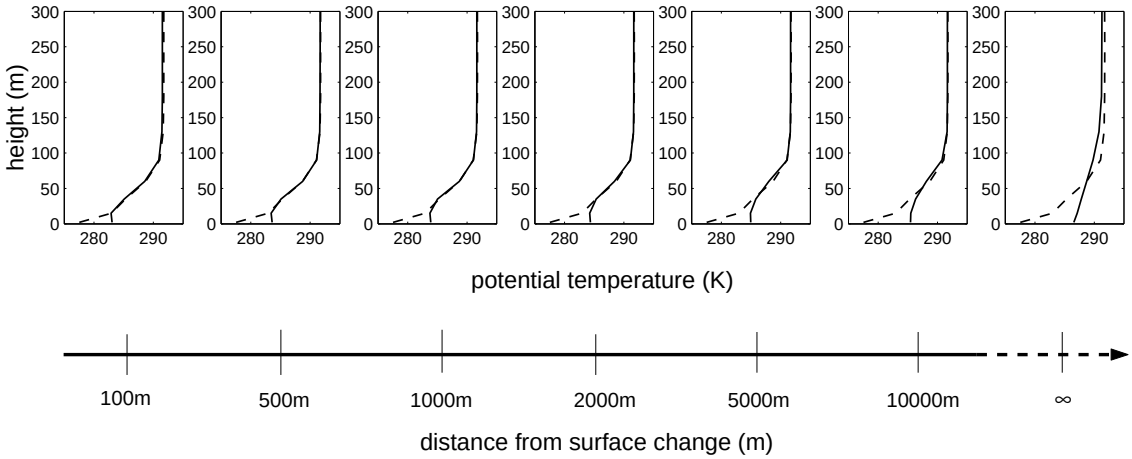

Figure 6.6: Variation of atmospheric profiles with fetch from the surface type change. Boundary layer potential temperature profiles at midnight for various fetches from the change in surface type (solid lines) as indicated by the bottom scale. Dashed line in each panel is the upstream boundary layer profile.

The adjustment of the boundary layer has many characteristics of the growth of a thermal internal boundary layer. Figure 6.6 shows vertical potential temperature profiles at midnight for a range of fetches, L_F. The maintenance of high surface temperatures due the effects of surface geometry on the net radiation acts to retard the cooling of the boundary layer near the surface. Turbulent mixing establishes well mixed, or slightly stable, profiles in the lowest layers of the boundary layer in association with the warmer surface temperatures. This mixing also creates a shallow layer above the well mixed layer which is cooler than the upstream boundary layer. The depth of the atmosphere affected by the change in the surface is clearly determined by the upstream profile and the surface thermal difference. This indicates that in real cities the depth and magnitude of the urban canopy and boundary layer heat islands are intimately linked to the state of the upwind rural boundary layer and determined, in part, by the adjustment processes. These profiles match closely the form, if not quantitatively, the boundary layer profiles observed by Oke and East (1971) over Montréal at dawn. The advection process also gives the similarity of the

urban and rural boundary layer profiles at altitude (Figure 6.6), which was a weakness in the one dimensional model.

The upstream boundary layer profiles in real life will be those of the surrounding rural countryside and not that of a flat, smooth, dry surface. Moisture plays a particularly important role in determining the energy balance and boundary layer profiles in rural areas (e.g. McNaughton and Spriggs, 1986) and will therefore impact on the adjustment of the boundary layer to an urban surface. In rural areas moisture acts to decrease the surface sensible heat flux as well as to decrease the surface and boundary layer temperatures during the day. The advection of this cooler boundary layer over an urban surface will result in larger values of the bulk sensible heat flux by day and night, reduced daytime temperatures and a greater fetch of urban surface generating positive nocturnal sensible heat fluxes when compared to the dry simulations. For instance, an order of magnitude estimate of the impact of incorporating a latent heat flux equal to the sensible heat flux by day and zero at night (a Bowen ratio equal to 1), indicates that this would have the effect of extending the region of positive nocturnal sensible heat fluxes out to 5 km from the change in surface type at dawn. Moisture will also affect the timing of the maximum heat island intensity, which is a weakness in the one dimensional model, through both its direct influence on the reference rural boundary layer and also indirectly through the advection process. A full investigation of the impacts of moisture on the energy balance of urban areas and on the adjustment process remains for future work.

6.4 Summary and implications

This chapter investigated the adjustment of the boundary layer and surface energy balance to an urban area. The advective terms in the boundary layer were incorporated into the coupled canyon energy balance and boundary layer model using a method involving a relaxation to the upstream boundary layer. Coupling the boundary layer modelled over a flat surface to the boundary layer over the canyon energy balance allowed the adjustment of the boundary layer and surface energy balance to the effects of surface morphology to be investigated.

Adjustment was seen to be a key process affecting the surface energy balance, as well as the boundary layer dynamics and thermodynamics of the urban area. At the surface, the urban impact on surface temperature is felt almost immediately through the shape factor effect. In the atmospheric boundary layer the urban impact is felt entirely through the adjustment process. The

interactions between the boundary layer and the energy balance act to provide a further 25% of the urban impact on the surface temperature.

The adjustment processes occur on a range of spatial scales and through a range of physical mechanisms. The shape factor effect on the net radiation and the dynamic adjustment to the increased roughness and displacement occur on short length scales. The thermodynamic adjustment, accomplished through the interactions of the boundary layer and the energy balance, occurs on longer length scales. This combined adjustment process is found here to require over 10 km of uniform surface to become fully equilibrated. A key result is that the adjustment process can allow the generation of positive nocturnal sensible heat fluxes.

There are a range of implications of this simple study. This work has shown that neutral nocturnal boundary layers can be explained by the adjustment process without the need to invoke large anthropogenic heat fluxes. The adjustment process is unlikely to equilibrate in real life as urban areas typically vary their characteristics on much shorter length scales than those shown to be required for full adjustment. Successive adjustments can then realise large regions of urban areas which can release positive nocturnal sensible heat fluxes.

Adjustment on length scales shorter than the grid spacing is difficult to incorporate into numerical weather models. Together with the long length scale required for thermodynamic adjustment this poses problem in determining the morphological properties representative of an urban area. For instance, suppose that within one grid box of a numerical weather prediction model there are two successive changes in urban surface. The adjustment process could then generate two regions of the urban area with positive nocturnal sensible heat fluxes and thus give a positive heat flux for the grid point. With only one representative set of values for the morphological properties of the urban surface, the numerical weather prediction model would be unable to incorporate the successive adjustments without increasing the resolution. Negative nocturnal sensible heat fluxes could then be predicted for the grid point even when incorporating the urban energy balance. Finally, the adjustment process will, in some way, also determine whether each individual urban area is large enough that it needs to be incorporated into numerical weather prediction models.

Advection and the accompanying adjustment processes within the boundary layer have been shown to play an important role in the simple case considered here. It is suggested that advection plays a key role in determining the impact of real urban areas on the local surface energy balance and boundary layer.

CHAPTER SEVEN

Conclusions

7.1 Summary of thesis

Urban areas pose a complex problem for the atmospheric scientist because of the complexity of the surface and the turbulent nature of the planetary boundary layer. Despite large differences in building configuration, for example, between individual urban areas, there are common themes in the observed modifications of the local climate by urban areas. Urban areas are generally warmer, less windy and drier in a relative sense than their rural surroundings, with these differences varying on all time and space scales. The large differences between urban areas make the understanding and prediction of the modifications to the local climate by an urban area difficult primarily because there are a large number of plausible causes.

The characteristic common to all urban areas are buildings. Buildings impose two properties on the surface of an urban area. Firstly, the total surface area is increased from that of a horizontal surface. Secondly, there is necessarily a change in the *geometry* of the surface to accommodate the increase in total surface area. Together these properties comprise the *morphology* of the urban surface. It is suggested that a cause of the modifications to the local climate by urban areas results from the combination of the effects of surface morphology. However, the full impacts of just the surface morphology on the urban climate had not been investigated thoroughly before this study.

Urban areas are surface features and so impose their modifications of the local climate by altering the surface energy balance and wind stress. In doing so the profiles of wind, temperature and humidity in the atmospheric boundary layer are altered. As the surface energy balance itself is determined in part by these profiles, the surface and boundary layer form one coupled system.

The aims of this work were therefore:

- To investigate thoroughly the influence of surface morphology on the individual terms of the surface energy balance of, and boundary layer, over urban areas.
- To establish which of the observed urban modifications of the local climate can be explained by the combined effects of surface morphology and to propose alternative physical mechanisms for those that cannot, and finally
- to establish a method to incorporate urban areas, notably the effects of surface morphology, into numerical weather prediction models.

To address these aims a generic unit of the urban surface, a dry urban street canyon, was used as the basis for a model of the surface energy balance of an urban area. The energy balance of, and boundary layer over, flat surfaces were compared with those over urban street canyon surfaces to investigate the influence of surface morphology on the individual facet-averaged and bulk energy balances, on the surface temperatures and on the profiles of wind and potential temperature in the boundary layer. A range of analytic, experimental and numerical methods were used in this investigation.

The first aim of the work was addressed in Chapters 2 and 3. Chapter 2 and Appendix A considered the effects of canyon geometry on the radiative fluxes. A matrix method (Sparrow and Cess, 1970) to calculate the facet-averaged net radiative flux densities for a street canyon, incorporating multiple reflections of radiation, was presented. This method was compared to two approximate, and commonly used, methods incorporating one reflection of radiation (e.g. Johnson *et al.*, 1991) or no reflections (e.g. Noilhan, 1981) across a wide range of canyon geometries. The effects of canyon geometry on the flux densities and bulk radiation balance were considered as well as the validity of the two approximate methods.

Chapter 3 considered the turbulent transfer within an urban street canyon. A model for the facet-averaged turbulent flux of a scalar, such as heat, from each facet of an urban street canyon was presented. The influence of canyon morphology on the turbulence within the boundary layer above the buildings and within the street canyon was incorporated into the model. Model predictions compared well with observations from Barlow and Belcher (2002) and Barlow *et al.* (2004) and were used to give insight into the important physical processes responsible for the turbulent transfer close to the surface of an urban area. The morphological dependence of the ground heat

flux in an urban area is dependent solely on the surface area and surface temperature variation so was not considered in detail.

Results from Chapters 2 and 3 were used to formulate the urban street canyon energy balance as presented in Chapter 4. The canyon energy balance model was coupled to a one dimensional boundary layer model (Busch *et al.*, 1976) to allow the interactions between the surface and boundary layer that are present in reality (e.g. Brubaker and Entekhabi, 1996; Raupach, 2001) to occur. This coupled model was then used to investigate the dependence of the average energy balances of the canyon facets, of the *bulk energy balance* for the entire canyon unit and of the boundary layer state to surface morphology. Additionally the model was used to determine qualitatively which observations of the urban modification of climate can be explained by surface morphology alone. Chapter 5 addressed the final aim of identifying a method to incorporate urban areas into numerical weather prediction models. The full four facet canyon energy balance was averaged in two ways (two facets - canyon and roof, and only one facet) to assess the degree of complexity needed to capture the effects of the urban street canyon.

Chapter 4 illustrated that some key features of the urban modification of climate, notably positive nocturnal sensible heat fluxes, cannot be explained solely by the effects of surface morphology on the bulk energy balance and boundary layer. Chapter 6 investigated possible causes for this feature, notably the advection of a rural boundary layer over an urban area.

Throughout this work the individual results are related to two concurrent themes - these conclusions will address these themes in turn. Firstly, the increase in surface area and the geometry of the surface influences all parts of the energy balance-boundary layer system. Net changes often result as the residual between opposing changes imposed by the two properties. Secondly, the surface energy balance and boundary layer form one system; one cannot be done without the other. Changes in one part of the system may relate to physical processes acting on a separate part.

7.2 Conclusions

Surface morphology influences the urban energy balance and urban boundary layer by increasing the total area of the surface available for energy exchange and by deforming the surface. The increased total surface area of an urban area reduces the magnitude of the average flux densities of all terms in the energy balance from the horizontal and vertical surfaces given the same external radiative forcing (Sections 2.5, 3.9, 4.4 and 4.8). The diurnal temperature variation at the surface

and near surface is therefore also reduced. However, the increase in total surface area acts to increase the bulk flux of longwave radiation away from the top of the convoluted surface with a corresponding decrease in the bulk sensible and bulk ground heat fluxes (Section 4.4).

Accompanying these changes due to surface area is a range of effects imposed by the geometry of the surface. Firstly, given the same atmospheric and surface temperatures, the bulk radiative and bulk sensible heat fluxes are increased in magnitude. This is despite the flux densities on the individual facets decreasing. This therefore illustrates the competing influences of an increased surface area and surface geometry. Secondly, the incoming longwave radiation for the canyon facets partly originates from the other facets and not the sky. This *shape factor effect* reduces the magnitude of the net longwave radiative flux densities and acts to offset (usually positively) the mean surface temperature. Thirdly, shadowing and the inclination of surfaces results in a non-uniform distribution of shortwave radiation onto the canyon facets. Finally, surface geometry acts to increase the roughness length and displacement height representative of the mean wind in the boundary layer over an urban area which is correspondingly reduced. These processes, notably the reduction in the turbulent flux densities, alter the partitioning of energy into its various forms compared to a horizontal surface and act to change the phases of the fluxes. A roughened surface without surface geometry is unable to reproduce these effects and can give opposite results (Section 4.5).

The boundary layer plays a key role in determining the modifications to the local climate by urban areas. By day, when the differences in the energy balance (i.e. the bulk sensible heat flux) between different cases are large, the increased depth of the boundary layer acts to spread the difference in the surface forcing in the vertical. This, together with the offset in surface temperature due to the shape factor effect, results in small thermal differences in the boundary layer by day. Conversely by night, when the differences in the bulk sensible heat flux between cases are small, the reduced depth of the stable boundary layer allows large thermal differences. This process, in conjunction with the offset in surface temperature due to the shape factor effect, means that the observed diurnal cycle of the surface and near-surface nocturnal urban heat islands (e.g. Oke, 1987) can be explained in terms of surface morphology alone.

Stability effects within the boundary layer act to reinforce the differences between the boundary layers over an urban canyon and flat surface, particularly during the night. The increased roughness and mixing due to geometry act to increase the efficiency of the turbulent transport of heat between the atmosphere and the surface. This mixes the nocturnal atmospheric cooling

through a greater depth of the boundary layer. This in turn reduces the stability of the nocturnal urban boundary layer. A reduction in the stability of the boundary layer increases the turbulent mixing which reinforces the nocturnal thermal differences. The combined effects of surface morphology therefore act to produce warmer, deeper and less stable nocturnal boundary layers over urban areas.

The variation of these effects with canyon geometry qualitatively explains some of the spatial variation in the urban modifications to the local climate. With increasing urbanisation (increasing canyon aspect ratio) the near-surface nocturnal thermal anomalies increase in magnitude as seen in spatial maps of the mean urban heat island (Oke, 1987). As the canyon aspect ratio is increased the canyon bulk energy balance is altered in two ways. Firstly the bulk sensible heat flux is decreased in magnitude with its peak value and the transition to stable conditions delayed (as observed by Grimmond and Oke (2002)). Secondly the bulk ground heat flux is increased in magnitude with its peak value occuring earlier during the day (as observed by Cleugh and Oke (1986)).

The coupled nature of the surface energy balance and boundary layer is highlighted further when explaining positive nocturnal sensible heat fluxes. The advection of a stable (rural) boundary layer over an urban surface was shown (Chapter 6) to be a plausible cause for this characteristic feature of urban areas. A one dimensional coupled model is unable to produce positive nocturnal sensible heat fluxes unless a mechanism is introduced to decouple the boundary layer and surface temperatures. Including the advection process in the boundary layer provides this mechanism and enables positive nocturnal sensible heat fluxes to be generated. The urban boundary layer heat island was seen to take the form of a thermal internal boundary layer (Section 6.3; Oke and East, 1971). When advection is included in the model the surface thermal anomalies are also altered: Only at a fetch of some 20 km are the thermal anomalies equal to the one dimensional simulations. The variation in spatial patterns of the urban heat island (e.g. Graves *et al.*, 2001) can then be interpreted as the variability due to advection of different adjusting boundary layers over the same urban surface. The energy balance, dynamic and thermodynamic impacts of urban areas should therefore be investigated using a coupled boundary layer-surface energy balance model where the full effects of surface morphology have been incorporated. Other features of urban areas (e.g. building material properties) can influence the urban modification of the local climate but play a secondary role.

The geometry of the urban surface allows the energy balances of the different building facets to interact directly. This is a property of the urban surface for which the surface exchange schemes of

most operational weather prediction models are not configured. However, providing the impacts of surface morphology on the radiation, bulk roughness length, bulk displacement height and turbulent transport are kept, the bulk energy balance from the four-facet urban street canyon can be successfully approximated using two facets (Section 5.3). These two facets are an unchanged roof facet and a canyon facet which is the average of the street and two walls weighted by surface area. The bulk energy urban street canyon cannot be successfully approximated across the full range of urban morphologies using only one facet due, primarily to the non-uniformity of the direct solar radiation.

There are a number of caveats to attach to these results. Firstly, the assumption that the energy balance of urban areas can be represented as that from a series of urban street canyons requires investigation. Care needs to be taken when extrapolating from the street canyon studies to real urban areas (see Section 3.7). Masson *et al.* (2002) has shown that an energy balance model based on an urban street canyon gives reasonable predictions of the observed energy balance in a range of locations. However, this work forces the energy balance with observations and therefore does not allow the coupled nature of the system to develop. However, the processes highlighted here (surface area, geometry and the coupled system) apply qualitatively to any array of buildings.

Secondly, urban areas cannot be considered to be dry. Moisture was ignored in this study to reduce the number of processes. Therefore comparisons between the energy balance of, and boundary layer over, the flat and urban canyon surfaces may not be indicative of the differences between urban and rural sites. Moisture is known to play an important role in the energy balance of an urban area during and after rain events (Landsberg, 1981) and there is increasing interest in the role of dew fall in urban areas (e.g. Richards and Oke, 2002). Additionally, moisture will play a significant role in determining the upstream boundary layer when considering the adjustment process (Chapter 6). The coupled nature of the energy balance and boundary layer implies that this will affect, quantitatively at least, the results concerning the generation of positive nocturnal sensible heat fluxes.

Finally, the anthropogenic heat flux in urban areas although commonly small may be sufficient to explain some observations of urban areas. Anthropogenic forcing can influence the surface energy balance directly (e.g. the maintenance of internal building temperatures as done here) or indirectly (e.g. traffic induced turbulence (Rao *et al.*, 2002), or heat emissions directly into the boundary layer (Kannari *et al.*, 2003; Sailor *et al.*, 2003)). These forcings may be important in specific cases (e.g. Ichinose *et al.*, 1999; Spronken-Smith *et al.*, 2003) and in explaining the timing

of transitions between stable and unstable conditions.

7.3 Impact on the wider picture

This work complements and adds to a range of existing work. This work confirms the conclusions from the work of Oke *et al.* (1991) that the principal causes for the urban modification to the local climate arise through surface morphology, with the building material properties (notably the thermal admittance) playing the second role. This work shows that these conclusions hold when the turbulent fluxes and the interactions between the boundary layer and surface energy balance are included.

Other urban energy balance models exist (e.g. Masson, 2000; Kusaka *et al.*, 2001; Grimmond and Oke, 2002; Martilli *et al.*, 2002; Vu *et al.*, 2002) which do not incorporate the dependence of the energy balance on surface morphology to the extent of this study. This work has shown the impact that a few additional processes can have on the model predictions, notably the inclusion of multiple reflections of radiation and the inclusion of turbulent fluxes which depend on the surface morphology and the overlying boundary layer characteristics. While the impact that these processes would have on these models is not immediately obvious, their impact on this work is significant and suggests that the properties of the coupled system (the balance between the increased surface area and geometry on the bulk fluxes for example) should be present in any model of the energy balance of an urban area.

Realisation of the importance of the boundary layer over the urban area in determining the energy balance and the temperature profiles is relatively new to this field. The boundary layer was seen to be a controlling influence on the turbulent fluxes and therefore the surface and near-surface temperatures. Caton *et al.* (2003) observed a similar dependence on the boundary layer turbulent intensity when considering the ventilation of pollutants from a street canyon. The adjustment of the boundary layer as it progresses over an urban area, and in particular the generation of positive nocturnal sensible heat fluxes, is of particular importance in a variety of applications. Future work into the energy balance of urban areas must consider the energy balance and boundary layer together especially when considering the sensitivities of the energy balance.

This work as a whole has confirmed the need for models of the energy balance of an urban area to incorporate surface morphology. Most of the bulk impacts of urban areas on the local climate can be captured using relatively simple methods provided the full range of physical processes

resulting from surface morphology are incorporated in both the energy balance and the boundary layer.

7.4 Future work

This work has developed understanding of the mechanisms acting which determine many of the modifications to the local climate made by urban areas. However, there are a number of avenues which remain to be investigated or which have opened due to this work.

Application of the naphthalene sublimation technique for measuring the facet-averaged turbulent fluxes can be extended in two ways. Firstly, alternative two dimensional geometries could be used to validate the model developed in Chapter 3 and for alternative canyon orientations. Secondly, the technique could be applied to a three dimensional array of buildings. This second use would allow an assessment of the differences between two and three dimensional geometries and indicate whether the urban street canyon should be used as a generic unit of an urban area. This broader aim could also be investigated by extending the radiative transfer model (Chapter 2) to three dimensions and comparing the results to the existing two dimensional calculations.

Moisture in the urban energy balance is a key issue to address. In an operational setting, where representative surface types for the grid points are required, this could be achieved by allowing a dry urban surface but reducing the fractional area occupied by the urban surface surrounding each grid point. This method may not, however, succeed during and after rain events. An alternative method is to incorporate a shallow pond model on the street and roof facets as part of the street canyon energy balance.

The specification of input parameters for real urban areas will require care. Using the urban street canyon as the generic unit of the urban surface implies that the geometric ratios h_e/w_e and w_e/r_e be related in some fashion to the real urban morphology. The surface roughness length, displacement height, radiative fluxes and turbulent fluxes all depend on the characteristic ratios in different non-linear ways. There is therefore a difficulty in the specification of the urban canyon parameters which preserves all of these properties of urban areas. A related problem is that within numerical weather prediction models these input parameters will be representative of the area surrounding the grid point. However, in real urban areas the characteristic ratios vary on length scales smaller than the numerical weather prediction models' grid-point separation. It is not immediately obvious how these input parameters should be chosen in order to preserve the mean bulk energy

balance.

The individual terms of the energy balance model developed here have been compared to either existing methods or new data. However, the full energy balance model remains to be validated. Such a validation would require the careful consideration of a number of points. For instance, can observations be made of the modelled variables e.g. facet-averaged energy balances? Additionally should one attempt to validate the entire boundary layer-surface energy balance model or just the surface component?

A final section of future work is the implementation of an urban energy balance into an operational numerical weather prediction model. Chapter 4 illustrated the properties that such a scheme should possess and Chapter 5 a possible method to do this. Once implemented, and questions over the input parameters have been overcome, several questions can be addressed. Firstly, is there an improvement of the forecast of local properties, e.g. the street surface temperature? Secondly, is there an improvement in the forecast at larger (city or regional) scales? Finally, is there evidence of urban areas influencing mesoscale or synoptic scale weather features? A related but separate issue is the relation of this work to canopy models. These models have been applied to incorporate vegetation and urban areas (e.g. Best, 1998a) into numerical weather prediction models. This approach has been successfully used to predict the spatially averaged mean winds through urban areas (Belcher *et al.*, 2003; Coceal and Belcher, 2004) and progress has been made towards incorporating surface morphology into the energy balance for an urban canopy (e.g. Vu *et al.*, 2002). A common method to deal with both the dynamic and thermodynamic aspects of the influence of any surface type on the boundary layer within numerical weather prediction models may therefore be possible.

APPENDIX A

Solar radiation in an urban street canyon

Solar radiation on arbitrary surfaces

The wavelength-integrated shortwave radiative flux density, or insolation, received at the top of the atmosphere, K_{toa}, is primarily determined by the position of the Earth relative to the Sun and solar activity. The insolation received at the Earth's surface additionally depends on the latitude, time of day, elevation and orientation of the surface as well as radiative processes within the atmosphere. Both the direct and diffuse components of the solar radiative flux density for an arbitrarily inclined and oriented surface are needed to provide a solar forcing for the surface energy balances described in Chapter 4.

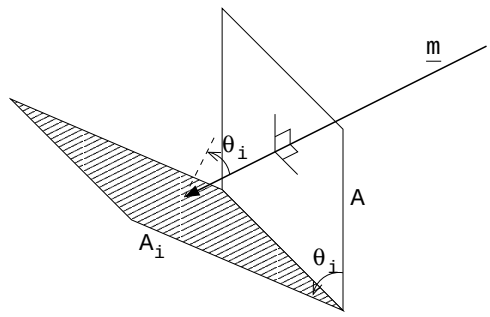

Figure A.1: Relative surface area for a surface oriented to a solar ray.

Consider first the geometric dependency of the direct solar radiative flux density that results from the variation in the direction of the sun's rays. Define the solar incidence angle, θ_i, to be the angle between the normal to the surface and the sun's rays and denote the direct solar radiative flux density onto a surface normal to the sun's rays as $K_\perp$ (i.e. incorporating atmospheric radiative effects but no geometric effects) as shown in Figure A.1. For a horizontal surface the solar incidence angle is equivalent to the solar zenith angle, θ. As the surface need not be normal to the

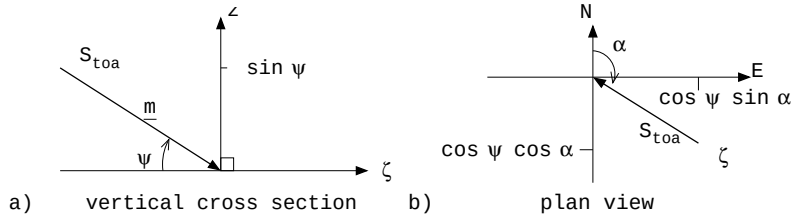

Figure A.2: Schematic of the unit vector aligned with a solar ray; (a) elevation; (b) orientation.

sun's rays the surface area, A_i, onto which the solar flux impinges is increased through a geometric factor given by

$$A = A_i \cos\theta_i, \tag{A.1}$$

and hence the flux density onto the surface, K_{sf}, is decreased to ensure conservation of energy to

$$K_{sf} = K_{\perp} \cos\theta_i. \tag{A.2}$$

The angle between any two vectors, $\underline{m}$ and $\underline{n}$, and hence between the normal to a plane and a line, can be calculated using the scalar product ($\underline{m} \cdot \underline{n} = |\underline{m}||\underline{n}| \cos\theta_i$). The geometric dependency of the direct component of the solar radiative flux density for an arbitrary surface can therefore be determined by calculating the unit vectors of the normal to the surface and of the sun's rays (e.g. Owczarek, 1997). For convenience these are expressed in terms of latitude, ϕ, Julian day number, d_n, and time of day, $h(t)$.

Consider first the vector describing the direction of the solar rays in a cartesian system at the Earth's surface aligned with the z-axis pointing vertically upwards, the x-axis pointing due east and the y-axis pointing due north. The solar rays will impinge on the surface with an elevation angle, ψ, and azimuthal angle, α, as shown in Figure A.2.

The unit vector for the solar ray in terms of the elevation angle and azimuthal angle is:

$$\underline{m} = \begin{bmatrix} \cos\psi(t)\sin\alpha(t) \\ \cos\psi(t)\cos\alpha(t) \\ \sin\psi(t) \end{bmatrix}. \tag{A.3}$$

Spherical geometry (Owczarek, 1997) gives that the vector $\underline{m}$ can be written in terms of the latitude, ϕ, solar declination angle, δ, and time of day, $h(t)$, using the following identities,

$$\cos\psi(t)\sin\alpha(t) = \cos\delta(d_n)\sin h(t), \tag{A.4}$$

$$\cos\psi(t)\cos\alpha(t) = -\sin\delta(d_n)\cos\phi + \cos\delta(d_n)\sin\phi\cos h(t), \tag{A.5}$$

$$\sin\psi(t) = \sin\delta(d_n)\sin\phi + \cos\delta(d_n)\cos\phi\cos h(t). \tag{A.6}$$

The declination angle, δ, measures the tilt of the Earth's rotational axis relative to its orbital plane and can be determined from the Julian day number, d_n, through Equation (A.7). The time of day, $h(t)$, is measured as the fraction of the day (in radians) with local noon being zero; the relationship to the local solar time, t, is given by Equation (A.8).

$$\delta(d_n) = 0.4102\cos\left[\frac{2\pi(d_n - 172)}{365}\right], \tag{A.7}$$

$$h(t) = 2\pi\frac{t-12}{24}. \tag{A.8}$$

The unit vector describing the direction of the solar ray is therefore

$$\underline{m} = \begin{bmatrix} \cos\delta\sin h(t) \\ -\sin\delta\cos\phi + \cos\delta\sin\phi\cos h(t) \\ \sin\delta\sin\phi + \cos\delta\cos\phi\cos h(t) \end{bmatrix}. \tag{A.9}$$

Consider now the unit vector normal to a planar surface with elevation angle β to the horizontal and orientation angle Ω from the north in the same cartesian coordinates as shown in Figure A.3.

The unit vector $\underline{\mathrm{n}}$ is found to be

$$\underline{n} = \begin{bmatrix} \sin\beta\sin\Omega \\ \sin\beta\cos\Omega \\ \cos\beta \end{bmatrix}. \tag{A.10}$$

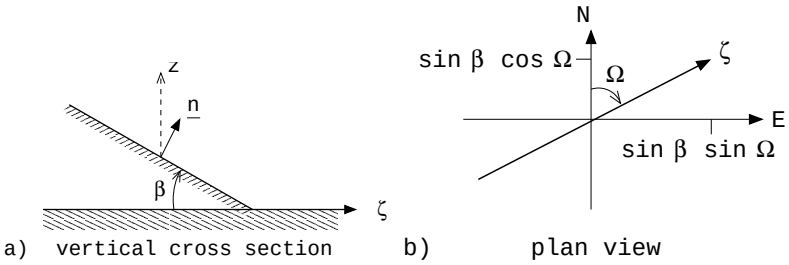

Figure A.3: Schematic of the unit vector normal to an arbitrary surface; (a) elevation; (b) orientation.

The cosine of the incidence angle θ is therefore:

$$\cos\theta_i = \underline{m} \cdot \underline{n} = a_1(\phi,\delta,\beta,\Omega) + a_2(\phi,\delta,\beta,\Omega)\cos h(t) + a_3(\phi,\delta,\beta,\Omega)\sin h(t), \quad \text{(A.11)}$$

$$\text{where } a_1 = \sin\delta(\sin\phi\cos\beta - \cos\phi\sin\beta\cos\Omega), \quad \text{(A.12)}$$

$$a_2 = \cos\delta(\cos\phi\cos\beta + \sin\phi\sin\beta\cos\Omega), \quad \text{(A.13)}$$

$$\& \; a_3 = \cos\delta\sin\beta\sin\Omega. \quad \text{(A.14)}$$

Note that for a horizontal surface, $\beta = 0$, then as expected

$$\cos\theta = \sin\delta\sin\phi + \cos\delta\cos\phi\cos h(t). \quad \text{(A.15)}$$

A final condition is that the solar flux density for any surface cannot be negative i.e. $\cos\theta_i < 0$ in Equation (A.2) cannot happen.

Radiative processes within the atmosphere and diffuse radiation

Geometry also effects the fraction of radiation which is scattered and absorbed by the overlying atmosphere. Scattering and absorption are both processes which are determined by the path length of the sun's rays' passage through the atmosphere. These processes can be captured simply through the optical depth of the atmosphere, τ_a, defined as

$$K_\perp / K_{toa} = \exp\left\{-\tau_a \sec\theta\right\}, \quad \text{(A.16)}$$

where the surface receiving the radiation is at ground level and the $\sec\theta$ term represents the path length dependence of scattering and absorption of radiation through the atmosphere. The optical depth of the atmosphere is heavily dependent on atmospheric constituents, cloud amounts and their properties. For the simple purposes of determining a solar forcing the optical depth is taken as a constant (= 0.2) throughout this work.

The diffuse solar flux density at the surface, K_{df}, is determined through a complex processes of multiple scattering and refraction. For the simple purposes of determining a forcing for the surface energy balance, the diffuse solar radiation impinging a horizontal surface and ground level is taken as a constant fraction (= 0.7) of the radiation which has been absorbed or scattered by the atmosphere, namely

$$K_{df} = 0.7K_{toa}(1 - \exp\{-\tau_a \sec\theta\}). \tag{A.17}$$

Shadowing

The directional nature of the direct component of the solar radiative flux density in conjunction with a system of surfaces at different elevation angles and/or orientations can lead to the shadowing of one surface by another. The individual facets of an urban canyon experience shadowing by another facet at some point in the day in almost all circumstances. A shadowed facet will receive no direct solar radiation but its full quota of diffuse radiation as described in Chapter 2. The urban canyon energy balance model considers facet-averaged flux densities; therefore, for consistency, a partly shadowed facet is deemed to receive a direct radiative flux density equivalent to the area-weighted average of the shadowed and unshadowed fractions of the facet. The fraction of each facet shadowed at any one time is a function of latitude, ϕ, solar declination angle, δ, canyon aspect ratio, h_e/w_e, and canyon orientation, Ω.

Consider a cartesian set of axis where the z-axis points vertically upwards, the x-axis points normally across the street canyon and the y-axis points along the canyon. The y-axis is therefore aligned at an angle Ω to north-south. Consider first the shadow cast by a pole of height h_e placed at the origin. The solar azimuth angle, A_z, is the angle between the shadow cast on a horizontal plane and due south as shown in Figure A.4. Sakakibara (1996) shows that the solar azimuthal

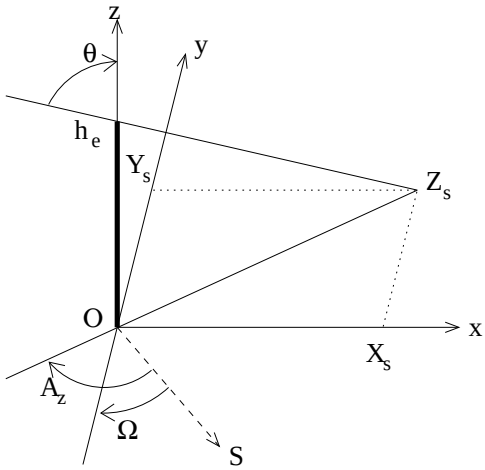

Figure A.4: Schematic of the shadow cast by a pole of height h_e in the canyon relative axes.

angle is related to the location of the pole through the following relations,

$$\cos A_z = (\cos\delta \sin\phi \cos h(t) - \sin\delta \cos\phi) / \sin\theta \ , \tag{A.18}$$

$$\sin A_z = \sin h(t) \cos\delta / \sin\theta \ , \tag{A.19}$$

$$\text{where } \cos\theta = \sin\phi \sin\delta + \cos\phi \cos\delta \cos h(t), \tag{A.20}$$

and θ is the solar zenith angle.

Let X_s, and Y_s denote the position of the end of the shadow cast on the horizontal plane in the x- and y- directions respectively. Trigonometry gives that these positions are,

$$X_s = h_e \tan\theta \sin(A_z - \Omega), \tag{A.21}$$

$$Y_s = h_e \tan\theta \cos(A_z - \Omega). \tag{A.22}$$

The fraction of each facet of an urban canyon shadowed is determined by placing the pole in Figure A.4 at the same x location as either wall of the canyon. The shadow cast by the wall will have the same cross-canyon dimension as that of a pole of the same height. However the shadow cast by the wall will have no along canyon variation due to the two dimensional nature of the urban street canyon. Figure A.5 shows a schematic of the shadowing occuring from the left hand wall for two canyons (superimposed) and the nomenclature used. For the wide canyon, $w_e = w_2$, the

opposing wall is unshadowed and the fraction of the street shadowed, $\zeta = X_s/w_2$, remains to be calculated. For the narrow canyon, $w_e = w_1$, the entire street is shadowed and it is the fraction of the opposing wall that is shadowed, $\eta = h_s/h_e$, that remains to be calculated.

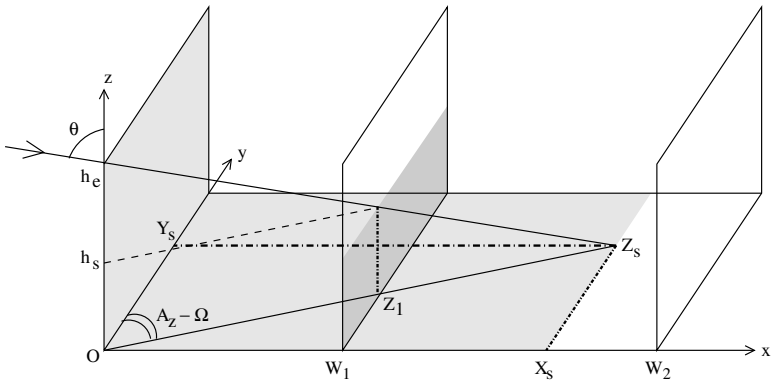

Figure A.5: Schematic of the shadowing occuring in a narrow street canyon (left-most two vertical facets) and a wide street canyon (outer two vertical facets), together with the nomenclature used.

Geometry of triangles gives that

$$\frac{h_s}{Z_s - Z_1} = \frac{h_e}{Z_s}, \tag{A.23}$$

$$\frac{w_1}{X_s} = \frac{Z_1}{Z_s}, \tag{A.24}$$

$$\Rightarrow \frac{h_s}{h_e} = 1 - \frac{w_1}{X_s}. \tag{A.25}$$

$$\tag{A.26}$$

The fractions of the canyon facets in shade can be expressed in terms of the canyon's locations using the identity (A.27) resulting from expanding Equations (A.21) and (A.22),

$$\begin{aligned} \frac{X_s}{w_1} &= \frac{h_e}{w_1} \tan\theta \sin(A_z - \Omega), \\ &= \frac{h_e}{w_1} \frac{\sin h(t) \cos\delta \cos\Omega + \sin\delta \cos\phi - \cos\delta \sin\phi \cos h(t)}{\cos\theta}, \end{aligned} \tag{A.27}$$

The fraction of the street facet of the canyon under shadow, ζ, at any time and location is therefore,

$$\zeta = \begin{cases} \max\left[\frac{|X_s|}{w_e}, 1\right] & \text{if } \cos\theta > 0, \\ 1 & \text{else,} \end{cases} \tag{A.28}$$

where the modulus sign takes into account shadowing from either wall. The fraction of the wall facet of the canyon under shadow, η, at any time and location is therefore,

$$\eta = \begin{cases} 1 & \text{if } \cos\theta < 0, \\ 1 & \text{if } \cos\theta \geq 0 \text{ and } \cos\theta_i < 0, \\ \max\left[1 - \frac{w_e}{X_s}, 0\right] & \text{else ,} \end{cases} \tag{A.29}$$

The conditions on the solar zenith angle and solar incidence angle ensure that firstly negative shadowing cannot occur and secondly that full shadowing occurs during nighttime and when the surface considered does not receive direct solar radiation due to its orientation.

Figure A.6 shows example calculations of the diurnal cycle of unshadowed direct solar forcings (a) and the fractions of the wall and street facets shadowed in an urban street canyon. The case considered is of a street canyon located at 60°N on the spring equinox, oriented at 45° from due north and for canyon aspect ratios of $h_e/w_e = 0.25$, 0.5, 1.0 and 2.0. The orientation of the canyon determines the asymmetry in both the direct solar forcing and the fraction of each facet shadowed. Only one of the two walls can receive direct solar radiation at any one time as seen in the sharp transition to/from shadowed conditions just before 15:00 hours local solar time. Increasing the canyon aspect ratio necessarily increases the fraction of the facets shadowed (to conserve to energy). The diffuse radiative flux (solid line in Figure A.6) is the dominant term in the early morning and late evening. This is due to the path length dependence of the scattering of radiation with the path length of the sun's rays being greatest at these times.

The solar radiative forcings used in the surface energy balance models are calculated by first calculating the unshadowed direct radiative forcings together with the fraction of each facet in shade to find the facet-averaged direct solar radiative forcing. To this is added the appropriate shape-factor weighted (see Chapter 2) contribution of diffuse radiation and finally the effects of multiple reflections for non-blackbody materials are added.

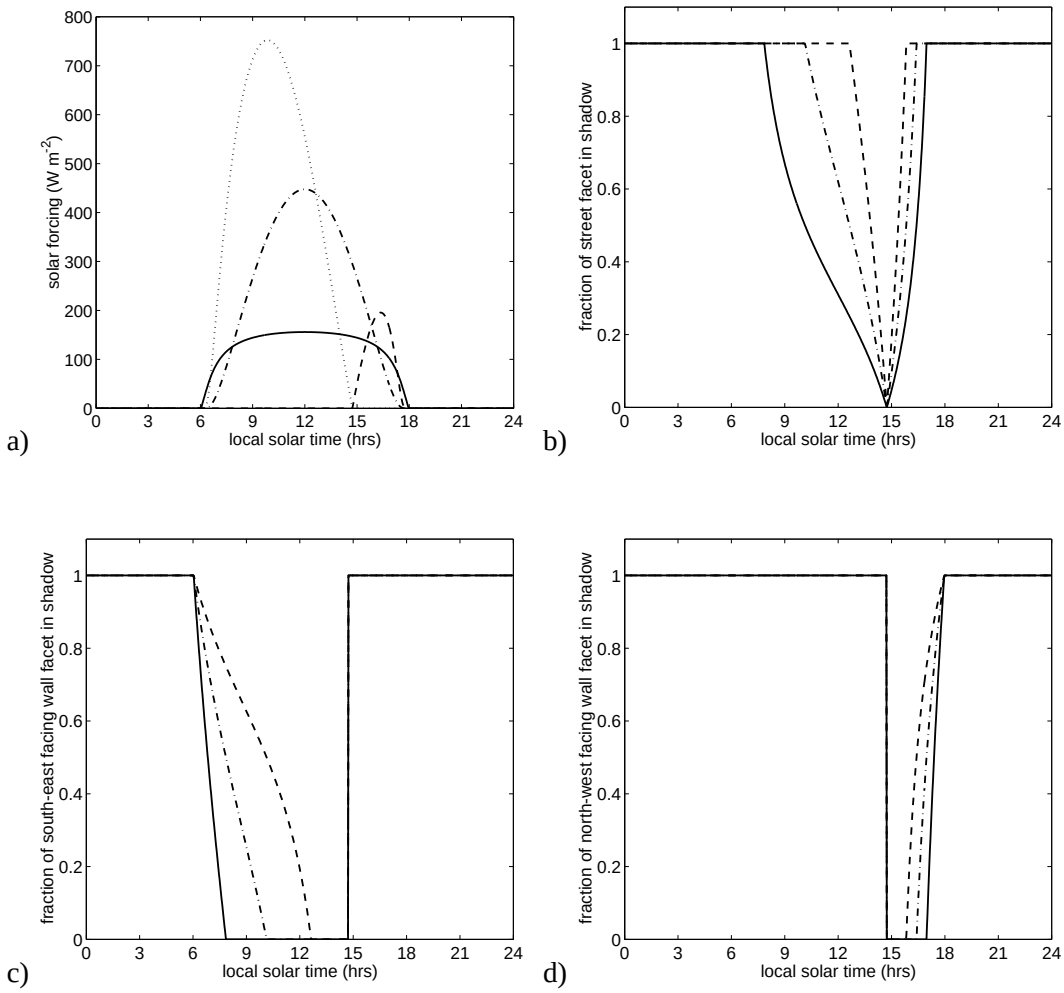

Figure A.6: Sample clear sky radiative forcings and shadows for the different facets of an urban street canyon oriented at 45° from north at 60°N on the spring equinox. (a) Solar radiative forcings; solid line, diffuse radiation onto horizontal surface; dotted line, direct radiation onto an unshadowed southeast facing wall; dashed line direct radiation onto an unshadowed northwest facing wall; dash-dotted line direct radiation onto an unshadowed horizontal surface; (b) shadowing for the street facet of the urban street canyon for a range of canyon aspect ratios; solid line, $h_e/w_e = 0.25$; dash-dotted line, $h_e/w_e = 0.5$; dashed line, $h_e/w_e = 1.0$; dotted line, $h_e/w_e = 2.0$; (c) as (b) but for the southeast facing wall; (d) as (b) but for the northwest facing wall.

APPENDIX B

Turbulence closure in the boundary layer

Studies of the atmospheric boundary layer face the turbulence closure problem, namely that the time-averaged prognostic equations for the state of the atmosphere always include unknown terms. For instance, the evolution of the mean state of the atmosphere is dependent on the vertical divergence of the turbulent fluxes of momentum and heat (Equations (4.17)–(4.19)). These unknown terms require parameterization in terms of known variables. The parameterization of the turbulent terms in the boundary layer model used in Chapters 4, 5 and 6 is that of Busch *et al.* (1976); a brief outline of this method is presented here.

The surface layer

The lower boundary conditions required when modelling the planetary boundary layer are the specification of the turbulent fluxes at the surface and hence the relation between the atmospheric and surface variables. Within the surface layer of the boundary layer, which comprises the roughness sub-layer and the inertial sub-layer, the atmosphere is assumed to be in equilibrium with the underlying surface. The vertical fluxes of momentum and heat are assumed to be constant with height. For a horizontal homogeneous surface, such as the flat surfaces considered in Chapter 4, Monin-Obukhov Similarity Theory (MOST) can be used to determine the spatially averaged vertical profiles of the wind, potential temperature and the surface fluxes of heat and momentum. The mean wind speed, $\bar{\mathbf{v}}(z)$, and potential temperature, $\bar{\theta}(z)$ are accordingly given as

$$|\bar{\mathbf{v}}(z)| = \frac{u_*}{\kappa}\left[\ln\left(\frac{z}{z_{0m}}\right) - \Psi_m\left(\frac{z}{L}\right)\right], \tag{B.1}$$

$$\bar{\theta}(z) - \theta_s = \frac{\theta_*}{\kappa}\left[\ln\left(\frac{z}{z_{0h}}\right) - \Psi_h\left(\frac{z}{L}\right)\right], \tag{B.2}$$

where $u_* = (\tau/\rho)^{1/2}$ is the friction velocity, θ_s is the surface temperature, $\theta_* = -H/\rho c_p u_*$ is a scaling for the instantaneous deviations of θ from its mean value, κ is the von Kármán constant and z_{0m} and z_{0h} are the surface roughness lengths for momentum and heat respectively. L is the Monin-Obukhov length defined as

$$L = -\frac{u_*^3}{\kappa\,(g/\theta_s)\,(H/\rho c_p)}, \tag{B.3}$$

where Ψ_m and Ψ_h are the integrals of the universal functions ϕ_m and ϕ_h (Dyer, 1967) which represent the effects of stability on turbulent mixing. The Beljaars and Holtslag (1991) forms for these functions used to prevent the unrealistic total suppression of turbulent mixing in stable conditions. The turbulent fluxes into the lowest layer of the atmosphere are then given by

$$\overline{u'w'} = -u_*^2 \left|\frac{\partial u}{\partial z}\right| \Big/ \left|\frac{\partial \mathbf{v}}{\partial z}\right|, \tag{B.4}$$

$$\overline{v'w'} = -u_*^2 \left|\frac{\partial v}{\partial z}\right| \Big/ \left|\frac{\partial \mathbf{v}}{\partial z}\right|, \tag{B.5}$$

$$\overline{w'\theta'} = H/\rho c_p. \tag{B.6}$$

Given a surface temperature, the mean wind and potential temperature at a reference height in the inertial sub-layer together with the surface roughness lengths for momentum and heat, Equations (B.1)–(B.3) can be solved iteratively to determine the surface fluxes.

For a complex surface, such as the urban street canyon, Equations (B.1)–(B.6) are replaced by equivalent conditions expressed in terms of a resistance network as introduced in Chapter 3.

The mixed layer

Above the surface layer, the turbulent fluxes vary with height. The turbulent fluxes are parameterized in terms of the mean atmospheric profiles using the turbulent diffusivity method (Equations

(4.20)–(4.22)), namely

$$\overline{u'w'} = -K_m \frac{\partial \overline{u}}{\partial z}, \tag{4.20}$$

$$\overline{v'w'} = -K_m \frac{\partial \overline{v}}{\partial z}, \tag{4.21}$$

$$\overline{\theta'w'} = -K_h \frac{\partial \overline{\theta}}{\partial z}, \tag{4.22}$$

where K_m and K_h are the turbulent diffusivities for momentum and heat respectively.

The turbulent diffusivities are determined using a mixing length approach. Assuming horizontal homogeneity, time independence and that the divergence of the vertical flux of turbulent kinetic energy is small, the turbulent kinetic energy equation gives (Busch *et al.*, 1976)

$$K_m = \lambda^2 \left[\left| \frac{\partial \mathbf{v}}{\partial z} \right|^2 - \frac{g}{\theta_s} \frac{\partial \theta}{\partial z} \right]^{1/2}. \tag{B.7}$$

The mixing length λ is dependent on the history of the flow, is height dependent and has the following properties. In unstable conditions turbulent mixing acts through the depth of the boundary layer and uniform vertical profiles of wind and potential temperature are established requiring λ to be high. In stable conditions, buoyancy effects suppress turbulent mixing requiring λ to be small. Finally near barriers to turbulent mixing, namely the surface or top of the boundary layer, the turbulent mixing is inhibited and the mixing length is reduced. The mixing length λ is determined from the prognostic equation

$$\frac{\partial \lambda(z)}{\partial t} = \frac{\lambda_e - \lambda}{\lambda/(u_*^2 + w_*^2)^{1/2}}. \tag{B.8}$$

Physically this states that the mixing length changes to adapt to the current surface forcing by relaxing towards the mixing length which would be in equilibrium with that forcing λ_e. The time scale on which this change occurs is inversely proportional to the strength of the current mixing as characterised by the *local* friction velocity u_* and the convective velocity w_*. These properties

of the flow are given by

$$u_*^2 = \lambda^2 \left| \frac{\partial \mathbf{v}}{\partial z} \right|^2, \tag{B.9}$$

$$w_* = \left(\frac{g}{\theta_s} \frac{H}{\rho c_p} h \right)^{1/3}, \tag{B.10}$$

$$\lambda_e = \begin{cases} \frac{\kappa z}{\phi_m} \left(1 - \frac{z}{h}\right) & \text{for } z \leq h', \\ \lambda_B & \text{for } z > h', \end{cases} \tag{B.11}$$

where h' is the height where the minimum bound on the mixing length $\lambda_B = 3$m is reached. $h(\approx h')$ is the height of the boundary layer given as the first height above the ground where the local Richardson number

$$R_i = \frac{g}{\theta} \frac{\partial \theta}{\partial z} \Big/ \left| \frac{\partial \mathbf{v}}{\partial z} \right|^2, \tag{B.12}$$

exceeds a critical value of $1/4$.

Finally the turbulent diffusivity for heat, K_h, is determined from Businger *et al.* (1971) as

$$K_h = K_m \, \phi_m / \phi_h, \tag{B.13}$$

and the prognostic equation for $\bar{\theta}(z)$ (Equation (4.19)) is adapted to allow for counter-gradient fluxes in light wind, low stability conditions (Deardorff, 1966) to

$$\frac{\partial \bar{\theta}}{\partial t} = \frac{1}{\rho} \frac{\partial}{\partial z} \left(\rho K_h \left[\frac{\partial \bar{\theta}}{\partial z} - \gamma_c \right] \right), \tag{B.14}$$

with $\gamma_c = 0.7 \times 10^{-3}$ K m $^{-1}$.

References

Abaramowitz, M. and Stegun, I. A., editors (1973). *Handbook of mathematical functions*. Dover Publications, 9th edition edition.

Aida, M. (1982). Urban albedo as a function of the urban structure - a model experiment. *Boundary-Layer Meteorology*, **23**, 405–413.

Aida, M. and Gotoh, K. (1982). Urban albedo as a function of the urban structure - a two-dimensional numerical simulation. *Boundary-Layer Meteorology*, **23**, 415–424.

Arnfield, A. J. (1982). An approach to the estimation of the surface radiative properties and radiation budgets of cities. *Physical Geography*, **3**(2), 97–122.

Arnfield, A. J. (1990). Canyon geometry, the urban fabric and nocturnal cooling: A simulation approach. *Physical Geography*, **11**(3), 220–239.

Arnfield, A. J. (2000). A simple model of urban canyon energy budget and its validation. *Physical Geography*, **21**(4), 305–326.

Arnfield, A. J. (2003). Two decades of urban climate research: A review of turbulence, exchanges of energy and water, and the urban heat island. *International Journal of Climatology*, **23**, 1–26.

Arnfield, A. J. and Grimmond, C. S. B. (1998). An urban canyon energy budget model and its application to urban storage heat flux modeling. *Energy and Buildings*, **27**, 61–68.

Atkinson, B. W. (1985). *U:P:D:A:T:E The Urban Atmosphere*. Cambridge University Press.

Baik, J.-J. and Kim, J.-J. (1999). A numerical study of flow and pollutant characteristics in urban street canyons. *Journal of Applied Meteorology*, **38**, 1576–1589.

Baik, J.-J., Park, R.-S., Chun, H.-Y., and Kim, J.-J. (2000). A laboratory model of urban street-canyon flows. *Journal of Applied Meteorology*, **39**(9), 1592–1600.

Barlow, J. F. and Belcher, S. E. (2002). A windtunnel model for quantifying fluxes in the urban boundary layer. *Boundary-Layer Meteorology*, **104**, 131–150.

Barlow, J. F., Harman, I. N., and Belcher, S. E. (2004). Scalar fluxes from urban street canyons. Part I: Laboratory simulation. *Boundary-Layer Meteorology*, In Press.

Bärring, L., Mattsson, J. O., and Lindqvist, S. (1985). Canyon geometry, street temperatures and urban heat island in Malmö, Sweden. *Journal of Climatology*, **5**, 433–444.

Belcher, S. E., Xu, D. P., and Hunt, J. C. R. (1990). The response of a turbulent boundary layer to arbitrarily distributed two-dimensional roughness changes. *Quarterly Journal of the Royal Meteorological Society*, **116**, 611–635.

Belcher, S. E., Jerram, N., and Hunt, J. C. R. (2003). Adjustment of a turbulent boundary layer to a canopy of roughness elements. *Journal of Fluid Mechanics*, **488**, 369–398.

Beljaars, A. C. M. and Holtslag, A. A. M. (1991). Flux parameterization over land surfaces for atmospheric models. *Journal of Applied Meteorology*, **30**, 327–341.

Bentham, T. and Britter, R. (2003). Spatially averaged flow within obstacle arrays. *Atmospheric Environment*, **37**, 2037–2043.

Best, M. (1998a). Representing urban areas in numerical weather prediction models. In *Proceedings of the 2nd Urban Environment Symposium*, pages 148–151. American Meteorological Society.

Best, M. (1999). Can we represent urban areas in operational numerical weather prediction models? In *Proceedings of the Third Urban Environment Symposium*, pages 70–71. American Meteorological Society.

Best, M. J. (1998b). A model to predict surface temperatures. *Boundary-Layer Meteorology*, **88**, 279–306.

Bornstein, R. and Lin, Q. (2000). Urban heat islands and summertime convective thunderstorms in Atlanta: three case studies. *Atmospheric Environment*, **34**, 507–516.

Bornstein, R. D. (1975). The two-dimensional URBMET urban boundary layer model. *Journal of Applied Meteorology*, **14**, 1459–1477.

Bornstein, R. D. and Thompson, W. T. (1981). Effects of frictionally retarded sea breeze and synoptic frontal passages on sulfur dioxide concentrations in New York City. *Journal of Applied Meteorology*, **20**(8), 843–858.

Bottema, M. (1996). Roughness parameters over regular rough surfaces: Experimental requirements and model design. *Journal of Wind Engineering and Industrial Aerodynamics*, **64**, 249–265.

Bristow, K. L. (1987). On solving the surface energy balance equation for surface temperature. *Agricultural and Forest Meteorology*, **39**, 49–54.

Britter, R. and Hanna, S. R. (2003). Flow and dispersion in urban areas. *Annual Review of Fluid Mechanics*, **35**, 469–496.

Brown, M. J., Lawson, R. E., Decroix, D. S., and Lee, R. L. (2000). Mean flow and turbulence measurements around a 2-D array of buildings in a wind tunnnel. In *Proceedings of the 11th Joint AMS/AWMA conference on the applications of air pollution, Long Beach, CA*.

Brubaker, K. L. and Entekhabi, D. (1995). An analytic approach to modeling land-atmosphere interaction 1. Construct and equilibrium behaviour. *Water Resources Research*, **31**(3), 619–632.

Brubaker, K. L. and Entekhabi, D. (1996). Analysis of feedback mechanisms in land-atmosphere interaction. *Water Resources Research*, **32**(5), 1343–1357.

Busch, N. E., Chang, S. C., and Anthes, R. A. (1976). A multi-level model of the planetary boundary layer suitable for use with mescoscale dynamic models. *Journal of Applied Meteorology*, **15**(9), 909–919.

Businger, J. A., Wyngaard, J. C., Izumi, Y., and Bradley, E. F. (1971). Flux-profile relationships in the atmospheric surface layer. *Journal of the Atmospheric Sciences*, **28**, 181–189.

Carlson, T. N. and Boland, F. E. (1978). Analysis of urban-rural canopy using a surface heat flux/temperature model. *Journal of Applied Meteorology*, **17**, 998–1013.

Castro, I. P. and Robins, A. G. (1977). The flow around a surface-mounted cube in uniform and turbulent streams. *Journal of Fluid Mechanics*, **79**(2), 307–335.

Caton, F., Britter, R. E., and Dalziel, S. (2003). Dispersion mechanisms in a street canyon. *Atmospheric Environment*, **37**, 693–702.

Cheng, H. and Castro, I. P. (2002). Near wall flow over an urban-like roughness. *Boundary-Layer Meteorology*, **104**, 229–259.

Christen, A., Bernhofer, C., Parlow, E., Rotach, M. W., and Vogt, R. (2003). Paritioning of turbulent fluxes over different urban surfaces. In *Proceedings of the Fifth International Conference on Urban Climate, Łódź, Poland.*

Clark, P. A. and Hopwood, W. P. (2001). One-dimensional site-specific forecasting of radiation fog. Part II: Impact of site observations. *Meteorological Applications*, **8**, 287–296.

Clark, P. A., Hopwood, W. P., Best, M. J., Dunlop, C. C., and Maisey, P. E. (1997). Assessment of the first version of the Site Specific Forecasting Model. Forecasting Research Division Technical Report 213, Met Office.

Clarke, J. A. (1985). *Energy simulation in building design*. Adam Hilger Ltd.

Cleugh, H. A. and Oke, T. R. (1986). Suburban-rural energy balance comparisons in summer for Vancouver, B.C. *Boundary-Layer Meteorology*, **36**(4), 351–369.

Coceal, O. and Belcher, S. E. (2004). A canopy model of mean winds through urban areas. *Quarterly Journal of the Royal Meteorological Society*, In press.

Cotton, W. R. and Pielke, R. A. (1995). *Human Impacts on Weather and Climate*, chapter 5, pages 73–84. Cambridge University Press.

C.R.C. (1993). *Handbook of Chemistry and Physics*. CRC Press Inc., 74th edition edition.

Dabbert, W. F. *et al.* (2000). Forecast issues in the urban zone: Report of the 10th prospectus development team of the U.S. weather research program. *Bulletin of the American Meteorological Society*, **81**(9), 2047–2064.

Deardorff, J. W. (1966). The counter-gradient heat flux in the lower atmosphere and in the laboratory. *Journal of the Atmospheric Sciences*, **23**, 503–506.

Dunlop, C. C. and Clark, P. A. (1997). Forcing the single column UM from the mesoscale model. Forecasting Research Division Technical Report 215, Met Office.

Dyer, A. J. (1967). The turbulent transport of heat and water vapour in an unstable atmosphere. *Quarterly Journal of the Royal Meteorological Society*, **93**, 501–508.

Essery, R., Best, M., and Cox, P. (2001). MOSES 2.2, Hadley Centre Technical Note 30. Technical report, Hadley Centre, Met Office.

Essery, R. L. H., Best, M. J., Betts, R. A., and Cox, P. M. (2003). Explicit representation of subgrid heterogeneity in a GCM land surface scheme. *Journal of Hydrometeorology*, **4**(3), 530–543.

Finnigan, J. (2000). Turbulence in plant canopies. *Annual Review of Fluid Mechanics*, **32**, 519–571.

Garcia-Cueto, R., Jáuregui, E., and Tejeda, A. (2003). Urban / rural energy balacne observations in a desert city in northern Mexico. In *Proceedings of the Fifth International Conference on Urban Climate, Łódź, Poland.*

Garratt, J. R. (1992). *The Atmospheric Boundary Layer*, chapter 8, pages 224–257. Cambridge University Press.

Graves, H., Watkins, R., Westbury, P., and Littlefair, P. (2001). Cooling buildings in London: Overcoming the heat island. Technical report, BRE Centre for Environmental Engineering.

Grimmond, C. S. B. (1992). Suburban energy balance, Vancouver. *International Journal of Climatology*, **12**(5), 481–497.

Grimmond, C. S. B. and Oke, T. R. (1995). Comparison of heat fluxes from summertime observations in the suburbs of four North American cities. *Journal of Applied Meteorology*, **34**, 873–889.

Grimmond, C. S. B. and Oke, T. R. (1999a). Aerodynamic properties of urban areas derived from analysis of surface form. *Journal of Applied Meteorology*, **38**, 1262–1292.

Grimmond, C. S. B. and Oke, T. R. (1999b). Heat storage in urban areas: Local-scale observations and evaluation of a simple model. *Journal of Applied Meteorology*, **38**, 922–940.

Grimmond, C. S. B. and Oke, T. R. (2002). Turbulent heat fluxes in urban areas: Observations and a Local-scale Urban Meteorological Parameterization Scheme (LUMPS). *Journal of Applied Meteorology*, **41**, 792–810.

Grimmond, C. S. B., Cleugh, H. A., and Oke, T. R. (1991). An objective urban heat storage model and its comparison with other schemes. *Atmospheric Environment*, **25B**, 311–326.

Grossman-Clarke, S., Zehnder, J. A., and Stefanov, W. L. (2003). Effects of urban land cover modifications in a mesoscale meteorological on planetary boundary layer characteristics in a semi-arid metropolitan area. In *Proceedings of the Fifth International Conference on Urban Climate, Łódź, Poland.*

Hertel, O. and Berkowicz, R. (1989). Modelling pollution from traffic in a street canyon. Evaluation of data and model development. Technical Report DMU LUFT-A129, National environmetal research institute, Denmark.

Hewer, F. E. and Wood, N. (1998). The effective roughness length for scalar transfer in neutral conditions over hilly terrain. *Quarterly Journal of the Royal Meteorological Society*, **124**, 659–685.

Hogg, A. J., Huppert, H. E., and Dade, W. B. (1997). Erosion by planar turbulent wall jets. *Journal of Fluid Mechanics*, **338**, 317–340.

Hunter, L. J., Johnson, G. T., and Watson, I. D. (1992). An investigation of three-dimensional characteristics of flow regimes within the urban canyon. *Atmospheric Environment*, **26B**(4), 425–432.

Ichinose, T., Shimodozono, K., and Hanaki, K. (1999). Impact of anthropogenic heat on urban climate in Tokyo. *Atmospheric Environment*, **33**(24–25), 3897–3909.

Jackson, P. S. (1981). On the displacement height in the logarithmic velocity profile. *Journal of Fluid Mechanics*, **111**, 15–25.

Johnson, G. T. and Hunter, L. J. (1995). A numerical study of dispersion of passive scalars in city canyons. *Boundary-Layer Meteorology*, **75**, 235–262.

Johnson, G. T. and Watson, I. D. (1984). The determination of view-factors in urban canyons. *Journal of Climate and Applied Meteorology*, **23**, 329–335.

Johnson, G. T., Oke, T. R., Lyons, T. J., Steyn, D. G., Watson, I. D., and Voogt, J. A. (1991). Simulation of surface urban heat islands under 'ideal' conditions at night. Part 1: Theory and tests against field data. *Boundary-Layer Meteorology*, **56**, 275–294.

Kanda, M., Moriwaki, R., Roth, M., and Oke, T. (2002). Area-averaged sensible heat flux and a new method to determine zero-plane displacement length over an urban surface using scintillometry. *Boundary-Layer Meteorology*, **105**, 177–193.

Kannari, A., Mikami, T., and Izumi, T. (2003). Direct effect on temperature rise by anthropogenic heat injection into urban atmosphere. In *Proceedings of the Fifth International Conference on Urban Climate, Łódź, Poland.*

Kawai, T. and Kanda, M. (2003). A simple 3D urban street canyon model for meso scale simulation. In *Proceedings of the Fifth International Conference on Urban Climate, Łódź, Poland.*

Ketzel, M., Berkowicz, R., Müller, W., and Lohmeyer, A. (2002). Dependence of street canyon concentrations on above roof wind speed – implications for numerical modelling. *International Journal of Environment and Pollution*, **17**(4), 356–366.

Kim, J.-J. and Baik, J.-J. (1999). A numerical study of thermal effects on flow and pollutant dispersion in urban canyons. *Journal of Applied Meteorology*, **38**, 1249–1261.

Kobayashi, T. and Takamura, T. (1994). Upward longwave radiation from a non-black urban canopy. *Boundary-Layer Meteorology*, **69**, 201–213.

Kusaka, H., Kondo, H., Kikegawa, Y., and Kimura, F. (2001). A simple single-layer urban canopy model for atmospheric models: Comparision with multi-layer and slab models. *Boundary-Layer Meteorology*, **101**, 329–358.

Landsberg, H. E. (1981). *The urban climate*. International geophysics series. Academic Press.

Lee, H. Y. (1993). An application of NOAA AVHRR thermal data to the study of urban heat islands. *Atmospheric Environment*, **27B**(1), 1–13.

Lemonsu, A. and Masson, V. (2002). Simulation of a summer urban breeze over Paris. *Boundary-Layer Meteorology*, **104**, 463–490.

Liu, C.-H. and Barth, M. C. (2002). Large-eddy simulation of flow and scalar transport in a modeled street canyon. *Journal of Applied Meteorology*, **41**, 660–673.

Loose, T. and Bornstein, R. D. (1977). Observations of mesoscale effects on frontal movement through an urban area. *Monthly Weather Review*, **105**(5), 563–571.

Louka, P. (1998). Measurements of airflow in an urban environment. Ph.D. thesis, Department of Meteorology, University of Reading.

Louka, P., Belcher, S. E., and Harrison, R. G. (1998). Modified street canyon flow. *Journal of Wind Engineering and Industrial Aerodynamics*, **74–76**, 485–493.

Louka, P., Belcher, S. E., and Harrison, R. G. (2000). Coupling between air flow in streets and in the well-developed boundary layer aloft. *Atmospheric Environment*, **34**, 2613–2621.

Lu, J., Pal Arya, S., Snyder, W. H., and Lawson Jr., R. E. (1997a). A laboratory study of the urban heat island in a calm and stably stratified environment. Part I: Temperature field. *Journal of Applied Meteorology*, **36**, 1377–1391.

Lu, J., Pal Arya, S., Snyder, W. H., and Lawson Jr., R. E. (1997b). A laboratory study of the urban heat island in a calm and stably stratified environment. Part II: Velocity field. *Journal of Applied Meteorology*, **36**, 1392–1402.

Macdonald, R. W. (2000). Modelling the mean velocity profile in the urban canopy layer. *Boundary-Layer Meteorology*, **97**, 25–45.

Macdonald, R. W., Griffiths, R. F., and Hall, D. J. (1998). An improved method for the estimation of surface roughness of obstacle arrays. *Atmospheric Environment*, **32**(11), 1857–1864.

Martilli, A. (2002). Numerical study of urban impact on boundary layer structure: Sensitivity to wind speed, urban morphology and rural soil moisture. *Journal of Applied Meteorology*, **41**, 1247–1267.

Martilli, A., Clappier, A., and Rotach, M. W. (2002). An urban surface exchange parameterisation for mesoscale models. *Boundary-Layer Meteorology*, **104**, 261–304.

Masson, V. (2000). A physically-based scheme for the urban energy budget in atmospheric models. *Boundary-Layer Meteorology*, **94**(3), 357–397.

Masson, V., Grimmond, C. S. B., and Oke, T. R. (2002). Evaluation of the town energy balance (TEB) scheme with direct measurements from dry districts in two cities. *Journal of Applied Meteorology*, **41**, 1011–1026.

McNaughton, K. G. and Spriggs, T. W. (1986). A mixed-layer model for regional evaporation. *Boundary-Layer Meteorology*, **34**, 243–262.

Mills, G. M. (1993). Simulation of the energy budget of an urban canyon—I. Model structure and sensitivity test. *Atmospheric Environment*, **27B**(2), 157–170.

Mills, G. M. and Arnfield, A. J. (1993). Simulation of the energy budget of an urban canyon—II. Comparison of the model results with measurements. *Atmospheric Environment*, **27B**(2), 171–181.

Myrup, L. O. (1969). A numerical model of the urban heat island. *Journal of Applied Meteorology*, **8**, 908–918.

Nakamura, Y. and Oke, T. R. (1988). Wind, temperature and stability conditions in an east-west oriented urban canyon. *Atmospheric Environment*, **22**(12), 2691–2700.

Narita, K. (2003). Wind tunnel experiment on convective transfer coefficient in urban street canyon. In *Proceedings of the Fifth International Conference on Urban Climate, Łódź, Poland.*

Noilhan, J. (1981). A model for the net total radiation flux at the surfaces of a building. *Building and the Environment*, **16**(4), 259–266.

Nunez, M. and Oke, T. R. (1977). The energy balance of an urban canyon. *Journal of Applied Meteorology*, **16**, 11–19.

Offerle, B., Jonsson, P., Eliasson, I., and Grimmond, C. S. B. (2003). Preliminary investigation of energy balance fluxes in Ouagadougou, Burkina Faso. In *Proceedings of the Fifth International Conference on Urban Climate, Łódź, Poland.*

Okamoto, S., Nakaso, K., and Kawai, I. (1993). Effect of rows of two-dimensional square ribs of flow property along plane wall. *JSME Interational Journal Series B. - Fluid and Thermal Engineering*, **36**(1), 121–129.

Oke, T. R. (1982). The energetic basis of the urban heat island. *Quarterly Journal of the Royal Meteorological Society*, **108**, 1–24.

Oke, T. R. (1987). *Boundary Layer Climates*, chapter 8, pages 262–303. Routledge, 2nd edition.

Oke, T. R. (1988). Street design and urban canopy layer climate. *Energy and Buildings*, **11**, 103–113.

Oke, T. R. and East, C. (1971). The urban boundary layer in Montreal. *Boundary-Layer Meteorology*, **1**, 411–437.

Oke, T. R., Johnson, G. T., Steyn, D. G., and Watson, I. D. (1991). Simulation of surface urban heat islands under 'ideal' conditions at night. Part 2: Diagnosis of causation. *Boundary-Layer Meteorology*, **56**, 339–358.

Oke, T. R., Sproken-Smith, R. A., Jáuregui, E., and Grimmond, C. S. B. (1999). The energy balance of central Mexico City during the dry season. *Atmospheric Environment*, **33**, 3919–3930.

O'Rourke, P. A. and Terjung, W. H. (1981). Urban parks, energy budgets, and surface temperatures. *Archives for Meteorology, Geophysics and Bioclimatology – Series B*, **29**, 327–344.

Owczarek, S. (1997). Vector model for calculation of solar radiation intensity and sums incident on tilted surfaces. Identification for the three sky condition in Warsaw. *Renewable Energy*, **11**(1), 77–96.

Pawlak, W. and Fortuniak, K. (2002). Estimation of the effective albedo of the urban canyon - comparison of two different algorithms. In *Proceedings of the International Conference "Man and Climate in the 20th Century", Wrocław, Poland.*

Pawlak, W. and Fortuniak, K. (2003). Application of physical model to study effective albedo of the urban canyon. In *Proceedings of the Fifth International Conference on Urban Climate, Łódź, Poland.*

Rafailidis, S. (1997). Influence of building areal density and roof shape on the wind characteristics above a town. *Boundary-Layer Meteorology*, **85**, 255–271.

Rao, K., Gunter, R. L., White, J. R., and Hosker, R. P. (2002). Turbulence and dispersion modeling near highways. *Atmospheric Environment*, **36**(27), 4337–4346.

Raupach, M. R. (1994). Simplified exressions for vegetation roughness length and zero-plane displacement as functions of canopy height and area index. *Boundary-Layer Meteorology*, **71**, 211–216.

Raupach, M. R. (2001). Combination thoery and equilibrium evaporation. *Quarterly Journal of the Royal Meteorological Society*, **127**, 1149–1181.

Raupach, M. R., Thom, A. S., and Edwards, I. (1980). A wind-tunnel study of turbulent flow close to regularly arrayed rough surfaces. *Boundary-Layer Meteorology*, **18**, 373–397.

Richards, K. and Oke, T. R. (2002). Validation and results of a scale model of dew deposition in urban environments. *International Journal of Climatology*, **22**, 1915–1933.

Rotach, M. W. (1993a). Turbulence close to a rough urban surface. Part I: Reynolds stresses. *Boundary-Layer Meteorology*, **65**, 1–28.

Rotach, M. W. (1993b). Turbulence close to a rough urban surface. Part II: Variances and gradients. *Boundary-Layer Meteorology*, **66**, 75–92.

Roth, M. (2000). Review of atmospheric turbulence over cities. *Quarterly Journal of the Royal Meteorological Society*, **126**, 941–990.

Rozoff, C. M. amd Cotton, W. R. and Adegoke, J. O. (2003). Simulation of St. Louis, Missouri, land use impacts on thunderstorms. *Journal of Applied Meteorology*, **42**, 716–738.

Sailor, D. J., Lu, L., and Fan, H. (2003). Estimating urban anthropogenic heating profiles and their implications for heat island development. In *Proceedings of the Fifth International Conference on Urban Climate, Łódź, Poland.*

Sakakibara, Y. (1996). A numerical study of the effect of urban geometry upon the surface energy budget. *Atmospheric Environment*, **30**, 487–496.

Salmond, J. A., Roth, M., Oke, T. R., Satyanarayana, A. N. V., Vogt, R., and Christen, A. (2003). Comparison of turbulent fluxes from roof top versus street canyon locations using scintillometers and eddy covariance techniques. In *Proceedings of the Fifth International Conference on Urban Climate, Łódź, Poland.*

Schmid, H. P. (1994). Source areas for scalars and scalar fluxes. *Boundary-Layer Meteorology*, **67**, 293–318.

Schmid, H. P., Cleugh, H. A., Grimmond, C. S. B., and Oke, T. R. (1991). Spatial variability of energy fluxes in suburban terrain. *Boundary-Layer Meteorology*, **54**, 249–276.

Shankar, P. N. and Deshpande, M. D. (2000). Fluid mechanics in the driven cavity. *Annual Review of Fluid Mechanics*, **32**, 93–136.

Sini, J.-F., Anquetin, S., and Mestayer, P. G. (1996). Pollutant dispersion and thermal effects in urban street canyons. *Atmospheric Environment*, **30**(15), 2659–2677.

Smirnova, T. G., Brown, J. M., and Benjamin, S. G. (1997). Performance of different soil model configurations in simulating ground surface temperature and surface fluxes. *Monthly Weather Review*, **125**, 1870–1884.

Sparrow, E. M. and Cess, R. D. (1970). *Radiation Heat Transfer*, chapter 3–4, appendices A & B, pages 75–136, 300–313. Thermal Science Series. Brooks/Cole.

Spronken-Smith, R. A., Kossmann, M., and Zawar-Reza, P. (2003). Where does all the energy go? Energy partitioning in suburban Christchurch under stable wintertime conditions. In *Proceedings of the Fifth International Conference on Urban Climate, Łódź, Poland.*

Steyn, D. G. and Lyons, T. J. (1985). Comment on "The determination of view-factors in urban canyons". *Journal of Climate and Applied Meteorology*, **24**, 383–385.

Stull, R. B. (1988). *An Introduction to Boundary Layer Meteorology*. Kluwer Publishers.

Sugawara, H., Yasuda, N., and Naito, G. (2003). Urban heat budget and geometrical structure of building canopy. In *Proceedings of the Fifth International Conference on Urban Climate, Łódź, Poland.*

Swaid, H. (1993). Urban climate effects of artificial heat sources and ground shadowing by buildings. *International Journal of Climatology*, **13**, 797–812.

Taha, T. (1999). Modifying a mesoscale meterological model to better incorporate urban heat storage: A bulk-parameterization approach. *Journal of Applied Meteorology*, **38**, 466–473.

Tennekes, H. and Lumley, J. L. (1997). *A first course in turbulence*, chapter 2, pages 27–58. The MIT press, 16th edition.

Townsend, A. A. (1976). *The structure of turbulent shear flow*, chapter 7: Boundary layers and wall jets, pages 259–333. Cambridge University Press, 2nd edition.

Uehara, K., Wakamatsu, S., and Ooka, R. (2003). Studies on critical Reynolds number indices for wind-tunnel experiments on flow within urban areas. *Boundary-Layer Meteorology*, **107**, 353–370.

Verhoef, A., de Bruin, H. A. R., and van den Hurk, B. J. J. M. (1997). Some practical notes on the parameter kB^{-1} for sparse vegetation. *Journal of Applied Meteorology*, **36**, 560–572.

Verseghy, D. L. and Munro, D. S. (1989a). Sensitivity studies on the calculation of the radiation balance of urban surfaces: I. Shortwave radiation. *Boundary-Layer Meteorology*, **46**, 309–331.

Verseghy, D. L. and Munro, D. S. (1989b). Sensitivity studies on the calculation of the radiation balance of urban surfaces: II. Longwave radiation. *Boundary-Layer Meteorology*, **48**, 1–18.

Voogt, J. and Grimmond, C. S. B. (2000). Modeling surface sensible heat flux using surface radiative temperatures in a simple urban area. *Journal of Applied Meteorology*, **39**(10), 1679–1699.

Voogt, J. A. and Oke, T. R. (1998). Radiometric temperatures of urban canyon walls obtained from vehicle traverses. *Theoretical and Applied Climatology*, **60**(1–4), 199–217.

Vu, T. C., Ashie, Y., and Asaeda, T. (2002). A $k - \varepsilon$ turbulence closure model for the atmospheric boundary layer including urban canopy. *Boundary-Layer Meteorology*, **102**, 459–490.

Wallace, J. S. and Verhoef, A. (1996). *Leaf Development and Canopy Growth*. Sheffield Academic Press. Chapter 8. Modelling interactions in mixed-plant communities: light, water and carbon dioxide.

Wood, N. and Mason, P. (1991). The influence of static stability on the effective roughness lengths for momentum and heat transfer. *Quarterly Journal of the Royal Meteorological Society*, **117**, 1025–1056.

Xu, Y., Zhou, C., Li, Z., and Zhang, W. (1997). Turbulent structure and local similarity in the tower layer over the Nanjing area. *Boundary-Layer Meteorology*, **82**, 1–21.

Yamartino, R. J. and Wiegand, G. (1986). Development and evaluation of simple models for the flow, turbulence and pollutant concentration fields wihtin an urban street canyon. *Atmospheric Environment*, **20**(11), 2137–2156.

Yoshida, A., Tominaga, K., and Watatani, S. (1991). Field measurements on energy balance of an urban canyon in the summer season. *Energy and Buildings*, **15**, 417–423.